THERMAL CONDUCTION AND HEAT GENERATION PHENOMENA IN LI-ION CELLS

by

STEPHEN JAMES DRAKE

Presented to the Faculty of the Graduate School of

The University of Texas at Arlington in Partial Fulfillment

of the Requirements

for the Degree of

DOCTOR OF PHILOSOPHY

THE UNIVERSITY OF TEXAS AT ARLINGTON

December 2014

Acknowledgements

Firstly, I would like to thank my research and academic advisor, Dr. Ankur Jain. Your thoughtful advice was invaluable over the course of my research. Your guidance and insight provided an immense impact on my learning. Additionally, you provided an amazing atmosphere to work and collaborate. From weekly group meetings to semiannual research group BBQs. You opened up your home and your family to everyone in the group. You took you role as a mentor outside the official walls of what you were required to do and I believe its impact is immeasurable.

Additionally, I wish to thank my committee members: Dr. Miguel Amaya, Dr. Cheng Luo, Dr. Hyejin Moon, and Dr. David Wetz, for their support. Their willingness and shared interest in my research was a great honour by agreeing to take the time and serve on my defense committee. Specifically Dr. Wetz for supporting cross-disciplinary collaboration. These efforts greatly expanded my appreciation for the research and allowed me to see its impact beyond my scope of my work.

I am grateful for all my teachers throughout the years who taught me and made this journey possible. I must thank the entire staff in the engineering department with their help during this process. Their assistance in deadlines, form submissions, scheduling meeting, and in general pointing me in the right direction over the past few years with a smile was very much appreciated.

I would also like to thank my colleagues and lab-mate: Leila, Vivek, Daipayan, and Krishna. We've accomplished some great things. Thank you all for your help from article collaborations, to sitting through group meetings and repetitive presentation practices. Also thanks to Matt for doing all the electrical cycling dirty work needed for my data analysis.

Finally I must thank my family and friends for their love, encouragement, and support throughout my academic pursuits. To Sarah, for supporting me through this endeavor. You have been my sounding board, my welcome distraction, and audience for my thoughts and emotions. You've truly shown me how happy I can be and I look forward to much more. To Kyle, thank you for being my lifelong friend. You've been my source for spontaneous activities, along with memorable camping and road trips. To my sister, Heather. Thank you for being an exceptional role model for me as I was growing up.

Most of all to my father and mother, Steve and Karen Drake, along with my grandparents, Herb and Jean Stange. I would like to express my deepest gratitude for their encouragement and patience. I am extremely fortunate to be so blessed; they supported me in ways unimaginable by many. Thank you for teaching me to be the man I am today, and to strive to become better with each passing day. You guided me by example. Your sacrifice and humility under adversity and good fortunes inspires me. Without your help this would not have been possible. I love you.

November 11, 2014

Abstract

THERMAL CONDUCTION AND HEAT GENERATION PHENOMENA IN LI-ION CELLS

Stephen James Drake, PhD

The University of Texas at Arlington, 2014

Supervising Professor: Ankur Jain

Cylindrical lithium ion (Li-ion) cells have demonstrated high power density and energy capacity among other energy storage devices. Despite their already widespread use, the thermal transport properties of cylindrical Li-ion batteries are not well documented and understood, while a sizable amount of work has been carried out for electrical, electrochemical, and materials optimization of Li-ion cells. These thermal phenomena are particularly important for high discharge rate batteries. With this uncertainty, if thermophysical properties are not accounted for in thermal models, the result may be a significant under-prediction or over-prediction of the temperature field in a Li-ion cell.

Experimental techniques are described that measure the thermal transport properties and heat generation rate in Li-ion cells. The anisotropic thermal conductivity and heat capacity of a Li-ion cell is measured using an adiabatic unsteady heating method. A cylindrical Li-ion cell is subjected to radial or axial heating on one of its outer surfaces, while all other surfaces are kept adiabatic. Experimental measurements indicate that radial thermal conductivity is around two orders of magnitude lower than axial thermal conductivity. Further, a variety of cells of varying shapes and sizes are characterized, including prismatic and pouch form-factor cells. The effect of the cell's

state of charge (SOC) and temperature induced accelerated aging on its thermophysical properties is also investigated.

An experimental technique is also developed for measuring the steady-state heat generation in a thermal test cell similar to a Li-ion cell. A heat flux sensor is applied to the curved surface of the test cell. Verified with an analytical model, this method predicts the value of the heat generation rate with an error of less than 10%. This model is constrained to a truncated experimental data set when data for only a short time may be available. The accuracy improves as the amount of available data increases. In this approach, it is not important to know material property values, which further adds to the simplicity and ease of the measurement.

Heat generation measurement on an actual Li-ion cell undergoing high rate discharge presents additional challenges. Towards this, the method described has been extended. Testing was first performed using the thermal test cell for real-time heat generation capture followed by 26650 cells at discharge rate of up to 9.6C. Measuring cell temperature and surface heat flux enables in situ heat generation rate as a function of time. Thermal measurements are within around 10% of well-known theoretical models based on electrical parameters at higher rates at which the cell can discharge – often referred to as its C-rate.

This work addresses multiple important voids in thermal understanding of Li-ion cells by describing relatively simple methods for thermal characterization. It is expected that this experimental work will result in a complete and robust method for thermophysical property determination and real-time heat generation measurement in Li-ion cells. These results will improve the understanding of thermal characteristics in cells and provide better cell performance by increasing safety and extend operational life.

Table of Contents

List of Illustrations

List of Tables

Chapter 1

Introduction

Li-ion Cell Technology

Lithium-ion cells [Goodenough *et al.*, 2013; Scrosati *et al.*, 2010] offer excellent energy storage and discharge capability [Armand *et al.*, 2008; Scrosati *et al.*, 2010]. As a result, Li-ion cells have been investigated for energy storage and conversion in consumer electronics and electric/hybrid vehicles along with military applications [Khaligh et al., 2010; Marsh et al., 2001; Linden et al., 2002]. Lithium-ion batteries are an ideal energy storage candidate due to their combination of high energy density as well as high power density Figure 1-1.

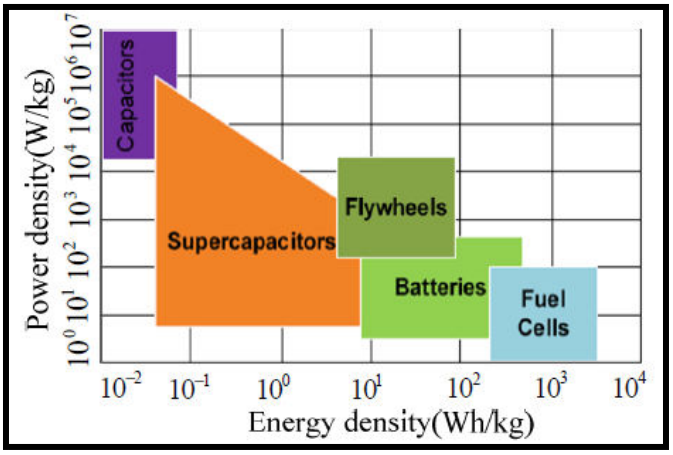

Figure 1-1 Ragone plot showing the power and energy density of various conventional off-the-shelf electrochemical energy storage technologies [Baoquan et al., 2012]

Li-ion batteries are an attractive choice for use in current and future high power energy applications such as primary generation sources, backup energy storage systems, and pulsed sourcing systems. Among those of interest are uses in military applications, more specifically in the Navy. Navy ships are expected to continue becoming more and more electrically driven [Thonham et al., 2013; Katzman, 2012; Lundquist, 2012]. Between the conventional electrical loads, new propulsion systems, and advanced high power directed energy weapons, the number

of electrical loads that must be reliably sourced will continue to increase. Traditional means of electrical generation, such as diesel powered turbines, are capable of powering these ships under standard operating conditions, but would need to be vastly oversized to simultaneously propel the ship and drive the various high power pulsed loads a future ship will have on board. In order to maintain its sourcing operation, high magnetic fields must be generated and sustained within a generator at all times, even during pulsed loads. When generators are used to source high power pulsed loads, it is difficult to maintain the rotational speed of a larger rotor, requiring more fossil fuel usage in order to ensure the generator is always ready to supply the high power that may be demanded of it. This is inefficient and far from optimal as the Navy works to reduce its dependence on fossil fuels. Even if a smaller dedicated turbine generator is allocated for the pulsed loads, the transient nature of these loads along with their intermittent use prevents a dedicated generator from being continuously base loaded, further reducing its efficiency and power quality.

Electrochemical energy storage devices such as lithium-ion batteries are being considered for use as a dedicated source capable of driving intermittent high power pulsed loads. This approach may dramatically reduce the oversizing of mechanical generators in order to be able to handle the recharge of the energy storage devices during off-peak operation. This reduces fossil fuel consumption and increases the overall system efficiency.

In directed energy applications, energy storage devices possessing high energy density are needed in order to maximize the number of pulsed discharges available per battery cycle, while high power density is required so that the energy storage is able to source the ever increasing high currents demanded by the pulsed load during operation. In general, a device having a higher energy density has a lower power density, so interest is placed in properly specifying power density requirements in order to maximize energy density. Such applications

might require electrically straining cells beyond their intended operating conditions and discharge rates, further complicating safety mitigation and environmental concerns.

More so, several recent incidents, including fire in a Li-ion battery pack aboard an aircraft and submarines [Wang *et al.*, 2012; Cavas, 2008] have occurred within normal manufactures recommended operational ranges. These highlight the importance of thermal understanding and design of Li-ion batteries. Fundamental studies of thermal phenomena occurring within Li-ion batteries are essential for developing a basic understanding of these technological challenges, and to design cooling systems prevent thermal runaway during high power operation. It is also critical to measure and understand the fundamental thermal transport properties of a Li-ion cell for accurate system-level modeling and design.

Unfortunately, fundamental construction of Li-ion cells provides barriers for simple analysis. Cells are constructed by using a combination of four main materials: the cathode, anode, separator, and electrolyte. The cathode retains the lithium-metal oxide materials, the anode typically containing graphite, the separator that electrically isolates the anode and cathode, while the electrolyte provides the medium through which the ion transfer occurs. Figure 1-2 shows an internal diagram of a typical cylindrical cell.

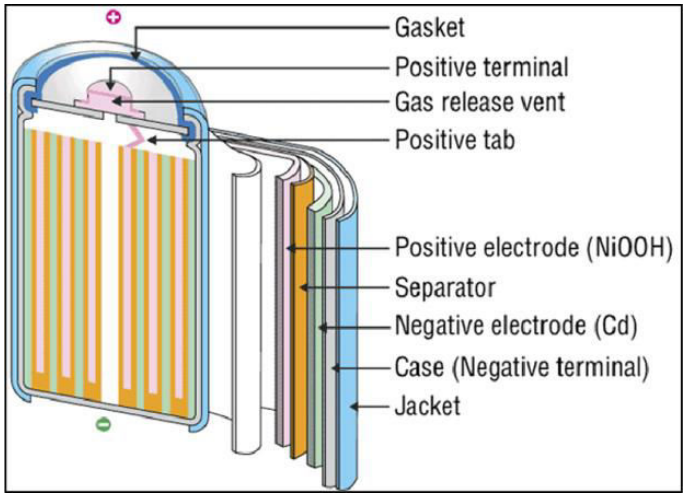

Figure 1-2 Detailed view of the spiral jelly roll construction inside a test cell [Winter *et al.*, 2004]

The cathode, anode, and separator are wound together on a spindle and placed inside the battery casing with the electrolyte added later. This “Swiss-roll” or “jelly-roll” formation creates a severe directionally dependent path for heat flow between the radial and axial direction. This is a major disadvantage for thermal management.

Figure 1-3 shows a 26650 cell disassembled without the casing and the multiple layers of cathode, anode, and separator materials winding around the core.

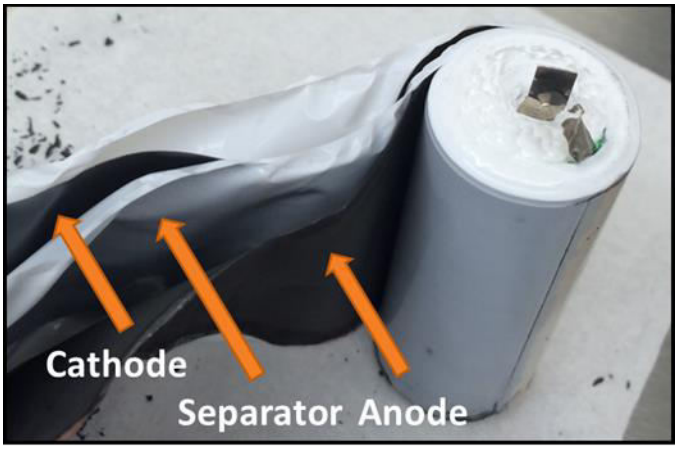

Figure 1-3 Disassembled 26650 to visualize internal material layers

Axially heat is expected to flow between each material encountering minimal material thermal interfaces, while radially, heat flow is impeded by multiple layers of component materials and the thermal contact resistances at such material interfaces.

This complication is exacerbated with future requirements of energy storage devices to be charged and discharged at high current rates that results in temperature rise and heat generation due, mainly to Joule heating. Joule heating is proportional to the square of the current flowing through the cell. The resulting temperature rise of the cell, if not properly predicted and managed can both degrade cell life as well as lead to disastrous safety issues. Despite their already widespread use, the thermal transport properties of cylindrical lithium-ion batteries are not well documented and understood.

Thermal Challenges in Li-ion Cells

During operation, batteries are subjected to cyclical charging and discharging, where a byproduct is temperature rise. Operating at elevated temperatures has been known to degrade the electrolyte composition, thereby negatively affecting cell life and performance [Rao *et a*l., 2011; Pesaran, 2002; Kahn et al., 2011; Smith et al., 2010]. Should this excess heat surpass a critical threshold, which varies dependent on exact battery chemistry, a cathode thermal runaway situation may arise, leading to electrolyte release, and potentially fire [Kim et al., 2007; Lisbona et al., 2011]. Capacity and power reduction has also been found to occur at high operating temperature [Liaw *et al*., 2003].

The process of conversion of electrical energy to chemical energy and vice versa inherently produces heat [Thomas *et al*., 2003; Bernardi *et al*., 1985; Yi *et al*., 2012; *Srinivasan et al*., 2003], which results in increased cell temperature [Shah *et al*., 2014; Shah2 *et al*., 2014;Taheri *et al*., 2013]. The operation of a Lithium-ion cell is based on several highly coupled phenomena involving multiple physical processes. For example, exothermic electrochemical reactions produce heat [Thomas *e*t al., 2003; Srinivasan et al., 2003; Chen et al., 1996], which causes temperature rise. Since temperature directly affects the rates of electrochemical reactions and electrical impedances [Thomas *et al*.,2003], therefore, the thermal performance of the cell in turn affects electrochemical and electrical performance. High energy content in Li-ion batteries plays a large role in thermal phenomena that affect performance as well as safe battery operation, and in most cases, contribute to operating limits [Rao et al., 2011; Pesaran, 2002; Kahn et al., 2011; Smith et al., 2010].

Uncontrolled temperature rise in a Li-ion cell is known to adversely affect performance as well as safety [Bandhauer et al., 2011; Broussely et al., 2002]. Power fade, capacity fade and self-discharge are well known performance-related problems at high temperature [Linden et al., 2002; Broussely et al., 2002; Aurbach et al., 2007; Johnson et al., 1998]. In addition, safety at

high temperature is a major concern [Spotnitz et al., 2003; Abraham et al., 2006]. Chemical reactions feeding into each other are known to occur if the cell temperature exceeds a certain threshold [Wang *et al*., 2012]. Thermal runaway is a serious concern that may lead to catastrophic failure.

Temperature measurement has been mostly limited to measuring the outside surface temperature, although some indirect measurements of the core temperature have also been reported [Srinivasan et al., 2011]. Significant temperature gradient exists within the cell, particularly at high currents, due to the low radial thermal conductivity of the cell [Shah et al.,2014; Srinivasan et al., 2011]. Accurate thermal properties are critical for the precision of analytical models.

While thermophysical properties of Li-ion cells are currently being investigated, not much literature exists on the measurement of heat generation rate in Li-ion cells. Similar to any other energy storage device, charging or discharging a Li-ion cell results in heat generation and thus increase in temperature due to electrochemical reactions and Joule heating. A number of theoretical models have been proposed to predict heat generation rate as a function of electrochemical parameters [Bernardi *et* al., 1985; Thomas et al., 2003; Pals et al., 1995; Srinivasan et al., 2003; Chen et al., 1993]. In particular, these models predict the rate at which the cell can discharge, C-rate, to strongly influence the heat generation rate. However, the lack of experimental data severely limits the effectiveness of models, and the possibility of electrochemical-thermal co-optimization based on these models. Only a limited number of papers report measurements of heat generation in Li-ion cells, most of which address only very low C-rates, typically C/1 or lower [Bandhauer *et al*., 2011]. In these experiments, a calorimetry technique such as Accelerated Rate Calorimetry, Isothermal Calorimetry, or Radiative Calorimetry is used to measure heat rejected from a cell to a thermal sink, and thus determine heat generation in the cell. Such methods do not adapt well to high-rate processes due to the

transient nature of heat generation, which may explains the lack of measurements reported at higher C-rates. Moreover, these methods provide time-averaged values of heat generation rate. While characterizing the charge/discharge process with a single overall heat generation rate may be sufficient for some applications, variation of heat generation with time may need to be accounted for in others. These calorimetry-based experiments typically use expensive equipment and might not be readily available.

Summary of Current Work

The two thermal transport properties that primarily govern temperature rise and thermal runaway in lithium-ion batteries are thermal conductivity and heat capacity. A robust experimental technique for measurement of these properties is of primary importance for safe thermal design of lithium-ion cells and energy storage systems based on such devices.

Several papers have reported computational and experimental investigation of temperature distribution at the cell-level and at the pack-level [Rao *et al*., 2011, Pesaran, 2002, Smith *et al*., 2010; Forgez *et al*., 2010; Chen *et al*., 1993; Mayyas *et al*., 2011; Chen *et al*., 2005]. A wide range of electrochemical and electrical studies have been performed on lithium-ion cells in the past [Pesaran, 2002; Khateeb *et al*., 2004; Fang *et al*., 2010; *Belt et al*., 2005; Ogumi *et al*., 2004; Zhang *et al*., 2008]. Accurate information about underlying thermal properties such as thermal conductivity and heat capacity is critical for the accuracy of such models.

Heat capacity of batteries has been measured [Pesaran *et al*., 2001]. However, this method does not provide thermal conductivity measurements. Core-to-outside lumped thermal resistance of a cell has been measured [Forgez et al., 2010; Lin et al., 2013]. Measurement of thermal conductivity and heat capacity of Li-ion cells using xenon flash technology and steady-state measurements has been reported thermal conductivity and specific heat [Maleki *et al*., 1999]. Recent measurements of heat capacity and thermal conductivity of a Li-ion cell using an adiabatic heating method indicate strong anisotropy in thermal conduction between radial and

axial directions [Drake *et al*., 2013; Zhang *et al*., 2014]. These papers compare experimental data with analytical [Drake et al., 2013] and numerical simulations [Zhang et al., 2014] and find that the radial thermal conductivity is around 150-200 times lower than the axial value. Bandhauer, *et al.* provide a review of thermal phenomena associated with Li-ion cells and also note the lack of thermal property measurement data [Bandhauer *et al*., 2011].

The xenon flash technology method is also cumbersome and expensive. Most of the previous work neglects the anisotropy of thermal conduction within a Li-ion cell. It is desirable to experimentally measure anisotropic components of thermal transport properties in a Li-ion cell.

In addition to thermophysical properties providing operating temperature, Li-ion cell behavior also depends on heat generation rate. A combination of heat conduction along with knowledge of internal heat generation is critical for accurate thermal characterization. Li-ion cells are remarkably sensitive to temperature rise due to heat generation. A number of papers have presented theoretical analysis of heat generation rate as a function of electrochemical parameters such as C-rate [Thomas et al., 2003; Bernardi et al.; 1985; Srinivasan et al., 2003]. Heat generation is caused by several different mechanisms, including exothermic heats of reaction, Ohmic losses, among others. A widely used theoretical model predicts the heat generation rate has been established [Thomas *et al*., 2003].

Temperature excursion beyond a certain limit results in a thermal runaway situation, usually accepted at temperatures above 130–150 °C [Spotnitz et al., 2003; Kim et al., 2007; Balakrishnan et al., 2006]. However is has been proposed that runaway can happen at conditions as low as 80 °C [Hammami *et al*., 2003]. This illustrates the critical need to thoroughly understand the thermal characteristics of Li-ion cells, and to develop effective means to dissipate heat during operation by means of effective cooling. In addition to such safety concerns, effective cooling also

directly influences performance. The C-rate may be limited by thermal concerns if the excess heat generated during discharge is not being properly dissipated.

An improved understanding of factors affecting temperature distribution and heat generation in Li-ion cells may facilitate high C-rate operational life, performance, and safety. Such work will enhance the accuracy of thermal computation for system-level thermal design, and will also help in developing a comprehensive understanding of heat flow within a Li-ion cell.

Chapter 2

Thermal Property Measurements

Introduction

Figure 2-1 shows a top view cutout of a typical Li-ion cylindrical cell. A composite layered material made up of an anode, cathode, separator and current collectors is soaked in electrolyte and rolled in a Swiss roll fashion. Electrode tabs are present at the ends of the cell to collect and conduct electric current to the external cell terminals.

Figure 2-1 Top view cutout of a typical Li-ion cylindrical cell

Due to this construction, the nature of radial thermal transport is expected to be significantly different from axial thermal transport. While in the radial direction, heat flow is expected to be impeded by several thermal contact resistances between the thin layers of several materials, such as electrodes, electrolyte, separator and collector, in the axial direction, thermal conduction is expected to occur primarily along the current collector materials, which often run

continuously in the axial direction. Thermal contacts between materials in microsystems often present significant thermal resistance, sometimes even greater than the material thermal resistance itself [Cahill *et al*., 2002]. Due to this expected anisotropy of thermal transport, it is important to experimentally measure the radial and axial thermal conductivities of a cylindrical Li-ion cell, since the assumption of isotropic thermal transport properties in Li-ion cells design will either underpredict or overpredict the temperature field, both of which are undesirable.

This section describes a new method for measurement of effective heat capacity and anisotropic thermal conductivity of cylindrical Li-ion cells. The method described here is relatively simple, and provides rapid measurement of axial and radial thermal conductivity in addition to heat capacity. The method utilizes the thermal response of the cell to axial or radial heating in an adiabatic configuration. An analytical heat transfer model is developed for modeling temperature distribution during such adiabatic heating. It is shown that simultaneous measurement of thermal conductivity and heat capacity can be obtained in a single experiment. Experimental data are in excellent agreement with the analytical model and indicate strong anisotropy in thermal conduction in 26650 and 18650 cells as expected. Results indicate a significant under-prediction of peak temperature by using only the axial thermal conductivity compared to a case where the anisotropy is accounted for. Results presented in this manuscript will enable more accurate performance models of Li-ion batteries and enable better designs for battery cooling systems.

Cylindrical Cell

Analytical Model

This section derives an analytical model for the expected temperature curve as a function of time when a cylindrical Li-ion cell is subjected to radial or axial heating on one of its outer surfaces, while all other surfaces are kept adiabatic. Figure 2-2 (a) and (b) show a schematic of the geometry for a cylindrical Li-ion cell of radius R and height H being subjected to uniform and

steady heat flux Q'' starting at t = 0 either in the radial direction at r = R, or in the axial direction at z = H.

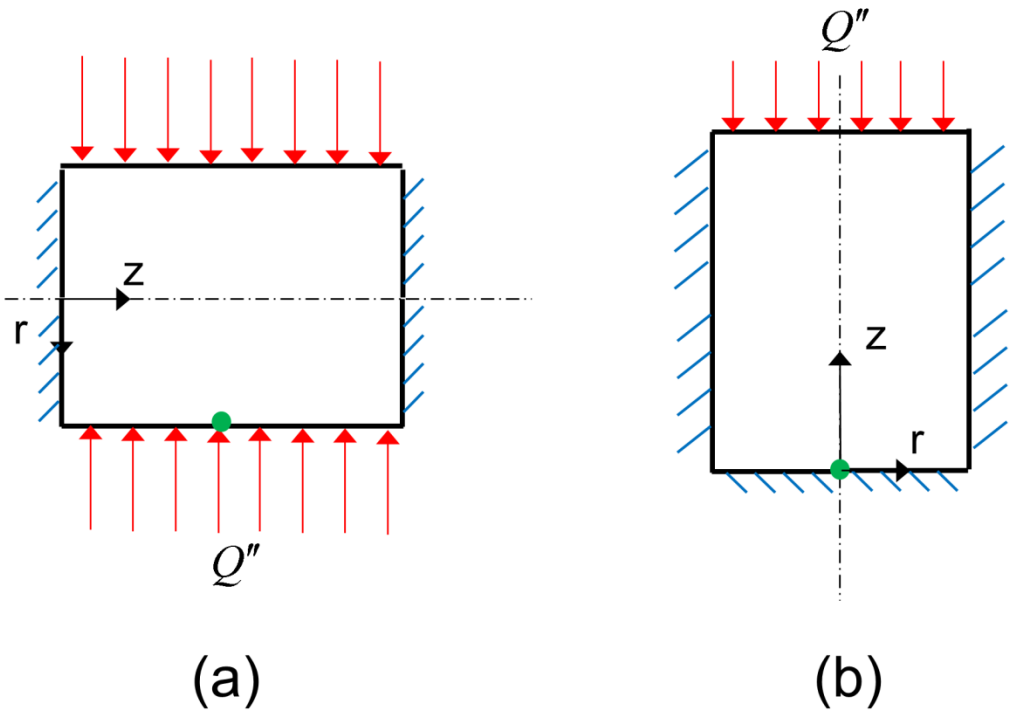

Figure 2-2 Schematic of the geometry for the (a) radial heating, and (b) axial heating cases

In each case, all other boundaries are adiabatic. In order to derive an expression for the temperature of the cell as a function of space and time, governing energy conservation equations along with boundary and initial conditions are written and solved. For the radial heating case shown in Figure 2-2 (a), heat flows only in the radial direction. As a result, the temperature distribution is one-dimensional in space. Assuming that the radial thermal conductivity is uniform and independent of temperature, the governing energy equation is

$$\frac{1}{r}\frac{\partial}{\partial r}\left(r\frac{\partial \theta}{\partial r}\right)=\frac{\rho C_p}{k_r}\frac{\partial \theta}{\partial t} \qquad (1)$$

where $\theta(r,t)$ is the temperature rise above ambient, and ρ, k_r and C_p are the mass density, radial thermal conductivity, and heat capacity of the cell respectively. Equation (1) is subject to the boundary conditions

$$\frac{\partial \theta}{\partial r} = \frac{1}{k_r} Q'' \text{ at } r=R \qquad (2) \qquad \frac{\partial \theta}{\partial r} = 0 \text{ at } r=0 \qquad (3)$$

It is assumed that at the cell is initially at ambient temperature, i.e. $\theta(r,0)= 0$.

Since there is only heat flux into the system, without any mechanism for heat loss, this problem does not have a steady-state solution and theoretically speaking the temperature of the battery keeps rising as a function of time. In reality, second-order effects such as radiation will limit the temperature rise at very high temperatures. Within the relatively low temperature range in this work, radiation has been shown to be negligible [Jain *et al.*, 2008]. An expression for $\theta(r,t)$ can be derived by recognizing that the average temperature of the battery, denoted by $\theta_m(t)$ must rise linearly with time. It can be shown that for such problems without a steady-state, the sub-problem resulting from the subtraction of $\theta_m(t)$ from $\theta(r,t)$ has a solution comprising $s(r)$, a steady-state component, and $w(r,t)$, an exponentially decaying transient part.

The average temperature rise $\theta_m(t)$ can be determined by considering the total heat capacity of the cell mass. By solving the remaining sub-problem using linear superposition and Eigen-functions expansion, the final solution is derived to be

$$\theta(r,t) = \theta_m(t) + s(r) + w(r,t) = \frac{2Q''}{\rho C_p R} t + \frac{Q''}{k_r R}\left(\frac{r^2}{2} - \frac{R^2}{4}\right) - \frac{2Q''R}{k_r} \sum_{n=1}^{\infty} \frac{J_0(\lambda_n r)}{(\lambda_n R)^2 J_0(\lambda_n R)} \exp\left(-\frac{k_r \lambda_n^{\,2}}{\rho C_p} t\right) \quad (4)$$

The eigenvalues λ_n are obtained from roots of the equation $J'_0(\lambda_n R) = 0$. J_0 denotes Bessel function of the first kind of order 0.

Equation (4) shows that the temperature measured at each location has three components – a component that linearly increases with time, for which the slope is inversely proportional to the product ρC_p, a time-invariant, spatially varying term which is inversely

proportional to the radial thermal conductivity, and an exponentially decaying term for which the time constant is inversely proportional to the radial thermal diffusivity. Provided the density can be measured separately, this shows that the measurement of the slope and intercept of the temperature curve after transients have died out can be used to simultaneously determine the heat capacity and radial thermal conductivity of the cell under test.

For the axial heating case, temperature profile is expected to be one-dimensional in space due to radial symmetry. Assuming that the axial thermal conductivity is uniform and independent of temperature, the governing energy equation is given by

$$\frac{\partial^2 \theta}{\partial z^2} = \frac{\rho C_p}{k_z} \frac{\partial \theta}{\partial t} \qquad (5)$$

where $\theta(z,t)$ is the temperature rise, and k_z is the axial thermal conductivity. Equation (5) is subject to the boundary conditions

$$\frac{\partial \theta}{\partial z} = \frac{1}{k_z} Q'' \text{ at } z=H \qquad (6) \qquad \frac{\partial \theta}{\partial z} = 0 \text{ at } z=0 \ (7)$$

It is assumed that at the cell is initially at ambient temperature, i.e. $\theta(r,0)= 0$.

This problem is solved in a similar manner as the radial problem. In this case, the solution is found to comprise three components given by

$$\theta(z,t) = \theta_m(t) + s(z) + w(z,t) = \frac{Q''}{\rho C_p H} t + \frac{Q''}{2k_z H}\left(z^2 - \frac{H^2}{3}\right) + \sum_{n=1}^{\infty} \frac{(-1)^{n+1} 2Q''H}{k_z (n\pi)^2} Cos\left(\frac{n\pi z}{H}\right) \exp\left(-\frac{k_z (n\pi)^2}{\rho C_p H^2} t\right) \qquad (8)$$

Measurement of the slope and intercept of the temperature curve at large time results in determination of the heat capacity and axial thermal conductivity respectively.

When designing an experimental setup such as this, it is important to select the sample height, H such that it provides measurable values of the slope and intercept. If H is too small, the slope is too large, and the temperature rises very rapidly, leading to large experimental uncertainty. This also results in approaching the maximum temperature limit of the cell too soon.

On the other hand, if H is too large, both the slope and intercept are small and the time constant of the transient decay is too large, resulting in very sluggish temperature rise as a function of time. If the sample size is fixed, as is the case for a standard Li-ion cell, the heat flux Q'' may be adjusted to result in increased sensitivity of experimental data.

Experiments

26650 and 18650 Cells

An experimental technique for determining the heat capacity and anisotropic thermal conductivity of a cell is developed in this section. The technique yields thermal conductivity and heat capacity in a single experiment. In order to do so, the cell is subjected to adiabatic heating in the radial or axial direction, and its temperature rise is measured as a function of time. Every cell under test is prepared using the same method.

The cells are electrically characterized by performing electrochemical impedance spectroscopy (EIS) using a potentiostat. The potentiostat is capable of providing the AC and DC resistance of the battery. The DC resistance is the standard measurement of the relative amplitudes of voltage and current. Unlike the DC resistance, the AC resistance is calculated by applying a small AC ripple and the recording the corresponding AC voltage at the constant frequency of 1 kHz. Electrical impedance is the ratio of the variation in the current with the changes in voltage. The relative amplitudes along with phase shift make up this value. This phase angle can deliver a complex resistance. EIS measurement is also able to provide additional parameters such as battery life, SOC, and individual charge and discharge profile of each cell [Schweiger et al., 2010]. Using this information the cells were fully charged prior to testing to avoid variations in lithiation state of the electrode materials and degeneracy in lithium distribution, which might otherwise influence thermal properties.

Physically the cells are also prepared for measurement, Figure 2-3. The cell is wrapped with thermal tape. This electrically isolates the cell as well as evenly thermally distributes input

heat. T-type thermocouples are attached on the outside surface of the thermal tape at mid-cell height. For axial measurements, thermocouples are attached in the center at the two circular ends of the cell. A flexible Kapton heater is attached to the curved or top circular surface of the cell, to heat either in the radial or axial direction, respectively. Fiberglass insulation tape is wrapped around the cell to minimize heat loss. All experiments are carried out in a vacuum chamber at -75 kPa (gage) vacuum to further reduce heat loss. The cell under test is suspended on thin paper arms to minimize thermal conduction loss through surface area contact.

Figure 2-3 Cell preparation steps prior to testing

Figure 2-4 (a) and (b) show images of the cell with the flexible heater and thermocouples in place inside the vacuum chamber. A Keithley 2612A sourcemeter is used for supplying heating current and measuring voltage. The thermocouple output is sampled at 2 Hz using a National Instruments (NI) 9213 24-bit thermocouple module within an NI cDAQ-9171.

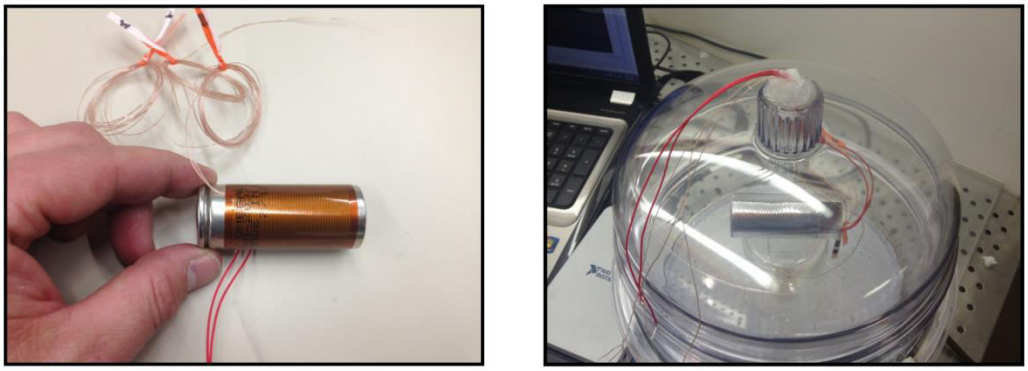

(a) (b)

Figure 2-4 Images of the experimental setup showing (a) the Li-ion cell with flexible heater and thermocouples, (b) the instrumented Li-ion cell inside a vacuum chamber for thermal measurements

The data acquisition is controlled using NI's LabVIEW software. Electrical resistance of Kapton heaters used in this work is measured at temperatures between 25 °C and 50 °C. There is less than 0.1% change in resistance, which shows that the temperature coefficient of resistivity is negligible. This ensures constant heat flux into the battery even as the temperature rises. Each experiment is stopped once the cell temperature reaches a value that is 10°C below the manufacturer's rated thermal maximum for the cell. For use in the 26650 and 18650 cells, the maximum operating temperature was limited at 55°C. The mass density of each test sample is determined separately by measuring its volume using Vernier calipers and its weight using a scale balance. Mass density of the 26650 and 18650 cells used is measured to be 2285 kg m^{-3} and 2362 kg m^{-3} respectively. Once mass density is known, the experimental setup is used for measuring thermal conductivity and heat capacity of 26650 and 18650 cells. Radial and axial thermal conductivity and heat capacity are determined by comparison with analytical model, which is described next.

Results and Discussion

Analytical Model Validation

Figure 2-5 (a) presents the temperature predicted by the radial model (equation (4)) as (a) a function of time for r = R, and (b) as a function of r for t = 2000s. Results from a transient finite-element simulation are also shown for comparison. There is excellent agreement between the two. Similar agreement is observed between the axial model (equation (8)) and a finite-element simulation carried out in ANSYS, both as function of time and z, as shown in Figure 2-6. As expected, the computation time of the analytical model, roughly a few seconds, is much less than the finite-element simulation, roughly several minutes, particularly since there is no set up time needed for modeling and meshing the geometry. Moreover, the analytical model provides a fundamental understanding of the thermal physics that is not apparent from the finite-element simulations. Figure 2-5 (b) shows a significant, non-linear, temperature gradient within the cell between r = 0 and r = R for thermal properties representative of Li-ion cells, as described in the next section.

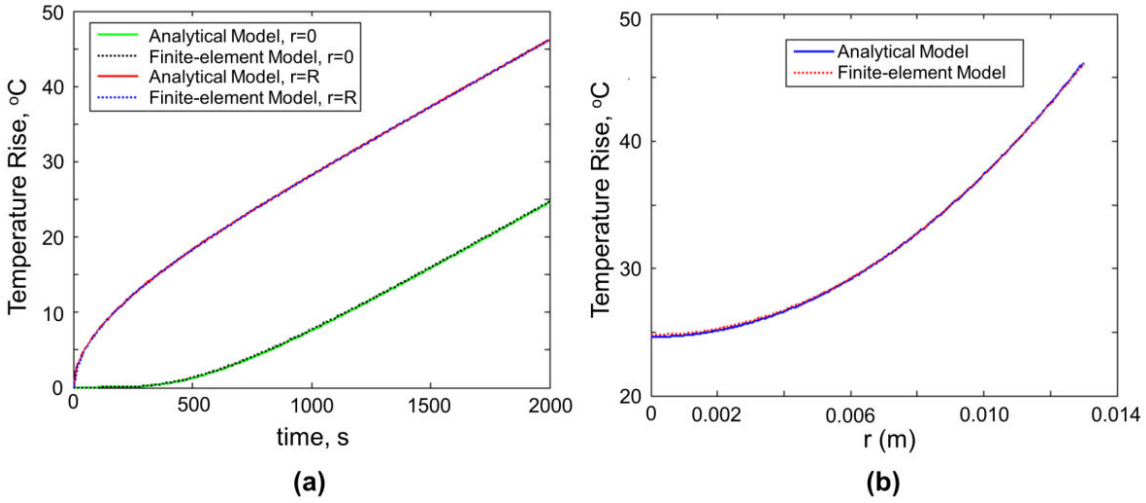

Figure 2-5 Comparison of radial model with finite-element thermal simulation; (a) is a combination of the radial model's on top with the axial model's on bottom, (b) shows the temperature profile across the cell with varying radius for a radial experiment

The presence of a temperature gradient within the cell is important to consider when evaluating the electrochemical design and operation of the cell, as well as for modeling of thermomechanical stress generation. Figure 2-5 and Figure 2-6 assume representative values for the thermal properties of the geometry under consideration.

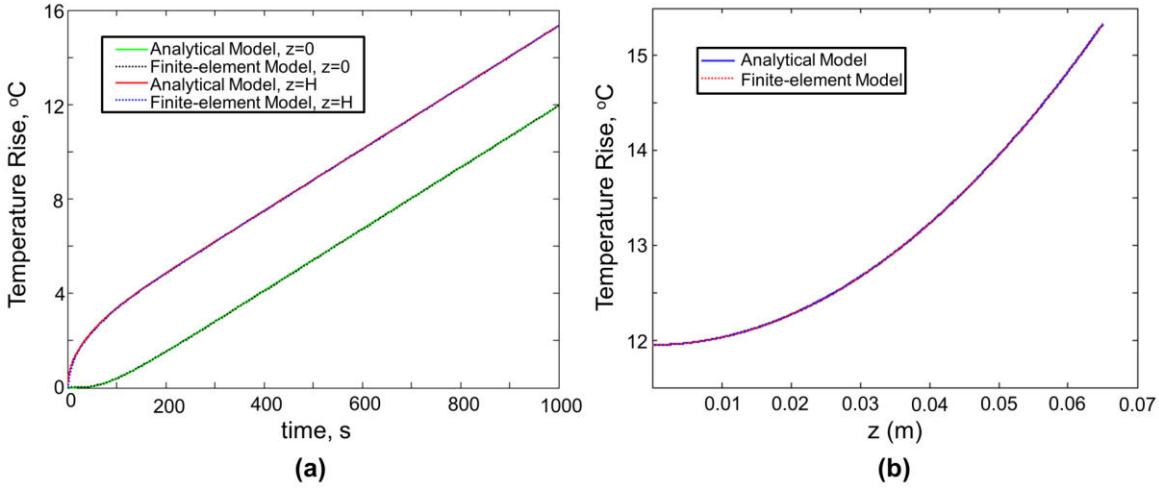

Figure 2-6 Comparison of axial model with finite-element thermal simulation

Excellent agreement between analytical model and finite-element simulations shown in Figure 2-5 and Figure 2-6 is verified for a typical range of expected values.

Measured Properties for 26650 and 18650 cells

Experimentally measured temperature curves for 26650 cell are shown in Figure 2-7 for the radial and axial heating tests, measured at mid-height on the outside surface of the cell, r = R, and at the end of the cell opposite to the heater, z = 0, respectively.

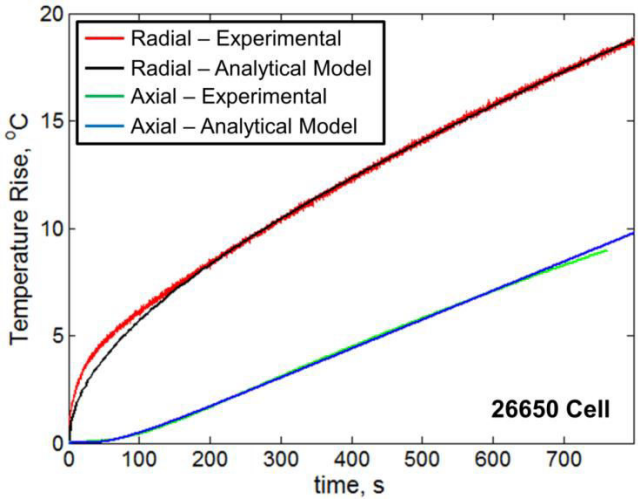

Figure 2-7 Comparison of experimental data and analytical model for radial and axial thermophysical property measurements for 26650 cell

Figure 2-8 shows similar curves for a 18650 cell. Radial and axial measurements for 26650 as well as 18650 cells excellent agreement with the analytical model presented in the previous section, including in the transient portion of the temperature curves. As expected from the model, the axial data is concave whereas the radial data is convex. The measured temperature curves comprise a linear term, a constant shift, and an exponentially decaying component.

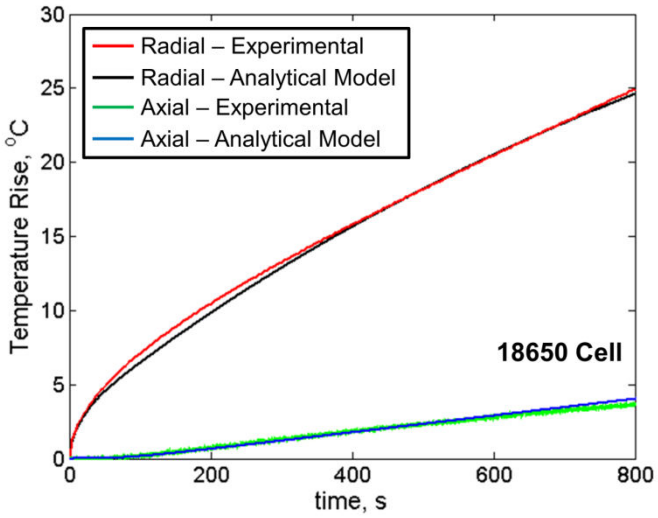

Figure 2-8 Comparison of experimental data and analytical model for radial and axial thermophysical property measurements for 18650 cell

The slope is always positive, whereas the intercept is positive for the radial case, and negative for the axial case. This corresponds to positive and negative values of the second term in equations (4) and (8) respectively. Through comparison of the slopes and intercepts of the temperature curves with analytical model, the radial and axial thermal conductivities of the 26650 and 18650 cells are determined, and are summarized in Table 2-1. These values are determined such that the mean square error between experimental data and the analytical model is minimized. There is a two orders-of-magnitude difference between the radial and axial thermal conductivities for both 26650 and 18650 cells, indicating strong anisotropy in the thermal conduction within the cells.

Table 2-1 Measured thermophysical properties of 26650 and 18650 cells

	k_r ($Wm^{-1}K^{-1}$)	k_z ($Wm^{-1}K^{-1}$)	C_p ($J\ kg^{-1}K^{-1}$)
26650	0.15	32	1605
18650	0.20	30	1720

Measured heat capacity for the axial test is somewhat lower than the radial test (eg.1605 $Jkg^{-1}K^{-1}$ vs. 1895 $Jkg^{-1}K^{-1}$ respectively for 26650 cell). The small difference is attributed to the fact that since temperature measurement in the radial experiment is made at the center plane of the cell, z = 0.5H, it does not account for the presence of metal tabs at the battery ends. When the metal tabs are taken into account in the axial experiment, the measured heat capacity is somewhat lower due to the lower heat capacity of metals compared to the organic solvents that constitute the battery electrolyte [Lide *et al*., 1994; Touloukian *et al*., 1970]. The axially measured heat capacity is believed to be more accurate due to the tabs being taken into account.

Thermal conductivity values measured in this work are somewhat lower than previous measurements on individual cell constituents such as the electrode-separator assembly that report out-of-plane thermal conductivity of around 1-3 W/mK [Maleki *et al*., 1999] and 0.3-1.6 W/mK [Chen et al., 2005]. This is possibly because the current experiments take into account multiple thermal contact resistances that exist in an actual cell but not in an isolated sample. By accounting for such thermal contact resistances, measurements reported in this work are expected to be more realistic than previous work. Even though both 26650 and 18650 cells used in this work employ the $LiFePO_4$ chemistry, there is a small variation in the measured property values. This is possibly because the number of interfacial thermal resistances in the two cells may be slightly different due to the different aspect ratios. Moreover, small variations in the materials and thicknesses for various other components such as metal tabs, container, etc. may also contribute to the small difference between the two.

The measured anisotropy in thermal conductivity is believed to originate from the Swiss roll-like arrangement of the anode-separator-cathode inside the cell. Heat flow in the radial direction encounters several material interfaces, whereas in the axial direction, heat flows in mostly a single material without encountering many material interfaces. It is also possible that the thermal conductivities of the anode, separator, and cathode materials might themselves be

anisotropic with an out-of-plane thermal conductivity value that is much smaller than the in-plane component. It is well-known that the in-plane thermal conductivity of thin film materials is much higher than the out-of-plane component [Cahill *et al.*, 2002].

The strong anisotropy of the thermal conductivity has important implications in the thermal design of the cell. Assumption of a single-valued thermal conductivity will result in either severe underprediction or overprediction of cell temperature depending on whether the axial or the radial thermal conductivity value is used. This is shown in Figure 2-9, which compares the temperature contour inside a 26650 cell for the anisotropic case to isotropic cases assuming either the axial or the radial thermal conductivity value. In each case, a constant volumetric heat generation rate within the cell body and a constant convective heat transfer coefficient on the cell surfaces are assumed. The temperature field is determined using a finite-element simulation. Figure 2-9 (c) shows that the anisotropic assumption results in a peak temperature rise of 24 K, whereas the isotropic assumption, using the radial and axial thermal conductivity values result in peak temperature rise of 33 K and 11 K respectively Figure 2-9 (a). Moreover, the isotropic case using the axial thermal conductivity value incorrectly predicts a very uniform temperature distribution within the cell. As a further illustration, simulations are carried out to predict the maximum cell temperature by measuring the outside temperature of the cell. Simulations indicate that if the measured temperature at the cell's outside body is 45 °C at a 25 °C ambient, then an isotropic thermal conductivity model assuming a value equal to the radial or axial thermal conductivity will predict a core temperature of 78 °C or 46°C, whereas the correct core temperature, determined using an anisotropic thermal conductivity model will be 74 °C. The temperature contours predicted by the isotropic models will also be incorrect.

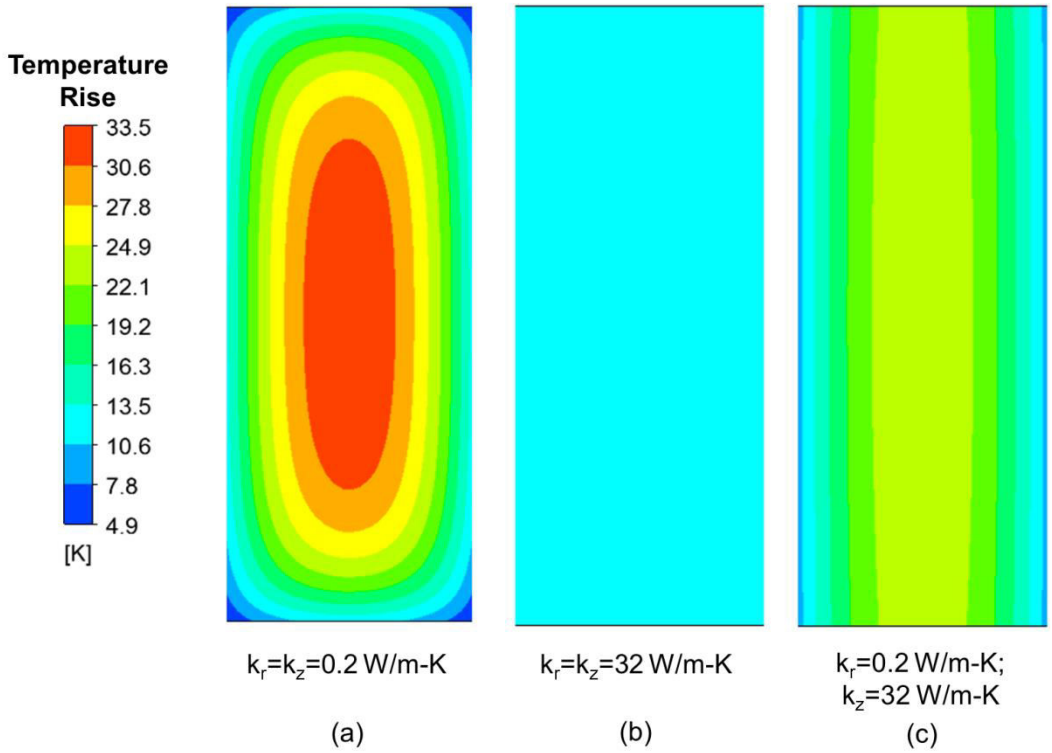

Figure 2-9 Simulations showing the effect of the thermal conductivity assumption on expected temperature profile within a 26650 cell, (a) and (b) are with isotropic thermal conductivity, assuming either the measured (a) radial or (b) axial value, (c) is with anisotropic thermal conductivity

While the first isotropic case described above will lead to un-necessary overdesign of the thermal solution, the other case might lead to safety problems due to under-prediction of peak temperature. The use of anisotropic thermal conductivity with accurately measured values is most appropriate for thermal design of the cell. It is also important to consider the importance of thermal conduction anisotropy in multi-physics cell design where other physical phenomena such as electrochemical reaction kinetics, charge/discharge rates, mechanical stresses, etc. depend on the temperature distribution. When such phenomena are themselves space-dependent within

the cell, it is important to accurately predict the spatial temperature distribution by recognizing the anisotropy in the thermal conductivity.

Thermocouple Placement

To ensure uniform heat distribution beyond the assistance of the thermal tape, three thermocouples were placed along the radial/curved face of the cell at ¼ the height, ½ the height, and ¾ the height. Radial heating was applied to the cell and the temperature rise was recorded as a function of time. Figure 2-10 shows a diagram and the temperature plot for this experiment.

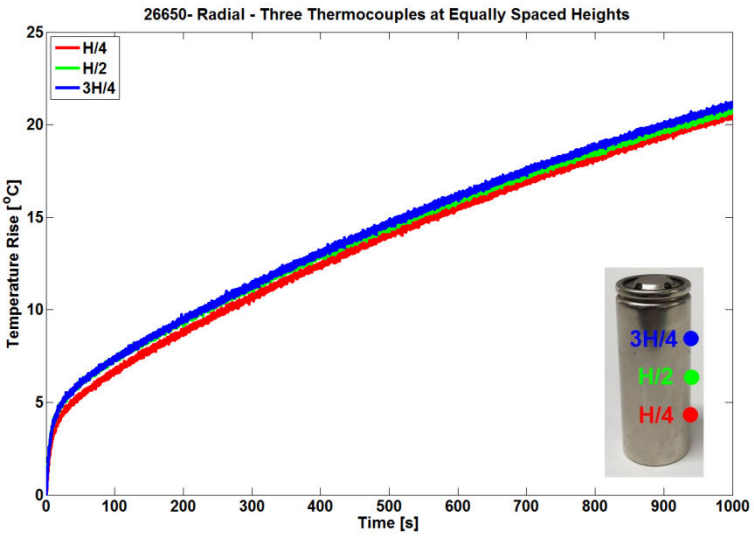

Figure 2-10 Radial heating with three thermocouples placed underneath the heater evenly spaced over the height of the cell

This test validates that the thermal agreement and minimal temperature variation at various spots along the surface is negligible. Along similar lines, the axial flow of heat can be seen in Figure 2-11.

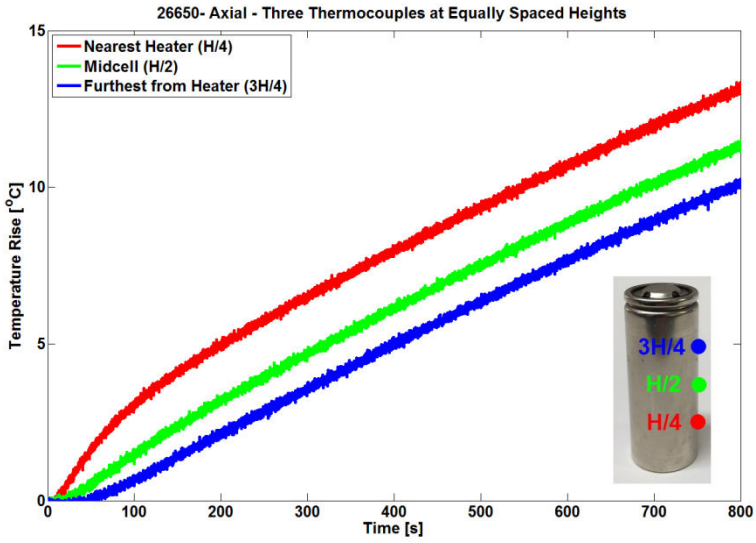

Figure 2-11 Axial heating with same three thermocouples that show the progression and temperature rise in the cell from heater to opposite end

In this experiment, heat was applied in the axial direction. Keeping the aforementioned three thermocouples in their same places, their temperature response was again recorded versus time. The heater was attached to the bottom as the cell is shown in the figure. It is clearly seen that the bottom, then middle, then furthest thermocouple away from the heat, rise respectively.

Uncertainty Analysis

T-type thermocouples used in the current work are accurate to 0.25 °C, which contributes approximately 2% uncertainty in thermophysical property measurements. Other measurements such as geometry, electric current, and voltage, etc. have much lower relative uncertainty. A significant uncertainty in the thermophysical property measurements arises from heat loss into the insulating layer surrounding the test cell. Since all tests described in this paper are transient in nature, heat generated in the heater, whether axial or radial, flows either into the cell, or into the surrounding insulation layer. The ratio of heat flows to the two thermal regions is given by the ratio of their thermal masses. Thus

$$\frac{Q_{insulation}}{Q_{cell}} = \frac{\left(m \cdot C_p \cdot \frac{d\theta}{dt}\right)_{insulation}}{\left(m \cdot C_p \cdot \frac{d\theta}{dt}\right)_{cell}} \quad (9)$$

An experiment is carried out to determine the importance and effect of insulation and a vacuum for future experiments. First was to test a cell in an insulated temperature chamber but without a vacuum. This plot can be seen in Figure 2-12.

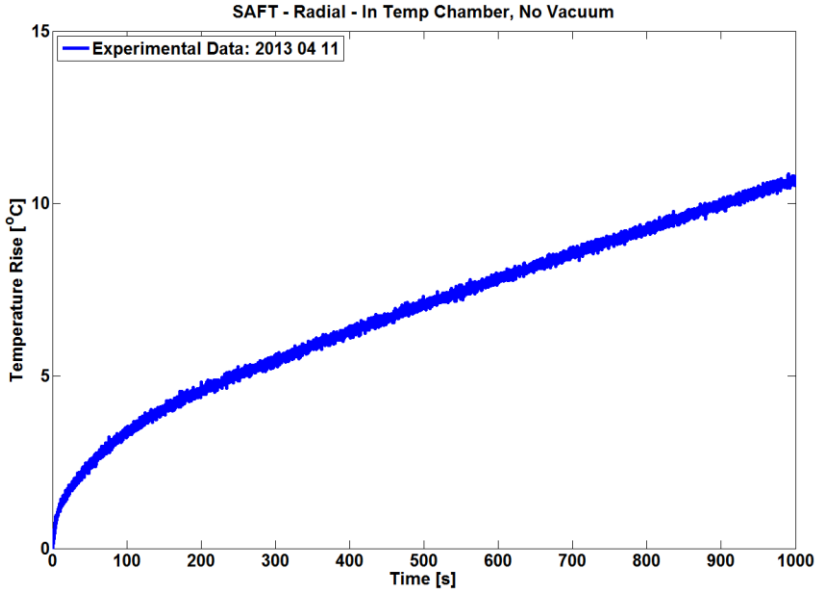

Figure 2-12 Experimental Data with cell tested inside an insulated temperature but without vacuum

This plot shows an expected temperature rise, however even while being insulated the non-linear shape of the temperature plot can be seen. This is believed to be the impact of free convections. Based on this test it was decided that all future experiments would be performed in a vacuum.

Next while under vacuum it was investigated the need for further control of heat into the cell. This would determine if there was a need for insulation. Two identical tests were performed

on a cell; one with radially applied heat to a cell with only thermal tape around the metal, while the other was the same cell with an added single layer of insulation. Figure 2-13 shows the discrepancy of the temperature rise at the same location.

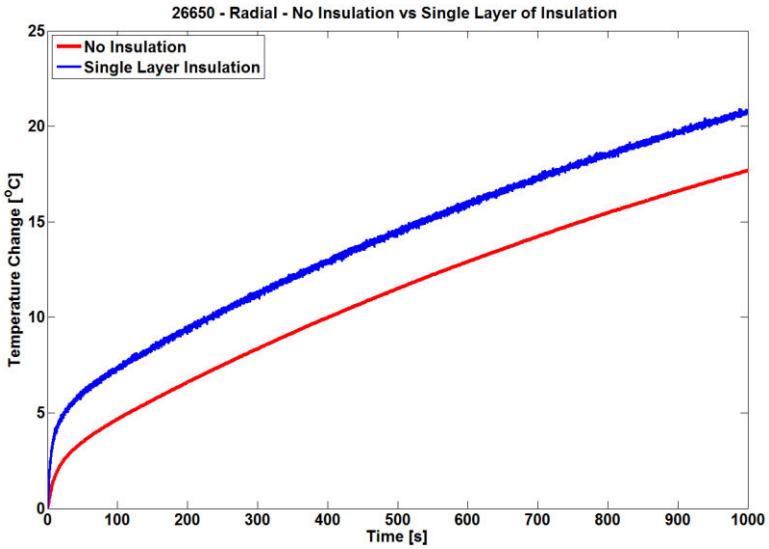

Figure 2-13 No insulation vs single layer of insulation during 26650 radial heating test

This plot shows the need for further control of the heat into the cell. Following this test, all experiments were performed with at least on layer of insulation. Figure 2-14 exhausts this point to determine if multiple layers of insulation would be required.

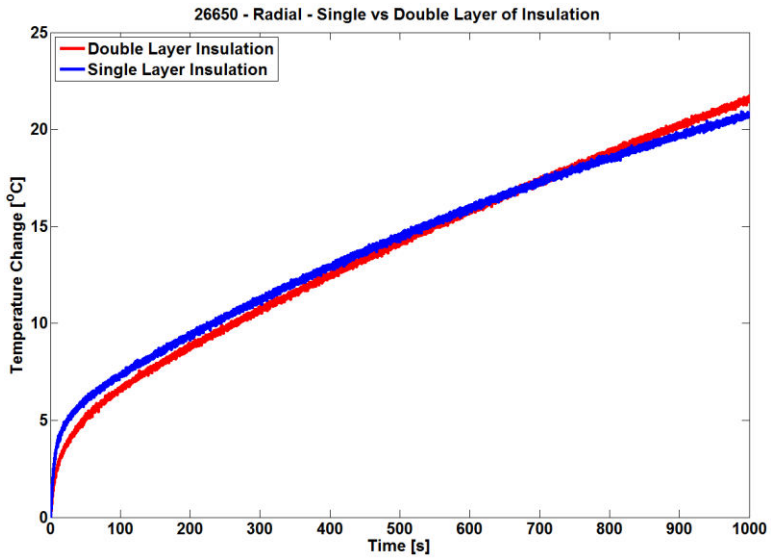

Figure 2-14 Single vs double layers of insulation during a radial heating test

The previous cell was tested with its current setup with a single layer of insulation. Immediately following and being allowed to cool, the same radial heat was applied however this time a second layer of insulation was applied. The temperature rise in this case was nearly identical, which shows that minimal temperature rise factoring in the additional mass from another layer of insulation, determined that additional heat lost was negligible and only a single layer of insulation would be required for future cell testing.

Heat capacity of the insulation is obtained from the manufacturer. From equation (9), it is found that heat flow into the insulation is very small, around 2% of the total heat generated by the flexible heater. As a result, this introduces additional uncertainty of around 2%. The effectiveness of insulation used in this work is further confirmed by the observation that a thermocouple suspended in vacuum just outside the heater does not register appreciable temperature rise, Figure 2-15.

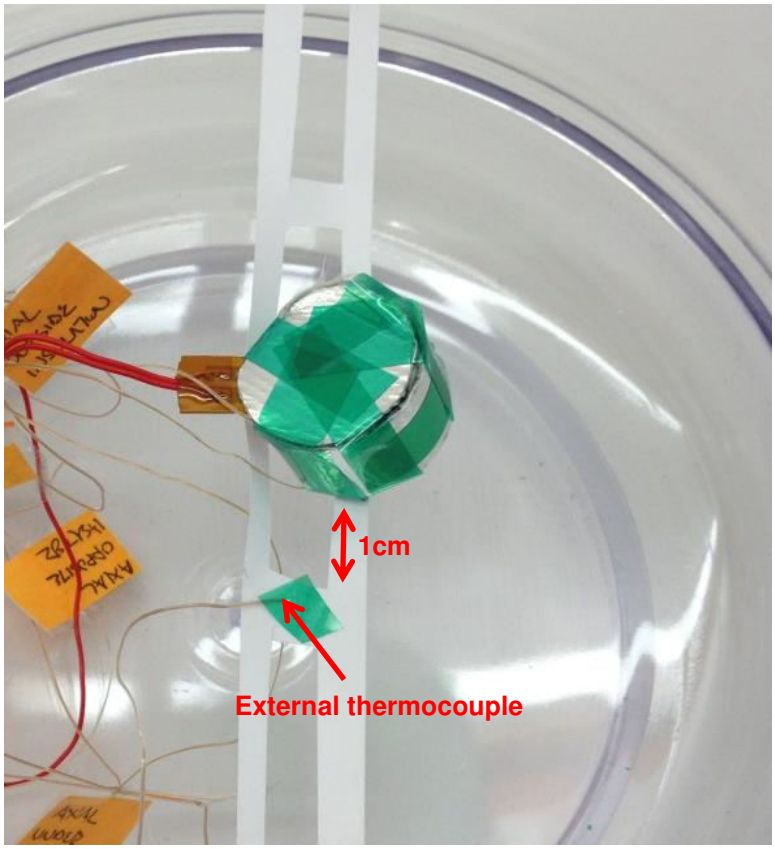

Figure 2-15 Thermocouple in air next to active test to record temperature rise

Figure 2-16 shows a plot of the setup in Figure 2-15 and how the temperature rise shows how heat does not spread inside the vacuum chamber, thereby minimizing error and heat loss.

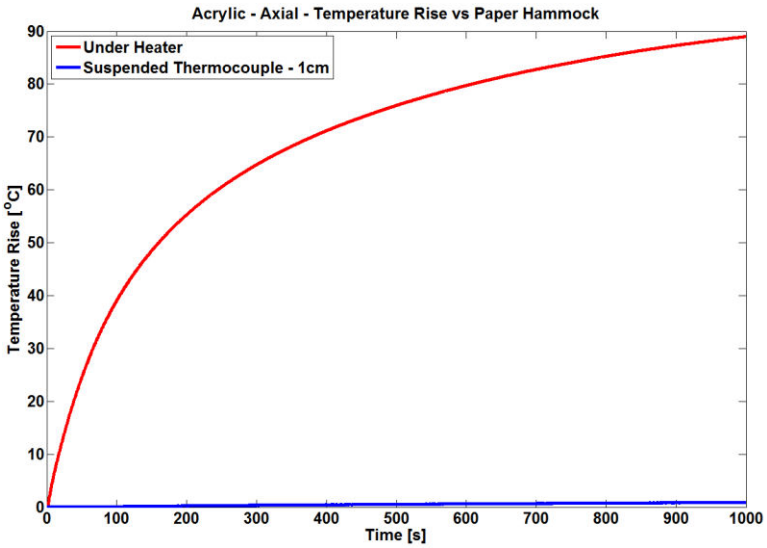

Figure 2-16 Thermocouple under heater and next to active test, data from Figure 2-15

A finite-element thermal simulation is carried out to determine the error introduced by heat conduction by the thin thermocouple and power supply wires. Simulation results indicate that due to the small diameter of the wires, less than 0.1% heat generated in the heater is lost in thermal conduction through the wires.

When accounting for all sources of uncertainty listed above, the total measurement uncertainty in the thermal conductivity and heat capacity values are estimated to be around ±5%, also shown in Table 2-1.

Conclusion

This paper presents a simple method for measurement of thermophysical properties such as thermal conductivity and heat capacity of cylindrical Li-ion cells. By measuring the thermal response of the cell to an adiabatic heat into the cell in either radial or axial direction, it is possible to determine both radial and axial thermal conductivities in addition to heat capacity. The analytical model agrees well with finite-element simulations and has been validated against experimental data. The radial thermal conductivity is as low as 0.15-0.2 W/mK for 26650 and 18650 cells. Measurements indicate strong thermal anisotropy with both cells tested in this work.

The measured radial thermal conductivity is less than 1% of the measured axial thermal conductivity for 18650 and 26650 cells respectively. This alarmingly high anisotropy has several important implications both for thermal modeling as well multi-physics modeling of physical phenomena that occur in a Li-ion cell. Not accounting for such anisotropy may lead to severe under-design or over-design of a Li-ion cell. By providing thermal property measurements, as opposed to thermal resistance measurements, this work contributes to a fundamental understanding of thermal transport within a Li-ion cell..

Prismatic and Pouch Cell

26650 and 18650 cells are among the most popular form factors for li-ion cells; however it is prudent to extend the same principals and methodology to other shapes. Rectangular shaped cells come in two styles: prismatic and pouch. Prismatic cells are encased in an external metallic casing that provides protection from the outside elements and conditions Pouch cells, sometimes mistakenly called prismatic, have similar internal materials but are encased only in a soft sided pouch. This pouch provides advantages and disadvantages. The soft exterior is more susceptible to punctures and tears, however it does allow for higher energy and power density packing. For this, prismatic cells are typically used in more aggressive environments such as laptops and cell phones, while pouch cells are more likely used in less extreme situations such as hybrid electric vehicle battery packs. Described below is the analytical model used to characterize a number of different rectangular cells along with experimental results and findings.

Analytical Model

This section derives an analytical model for the expected temperature profile as a functions of time as a rectangular cells is subjected to heat. This model will follow very closely to that of the axial case for the cylindrical model. Rectangular cells are constructed in the same manner as cylindrical cells. Internal components are assembled in the same stacking sequence, however instead of being wrapped around a spindle; rectangular cells are wound around two

spindles a predetermined distance apart. This results in a longer and flat profile for the cell. Figure 2-17 shows the top of a prismatic cell with the top removed.

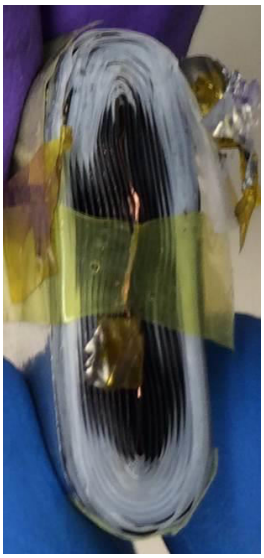

Figure 2-17 Internal components configuration of rectangular cells

Figure 2-18 show a schematic and direction nomenclature used for the rectangular cells tested in this paper.

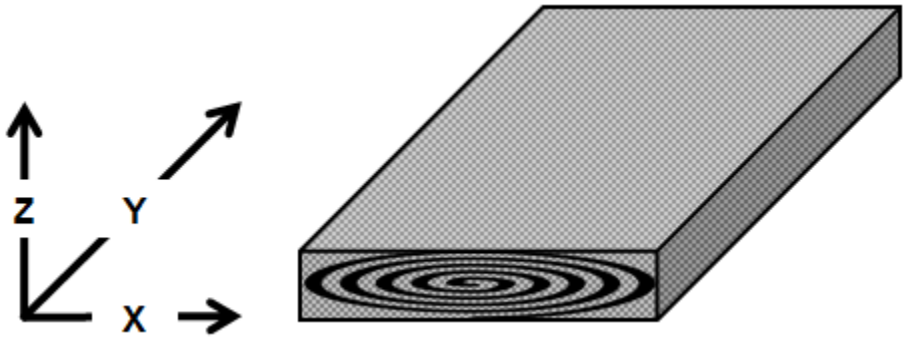

Figure 2-18 Rectangular cell direction nomenclature

Thermal conductivity is expected to be uniform and independent of temperature which gives the energy equation to be

$$\frac{\partial^2\theta}{\partial z^2} = \frac{\rho C_p}{k_z}\frac{\partial\theta}{\partial t} \quad (10)$$

where $\theta(z,t)$ is the temperature rise, and k_z is the thermal conductivity. Equation (10) is subject to the boundary conditions

$$\frac{\partial\theta}{\partial z} = \frac{1}{k_z}Q'' \text{ at } z=H \quad (11) \qquad \frac{\partial\theta}{\partial z} = 0 \text{ at } z=0 \quad (12)$$

It is assumed that at the cell is initially at ambient temperature. This problem is solved in a similar manner as the previous cylindrical problem. Again, the solution is found to comprise three components given by

$$\theta(z,t) = \theta_m(t) + s(z) + w(z,t) = \frac{Q''}{\rho C_p H}t + \frac{Q''}{2k_z H}\left(z^2 - \frac{H^2}{3}\right) + \sum_{n=1}^{\infty}\frac{(-1)^{n+1}2Q''H}{k_z(n\pi)^2}Cos\left(\frac{n\pi z}{H}\right)\exp\left(-\frac{k_z(n\pi)^2}{\rho C_p H^2}t\right) \quad (13)$$

When comparing this solution to the cylindrical case it should be noted that the difference in calculation occurs when determining the surface are for the heat flux.

Experiments

The same experimental technique for determining the heat capacity and anisotropic thermal conductivity of a cell is used for these new form factored cells. The technique will also yield thermal conductivity and heat capacity in a single experiment. Similarly the cell is subjected to a single face of adiabatic heating while temperature rise is recorded as a function of time. Four cells were tested and characterized in this section. Figure 2-19 shows each cell next to one another for size comparison. Cells were chosen to be geometrically different in order to display the flexibility of the testing paradigm and model.

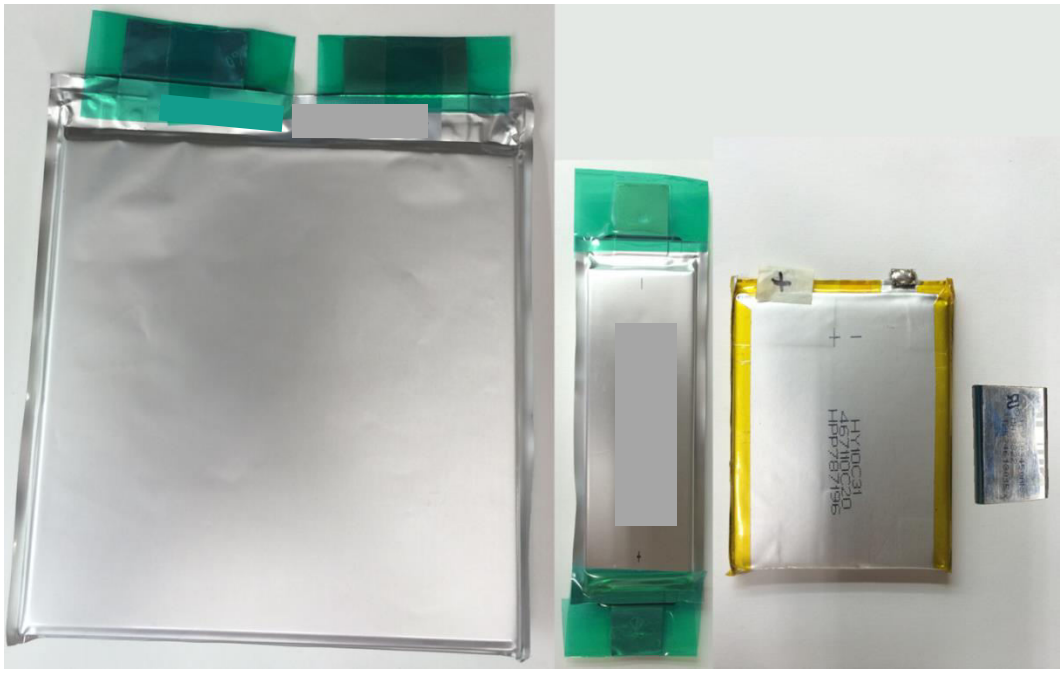

Figure 2-19 Four rectangular cells under test, from left to right, pouch large, pouch small, ICP, and Digecor rectangular cells

Prior to testing, the cells were measured and weighed, and then compared to their manufacturing specification sheet. This provided each cells mass density which is used within the model for characterization. The cells are physically prepared for measurement the same as previous tests. Figure 2-20 shows the stages of preparation of the small pouch cell.

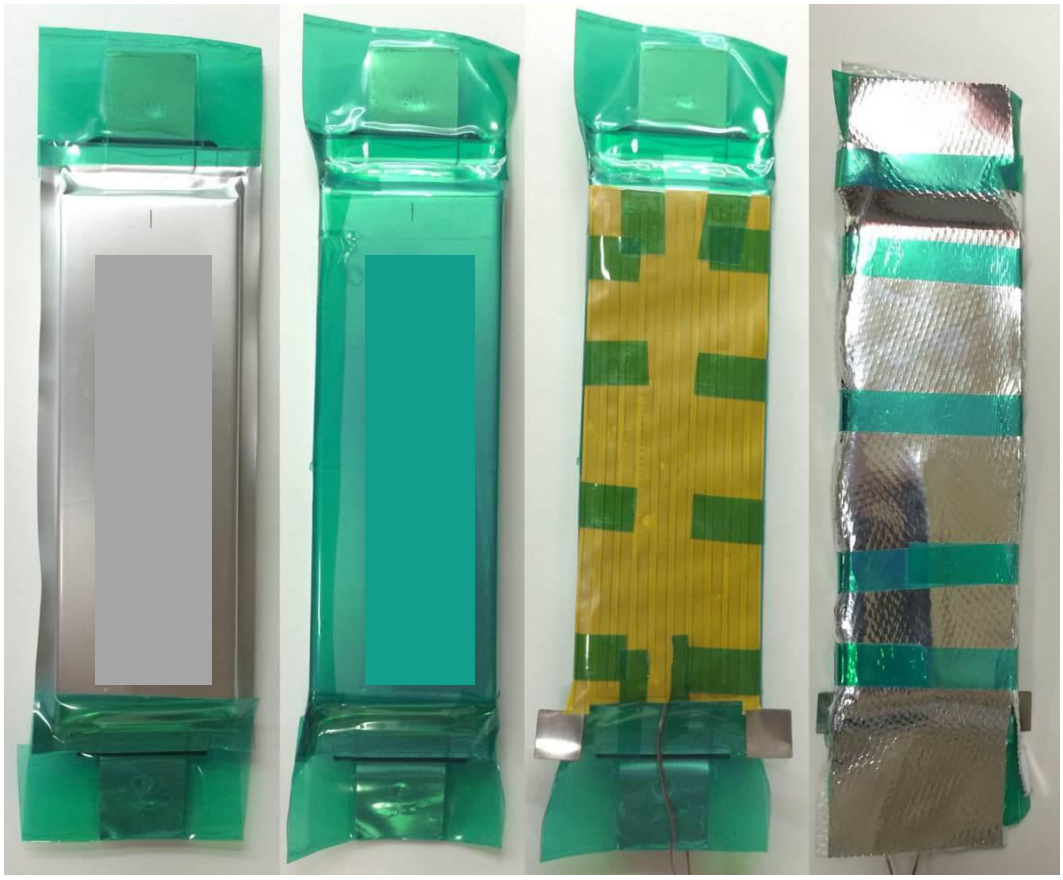

Figure 2-20 Rectangular cell setup progression

Cells are wrapped with thermal tape. This electrically isolates the cell as well as evenly thermally distributes input heat. Six T-type thermocouples are attached on the outside of each surface of the thermal tape at mid-cell height. Three flexible Kapton heaters are attached, one on each primary axis of testing. Fiberglass insulation tape is wrapped around the cell to minimize heat loss. All experiments are carried out in a vacuum chamber at -75 kPa (gage) vacuum to further reduce heat loss with the exception of the large pouch cell due to size constraints. For this test, the large pouch was tested inside an insulated temperature chamber. Inside the vacuum chamber the cells were suspended on paper supports to minimize thermal conduction loss.

The same Keithley 2612A sourcemeter is used for supplying power along with current and voltage measurements. The thermocouples output is sampled at a National Instruments (NI) 9213 24-bit thermocouple module within an NI cDAQ-9171. Each experiment is stopped once the cell temperature reaches a value that is 10°C below the manufacturer's rated thermal maximum for the cell. The dimension of each cell is listed in Table 2-2.

Table 2-2 Physical dimensions of rectangular cells

	x (mm)	y (mm)	z (mm)	Mass (g)	Density (kg/m^3)
Digecor	92.75	71.52	7.97	115.7	2188.4
ICP	49.0	33.65	10.00	36.5	2213.7
Pouch Large	218.00	198.00	9.80	840.0	1985.8
Pouch Small	112.72	40.58	11.50	133.0	2528.4

Results and Discussion

Figure 2-21 - Figure 2-24 shows experimental and model curves for all the rectangular cells in the X, Y, and Z axis. All cells in all directions provided very good agreement with the analytical model previously presented. In all cases the experimental data resulted in a concave curve plot. Property values determined are listed in Table 2-3.

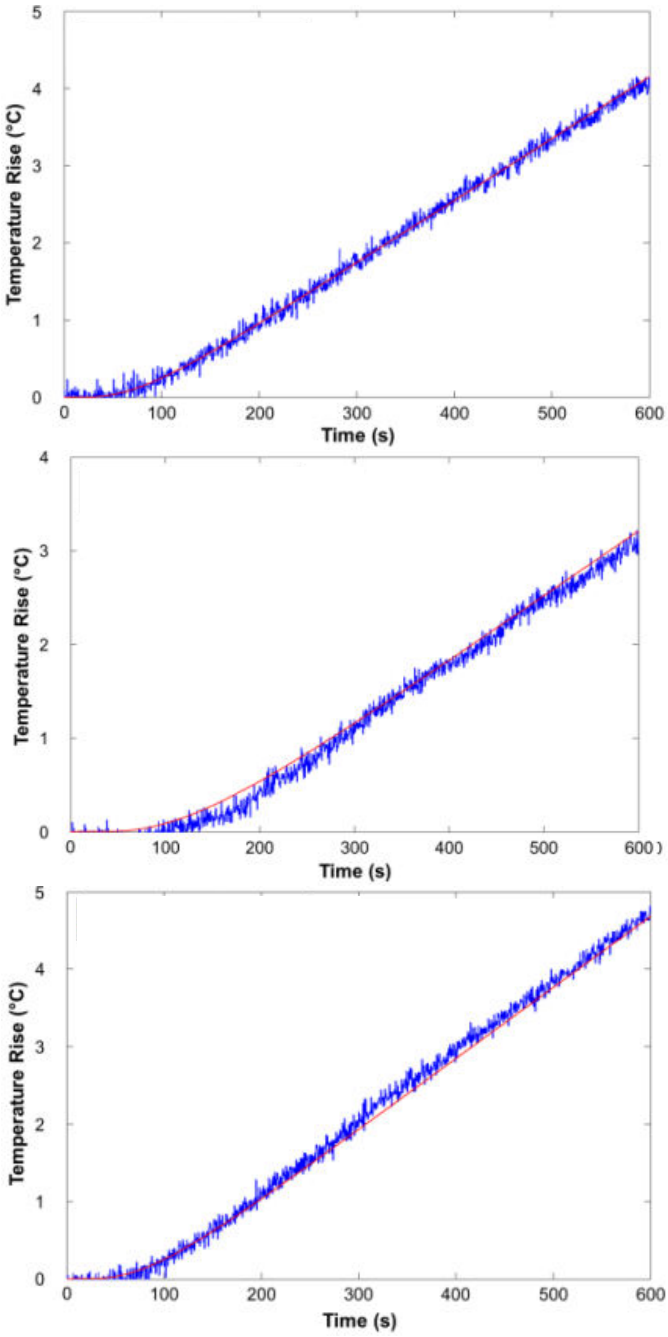

Figure 2-21 Digecor X (top), Y (middle), and Z (bottom) experimental data and model; blue line indicates test data, red line is model fit curve

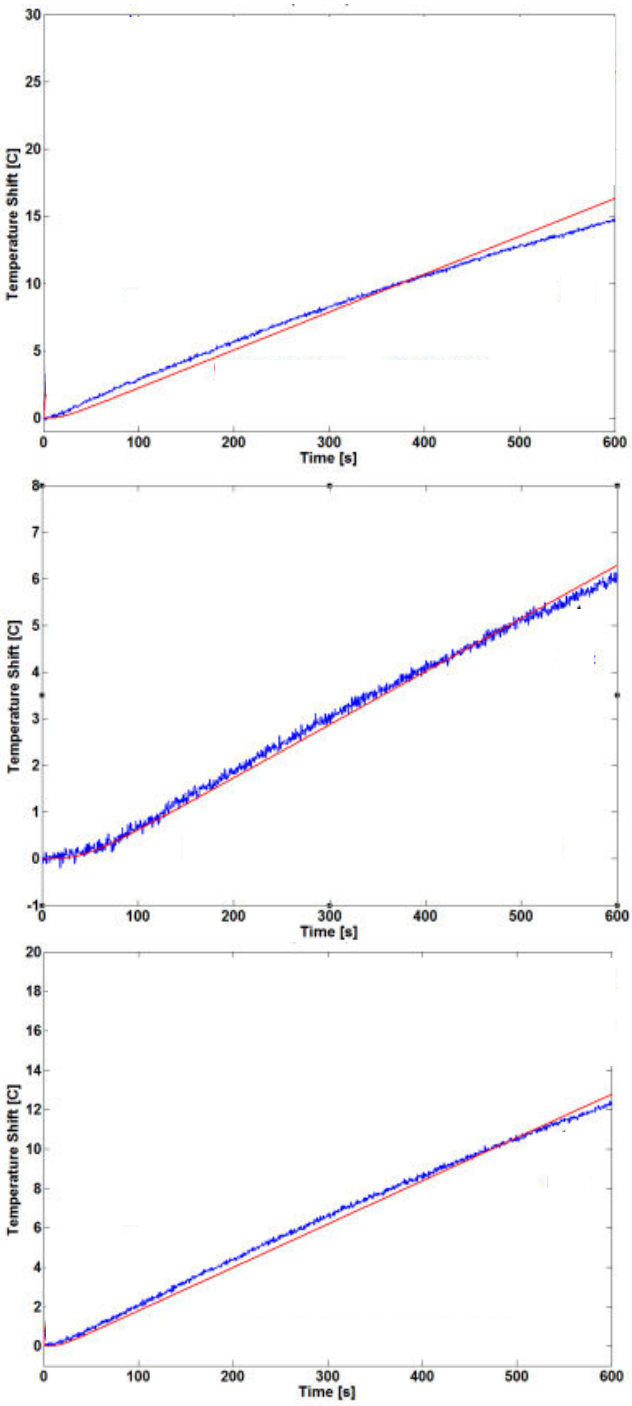

Figure 2-22 ICP X (top), Y (middle), and Z (bottom) experimental data and model; blue line indicates test data, red line is model fit curve

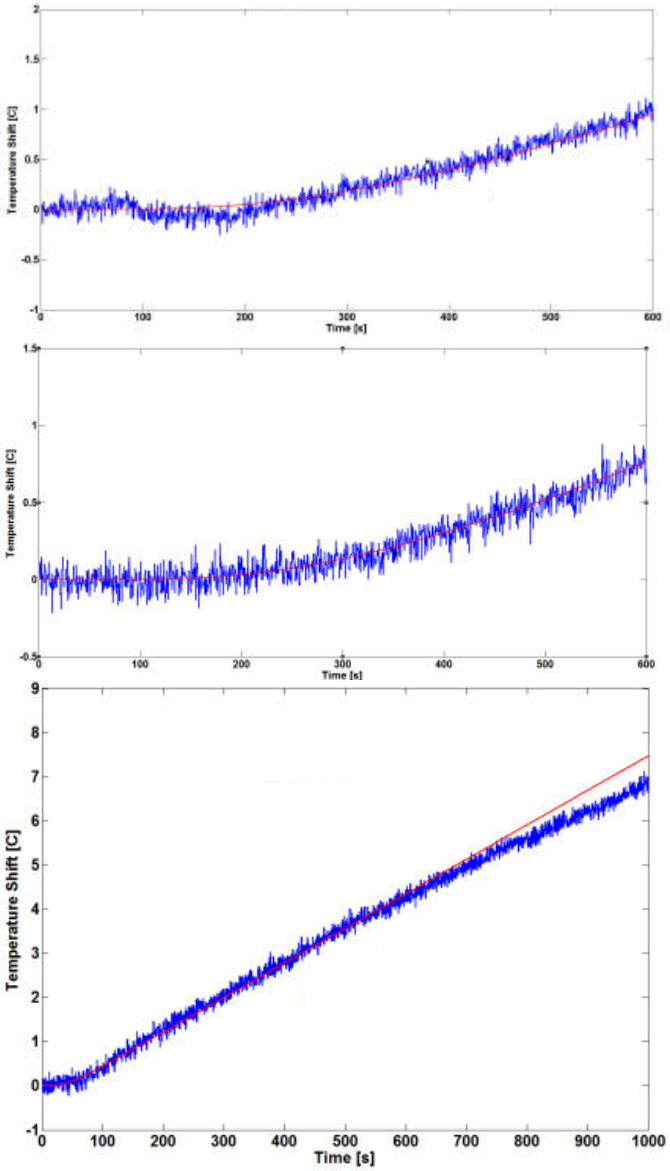

Figure 2-23 Pouch large X (top), Y (middle), and Z (bottom) experimental data and model; blue line indicates test data, red line is model fit curve

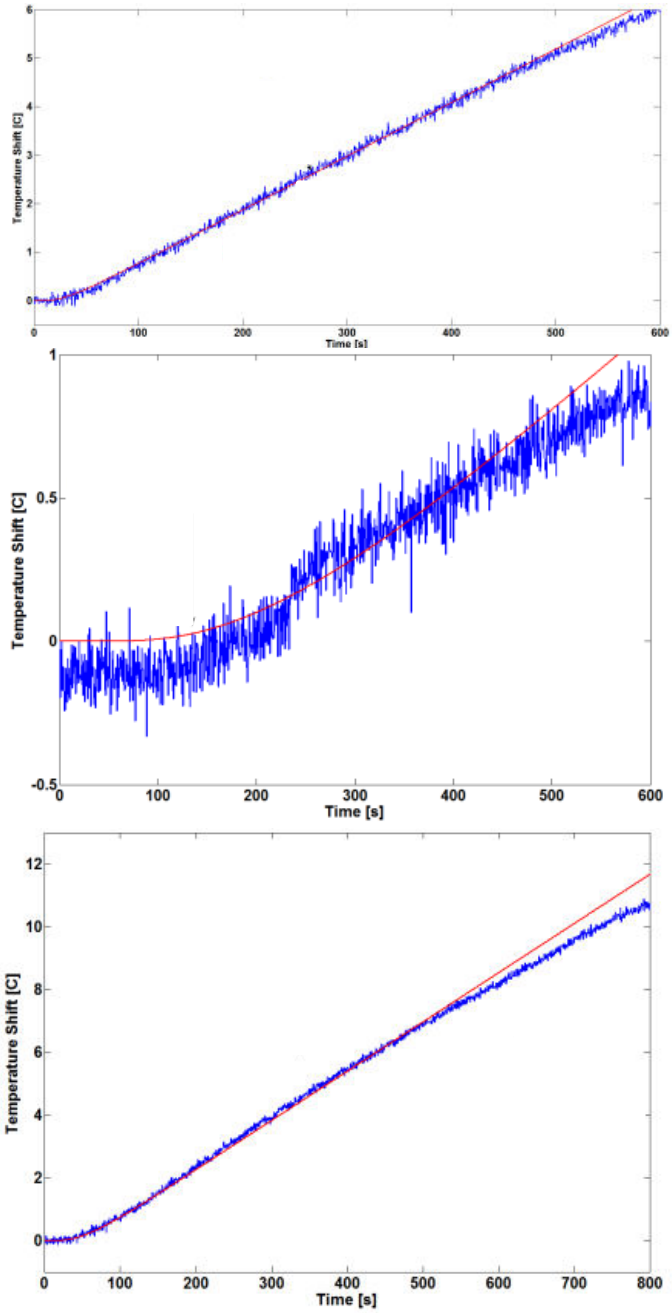

Figure 2-24 Pouch small X (top), Y (middle), and Z (bottom) experimental data and model; blue line indicates test data, red line is model fit curve

Table 2-3 Measured thermophysical properties of rectangular cells

	k_x ($Wm^{-1}K^{-1}$)	k_y ($Wm^{-1}K^{-1}$)	k_z ($Wm^{-1}K^{-1}$)	C_p ($J\ kg^{-1}K^{-1}$)
Digecor	45	45	0.40	1550
ICP	30	25	5.0	1450
Pouch Large	45	45	0.65	1000
Pouch Small	40	40	0.30	1650

Equivalent Circuit Analysis

The metal casing of the prismatic cell allows for a unique opportunity to take Fourier's heat conduction law and apply the electrical resistance analogy in the form of a thermal circuit. At first it might appear that the thin metal casing around this cell would be negligible, further analysis would prove otherwise. Similar to Ohm's law, the conduction thermal resistance is length over thermal conductivity. Below, Figure 2-25 (a), is the top view of the prismatic cell, while (b) and (c) are representative views from the y-axis and z-axis, respectively.

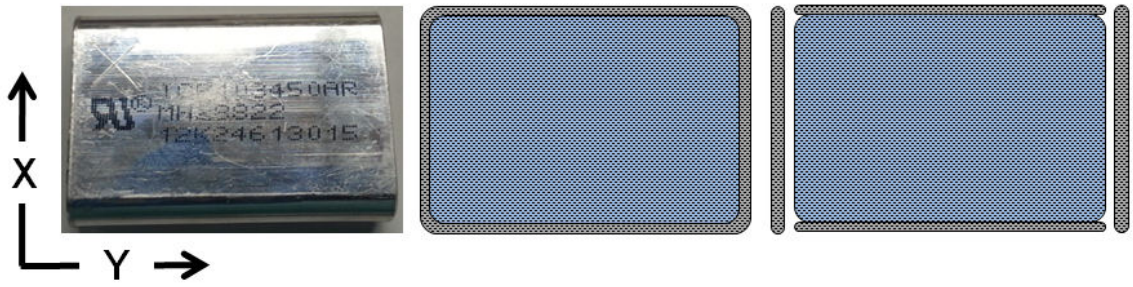

Figure 2-25 Prismatic cell thermal resistance breakdown diagram

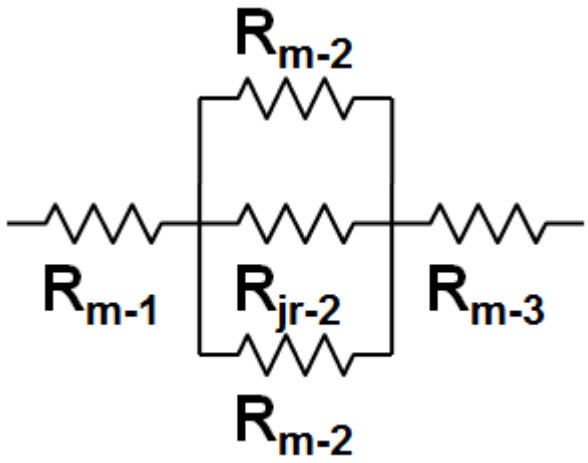

Figure 2-26 Equivalent series thermal resistance for the prismatic cell

Figure 2-26 is the series resistance assumed for Figure 2-25 (c). Upon disassembly of the cell, it is determined that all faces share the same resistance format, while only changing the values of thickness and dimensions. Thermal conductivity of the metal casing was assumed to be that of aluminum, 237 Wm-1K-1, and the internal “Jelly-roll” was assumed to be 0.20 Wm-1K-1. Thickness of the metal casing was measured to be 0.5 mm thick. Results and comparison to experimentally determined values are located in Table 2-4.

Table 2-4 Thermal resistance circuit equivalent properties compared to experimentally measured values

	k_x ($Wm^{-1}K^{-1}$)	k_y ($Wm^{-1}K^{-1}$)	k_z ($Wm^{-1}K^{-1}$)
Experimental	30	25	5.0
Thermal Resistance	29	30.5	13

Values were not in perfect agreement with experimentally determined however results were similar in nature. As expected there did also exhibit an anisotropic pattern based on the axis of rotation of the internal materials.

Manufacturers and Electrochemistry Variations

This section has expanded testing from geometrical shape of the cells, to a variety of battery chemistries, manufacturers, and manufacturing techniques. Variances in thermophysical properties are expected, however a noticeable anisotropy should still be present. Devices from a wide variety of manufacturers have been studied using a manufacturer-independent experimental method for measurement of thermal transport properties.

Custom Axial Heaters

Nine different cylindrical cells were tested and characterized in this section that resulted in new challenges during experimentation. Figure 2-27 shows the axial terminal ends of six of the cells under investigation.

Figure 2-27 Top view of 6 cells under test and their unique protrusion geometry

Each cell had unique axial geometry with regard to the connection terminals. Some cells has positive and negative at the same end, while some only had one terminal per end. This provided problematic to find readily-available consumer-off-the-shelf (COTS) Kapton heaters for axial characterization. In some cases, the surface area to apply heat was less than 1 cm^2. It would have been unsatisfactory to merely ignore these cells and measurements for this study. Early it was determined that custom heaters would be required to complete this effort. Initially hand-cut heaters were attempted. .001" thick stainless steel was chosen as the base material due to its relatively high resistivity. Overall resistance of the heater was determined by equation (14)

$$R = \frac{\rho L}{A} \qquad (14)$$

where ρ is the resistivity of the material in Ω-m, L is the length of the material in m, and A is the cross-sectional area of the material in m^2. A high resistance was required since the surface area on each axial cell was very small. First attempts for hand-made Kapton heaters are shown in Figure 2-28.

Figure 2-28 Hand-cut custom heaters

It was quickly determined that the lengths needed in order to provide adequate resistance would not be possible through this manner. An Oxford Research 355nm micro-drilling laser was utilized for making heaters to accommodate more complicated axial terminal geometries, Figure 2-29. This capability allowed for rapid, low-cost thermal testing of a wider range of batteries. Cells

with small diameters required heaters with intricate heater patterns long enough to make resistances large enough so ample power could be dissipated.

Figure 2-29 Custom heaters development in CAD drawn then laser machined

Similar challenges were present for the slim ends during the rectangular cell characterization. Figure 2-30 shows the laser machined long heaters fabricated for those experiments.

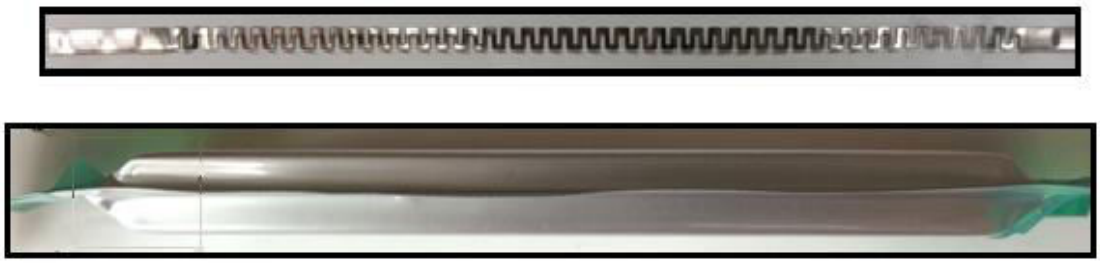

Figure 2-30 Close-up of pouch small cell with highlight of challenging area and thin sided heater

Fabrication became a relatively simple process. Each cell that could not be outfitted with a COTS heater would be measured for a custom unit. Heaters were designed in SolidWorks and converted to the native format used by the laser. Cutting for an average circle heater took about 10 minutes.

Experiments

The experimental technique described in previous sections to characterize cylindrical cells was repeated. Heat is applied at one of the axial ends along the axis of internal components

for the cell, or radially along the outer curved surface. Temperature rise was carried out using thermocouples (Omega T-type: precision 0.25 °C) placed at the ends and at the center axis of the cell. When radial heat test were performed, a thermocouple was placed mid-height on the outside radial surface of the battery and below the heater.

All cells were small enough to be tested inside the vacuum chamber at -75 (kPa). A diagram of this experimental setup is seen in Figure 2-31. Comparisons of the slopes and intercepts of the temperature curves with an analytical model provide the final values for a given cell. Each cell's geometry and mass was measured with Vernier calipers and a balance scale. The mass density of each test cell was then determined for model analysis comparison.

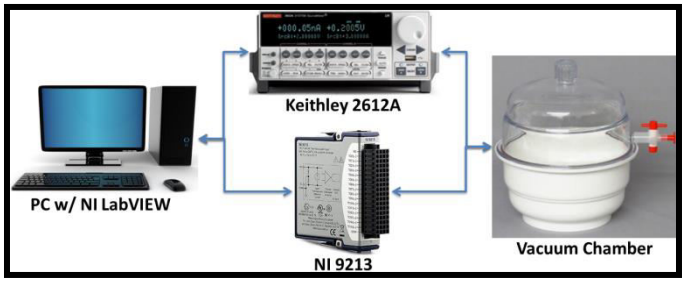

Figure 2-31 Experimental equipment setup for testing battery thermal properties

Results and Discussion

All experimental plots and corresponding models are shown below in Figure 2-32-Figure 2-40. As anticipated, the axial data plots are concave whereas the radial data is convex. The slope of both measurements is always positive. The intercept is positive for the radial case and negative for the axial case. The temperature curves are comprised of a linear term, a constant shift, and an exponentially decaying component. Comparison of the measured intercepts and slopes with an analytical model has been previously presented [Drake *et al*., 2013].

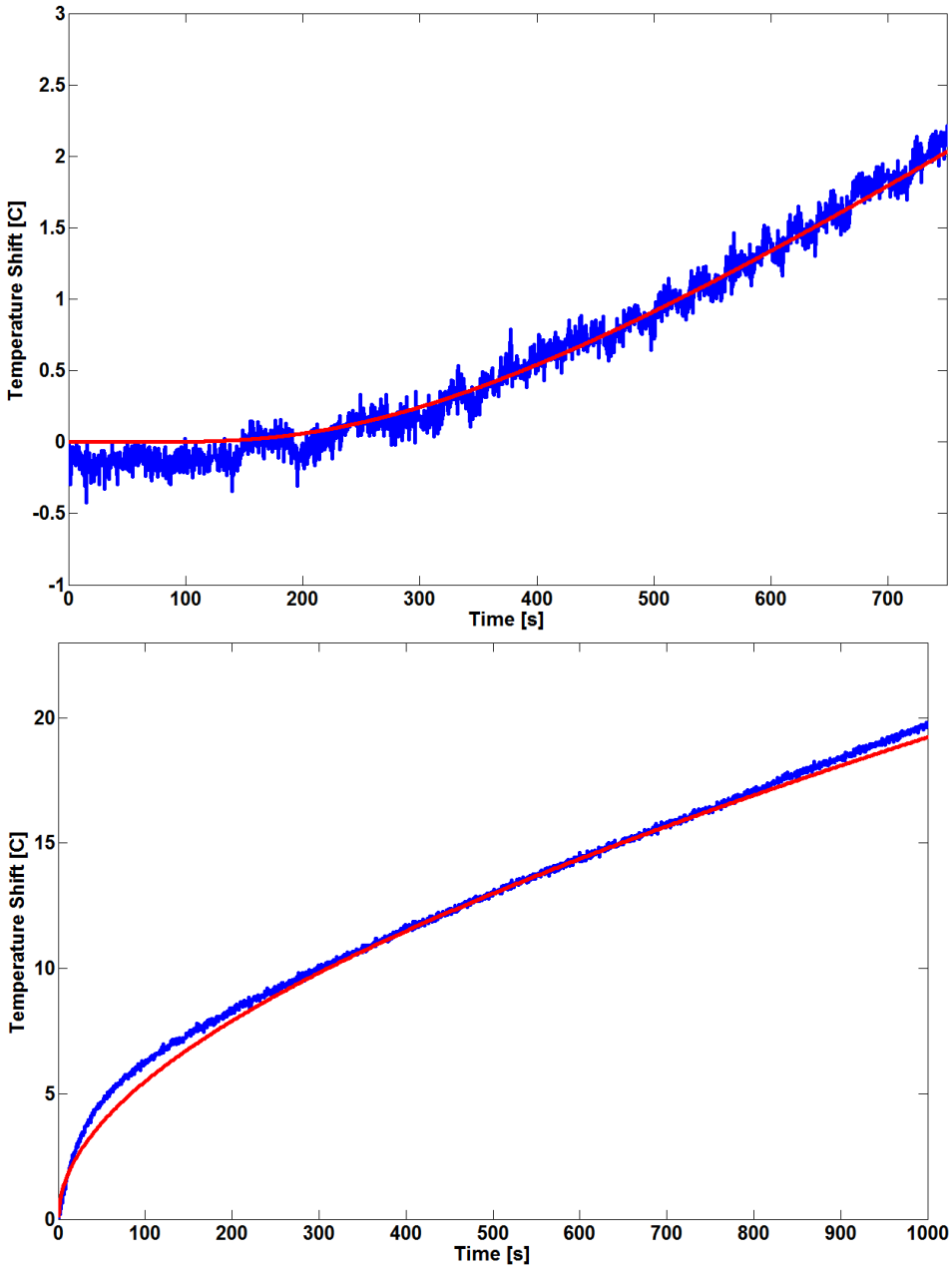

Figure 2-32 Axial (top) and radial (bottom) experimental data with accompanying model for the SAFT VL34 cell with NCA chemistry; blue line indicates test data, red line is model fit curve

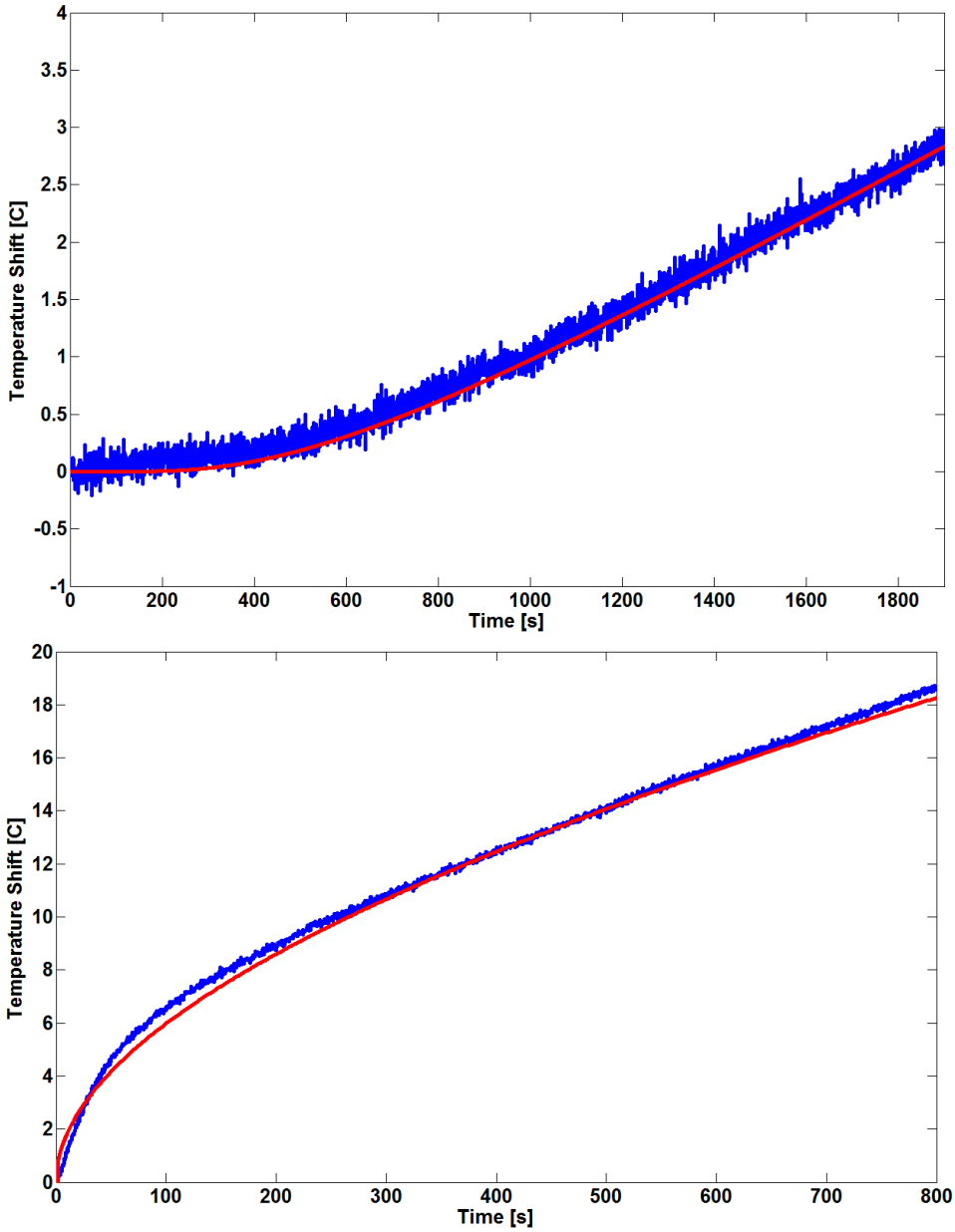

Figure 2-33 Axial (top) and radial (bottom) experimental data with accompanying model for the SAFT L30PFE cell with LFP chemistry; blue line indicates test data, red line is model fit curve

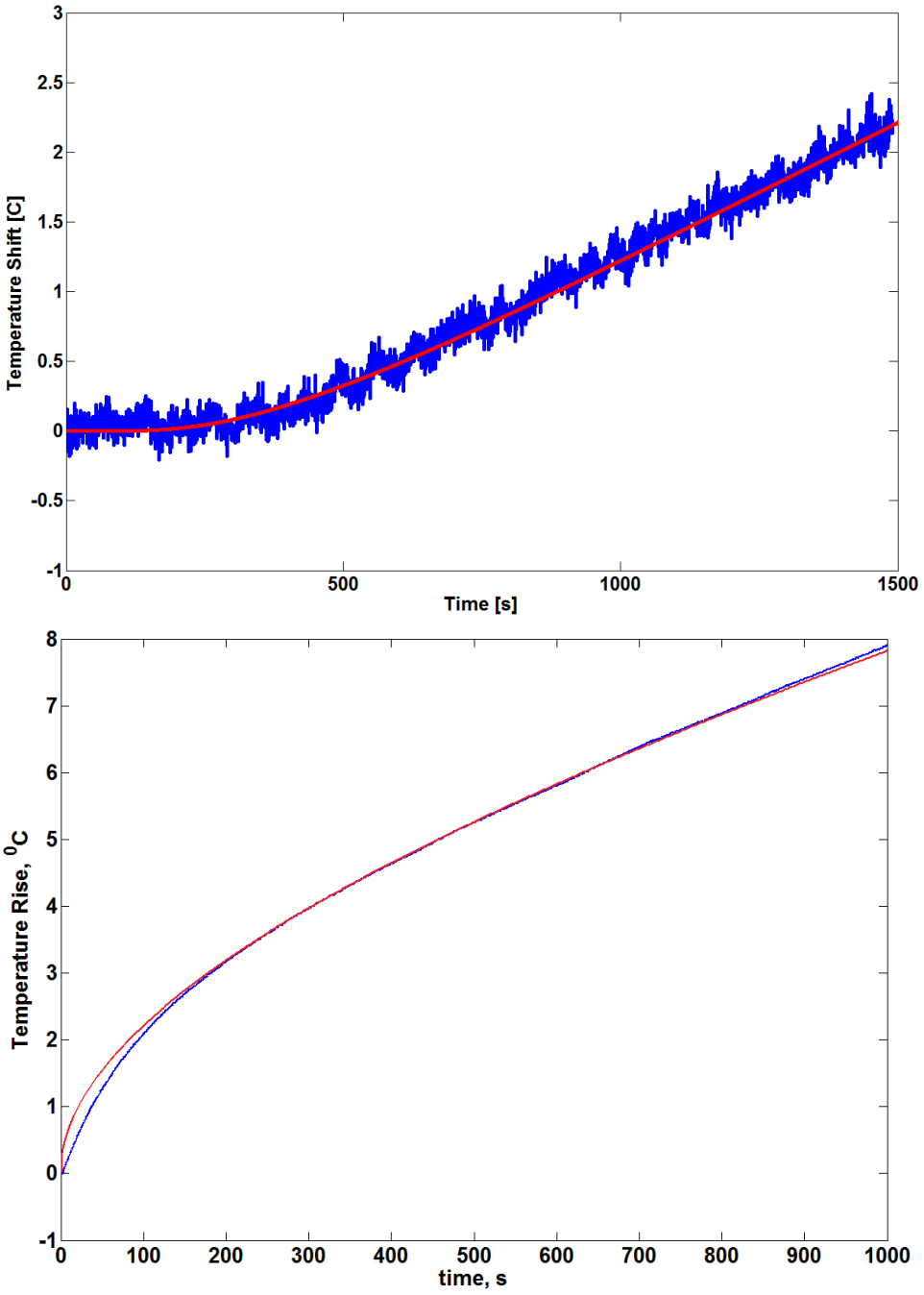

Figure 2-34 Axial (top) and radial (bottom) experimental data with accompanying model for the GAIA 27Ah cell with NCO chemistry; blue line indicates test data, red line is model fit curve

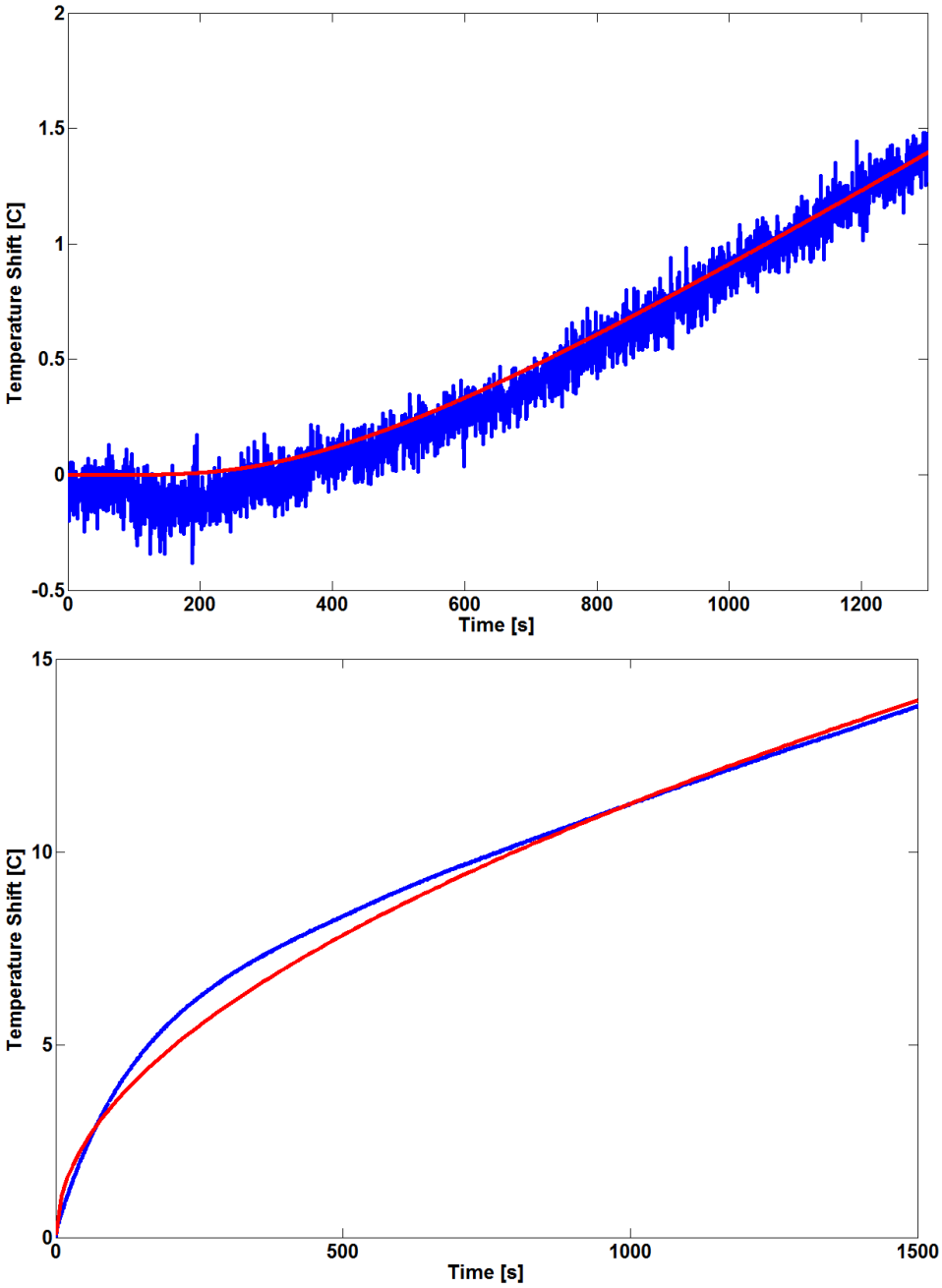

Figure 2-35 Axial (top) and radial (bottom) experimental data with accompanying model for the GAIA 18Ah cell with LFP chemistry; blue line indicates test data, red line is model fit curve

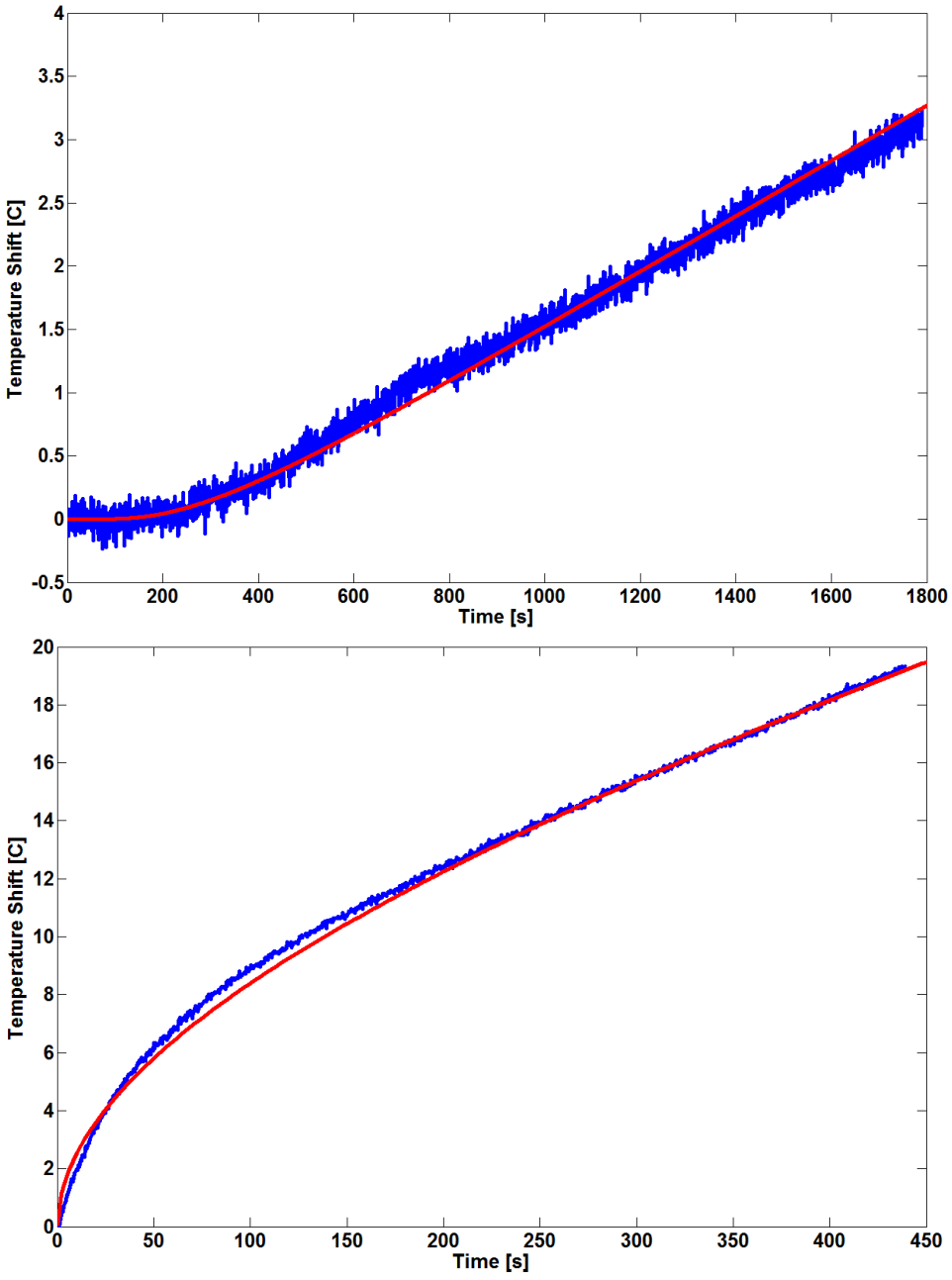

Figure 2-36 Axial (top) and radial (bottom) experimental data with accompanying model for the SAFT VL5Ucell with NCA chemistry; blue line indicates test data, red line is model fit curve

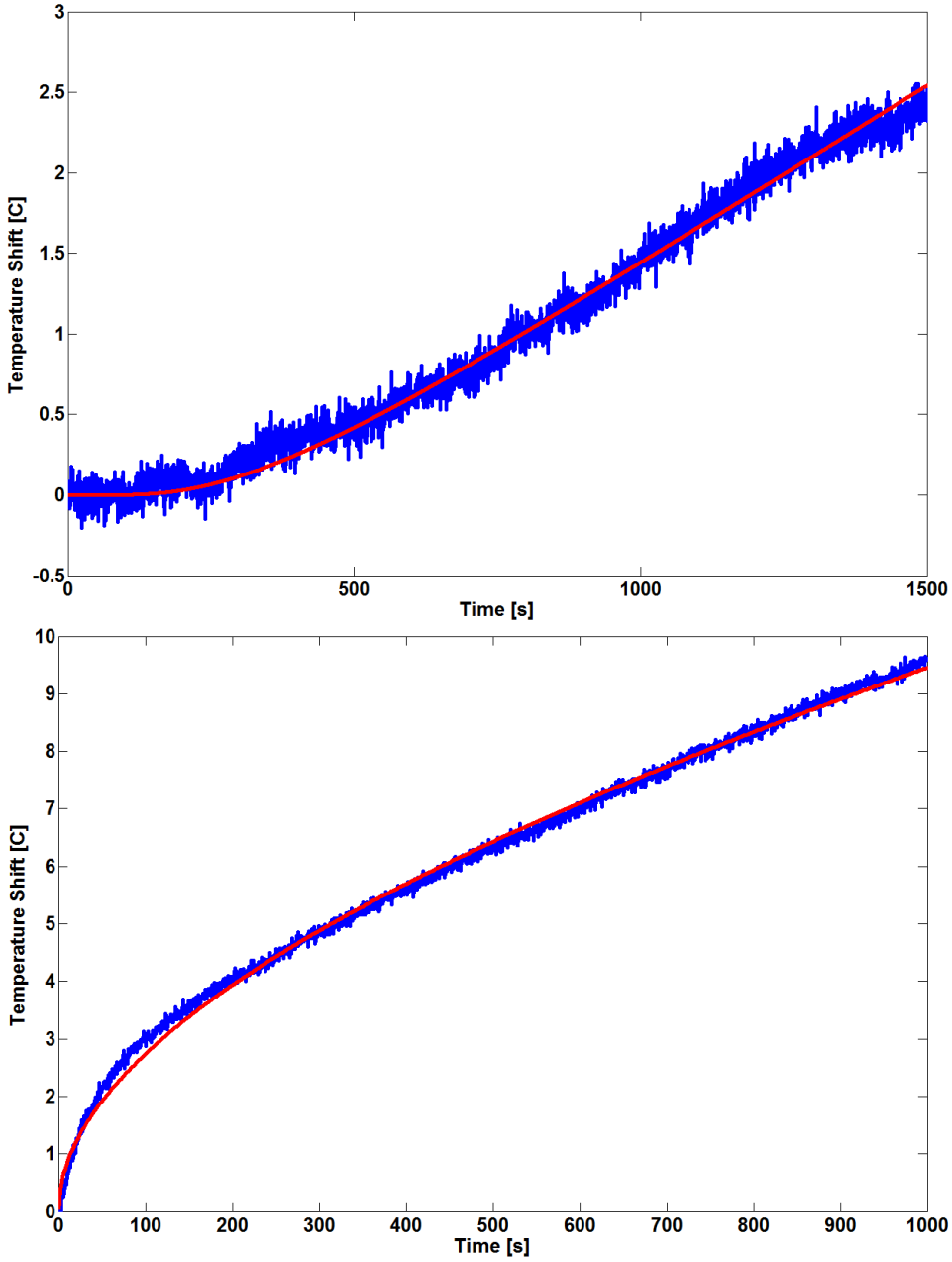

Figure 2-37 Axial (top) and radial (bottom) experimental data with accompanying model for the SAFT VL12V cell with NCA chemistry; blue line indicates test data, red line is model fit curve

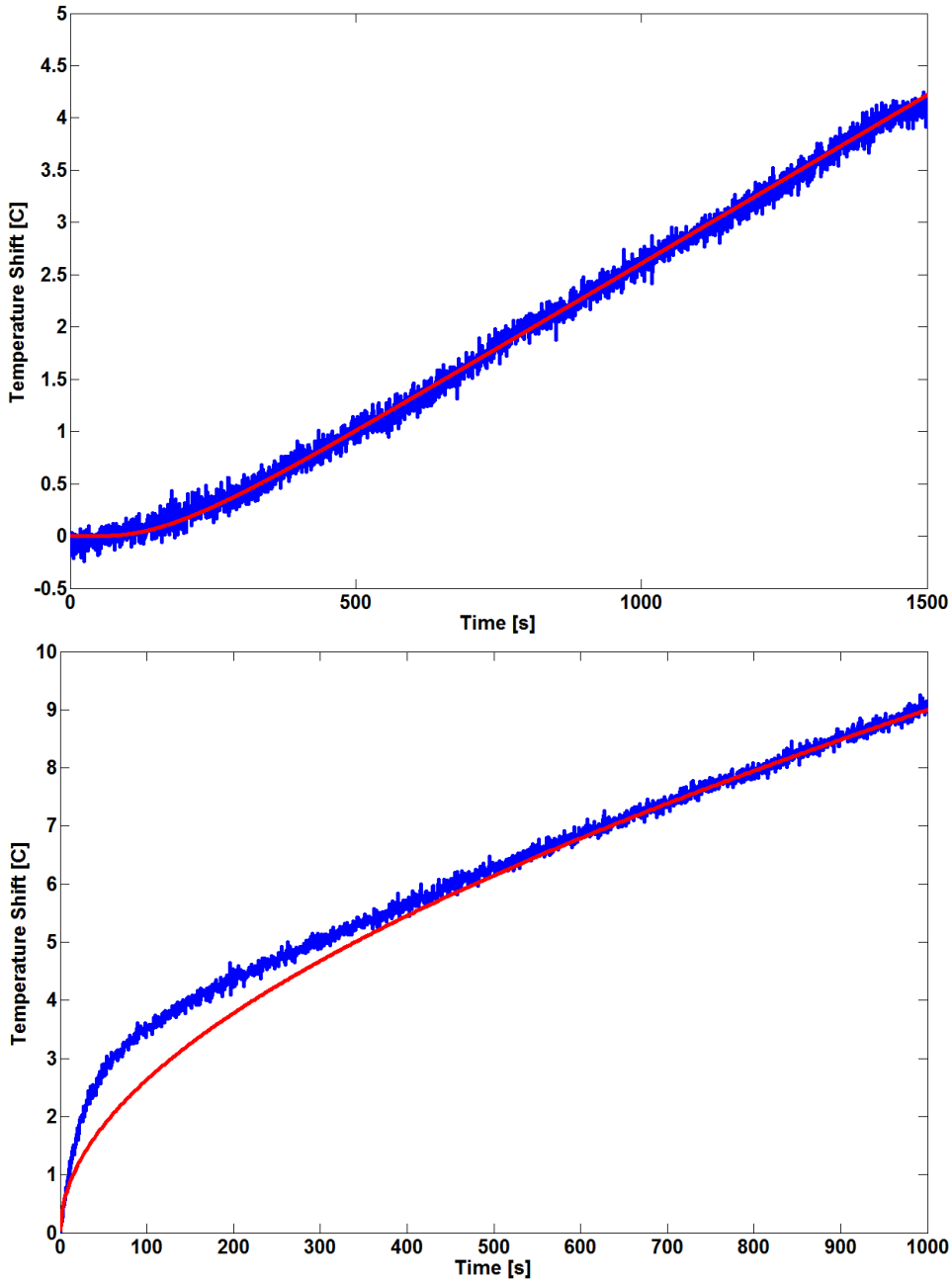

Figure 2-38 Axial (top) and radial (bottom) experimental data with accompanying model for the SAFT VL22V cell with NCA chemistry; blue line indicates test data, red line is model fit curve

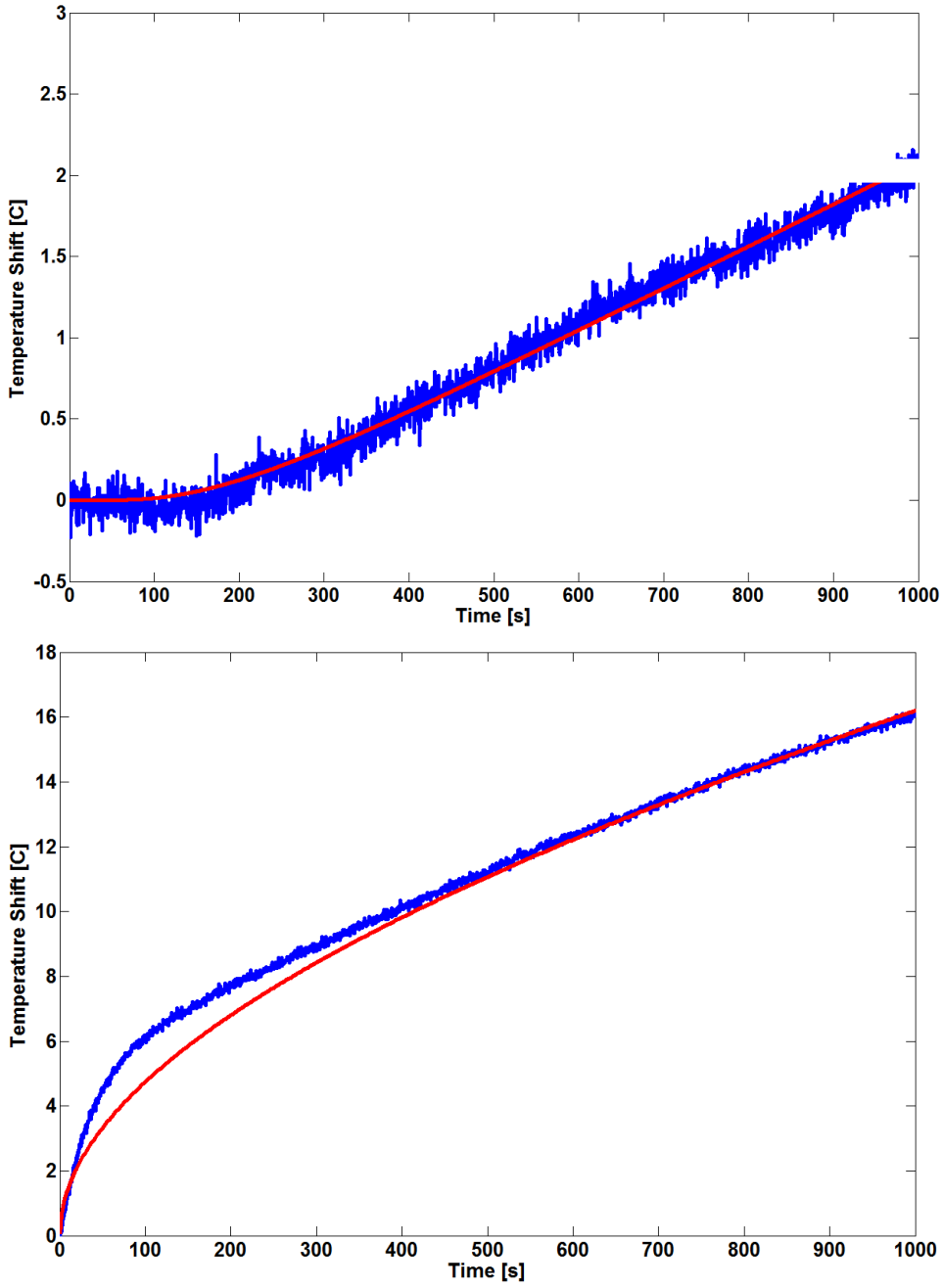

Figure 2-39 Axial (top) and radial (bottom) experimental data with accompanying model for the SAFT 4Ah cell with LTO chemistry; blue line indicates test data, red line is model fit curve

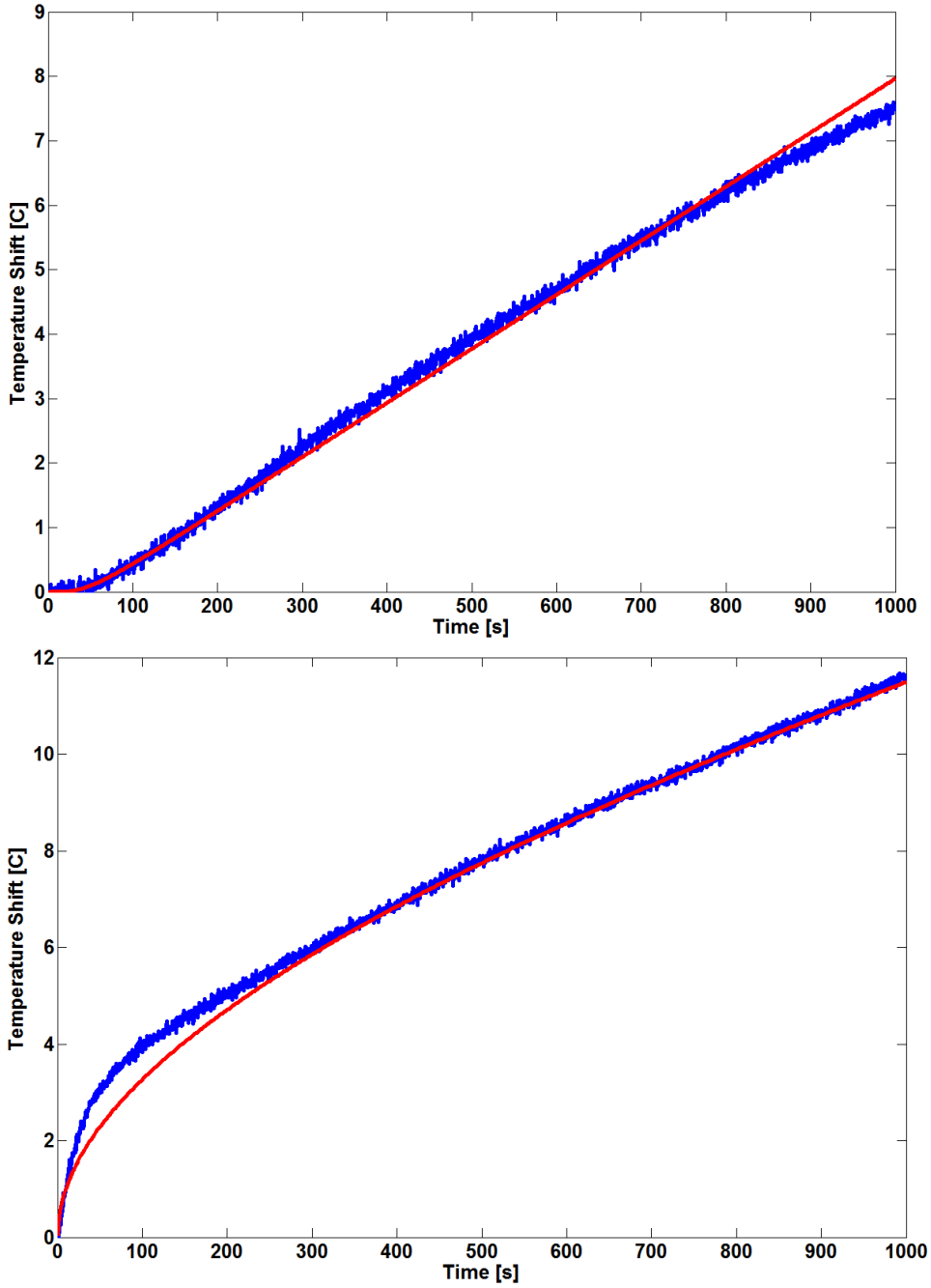

Figure 2-40 Axial (top) and radial (bottom) experimental data with accompanying model for the SAFT 3Ah cell with NCA chemistry; blue line indicates test data, red line is model fit curve

The thermal transport properties of nine batteries are presented in Table 2-5. The degree of anisotropy (k_z/k_r) in the thermal conductivity ranges from a minimum of 54 (GAIA 27Ah cell with NCO chemistry, Figure 2-34) to a maximum of 708 (SAFT 3Ah cell with NCA chemistry, Figure 2-40), with mean and median values of 252 and 201, respectively, from this sample group. Therefore, the anisotropy can vary by more than an order of magnitude, but is typically on the order of 200.

As such, it should be expected that temperature gradients in the radial direction would be 200 times greater than in the axial direction. Given such strong anisotropy, and the fact that the typical operating temperatures of lithium-ion batteries are less than 60°C, one would not expect to see much more than a degree of variation along the axis of the cell under most scenarios.

Table 2-5 Measured thermophysical properties of various shaped cells

Battery Manufacturer, Name, Chemistry	Radius (m)	Height (m)	k_r ($Wm^{-1}K^{-1}$)	k_z ($Wm^{-1}K^{-1}$)	C_p ($J\,kg^{-1}K^{-1}$)
SAFT, VL34, NCA	.027	.02	0.25	47	1300
SAFT, VL30PFE, LFP	.027	.20	0.22	35	1600
GAIA, 27Ah, NCO	.030	.13	0.50	27	1300
GAIA, 18Ah, LFP	.030	.13	0.09	57	3250
SAFT, VL5U, NCA	.017	.15	0.25	55	1550
SAFT, VL22V, NCA	.027	.18	0.16	85	1900
SAFT, VL12V, NCA	.023	.15	0.18	40	1450
SAFT, 4Ah, LTO	.017	.09	0.08	25	2250
SAFT, 3Ah, NCA	.017	.09	0.12	85	1600

Results indicate high thermal anisotropy in each cell once again. Axial thermal conductivities ranged from 25-85 W/m-K, while radial thermal conductivities spanned 0.08-0.50 W/m-K. At minimum, the axial-to-radial thermal transport anisotropy ratio ranged from 50 to 700.

This work highlights the significant differences from the various lithium-ion batteries available today. Knowledge of the highly anisotropic thermal transport properties of cylindrical batteries allows battery power system designs to design more efficient thermal management mechanisms and avoid operating the batteries in a hazardous manner.

State of charged and aging dependence of k, C_p

It is very important to understand the thermal properties of a battery when contemplating how to integrate it into a system, particularly for applications which are operated at extremely high rates. Very little thermal transport data has been published for lithium-ion batteries, specifically as related to how these properties change with respect to state of charge and aging. Experiments have been carried out to measure the change in thermal conductivity and specific heat of cylindrical 26650 lithium-ion cells as the cells age and with respect to state of charge.

Experiments

For these tests four new 26650 cells were tested. Cells were to be artificially aged and thermally characterized through a number of different criteria and compared. In order to accelerate aging for experimental purposes, the cells were repeatedly stored for one week at 70^{o}C until 20% capacity fade was achieved. Two of the four cells were maintained at 50% SOC while stored at 70^{o}C in the temperature chamber while the other two were maintained at 100% SOC. Previous experiments have shown that one week of storage at 70^{o}C induces ~8% capacity fade in a 26650 cell. This leads to an expected end-of-life after 3 weeks of storage. After every one week storage period, the cells are characterized electrically and thermally. Electrochemical Impedance Spectroscopy (EIS) measurements were made to track impedance changes as a function of capacity fade. Potentiostatic EIS is the process of perturbing the cell at its open circuit potential (OCP) with a small amplitude sinusoid at varying frequencies while measuring the resulting current. Analysis of the voltage and current allows the impedance of the cell to be measured. Electrically the cells are cycled each week at ½C and 1C rates. Capacity

measurements are made at each rate. EIS measurements are made at 0%, 50%, and 100% SOC. Thermally the cell's axial and radial thermal conductivities as well as the specific heat are measured each week. Each measurement is made at 0%, 50% and 100% SOC. SOC dependent tests were always carried out following a top off charge and 1C controlled discharge so that exact SOC is known as the cells age.

Results and Discussion

Verification of aging is shown in the clear trend that charge transfer resistance grows as the cell is aged. The increase in the SEI layer is indicative of the decomposition of the electrolyte, and possible damage to the anode electrode. A distinct increase in the Ohmic resistance is indicated by the impedance spectra's shift to the right on the x-axis, Figure 2-41 (a).

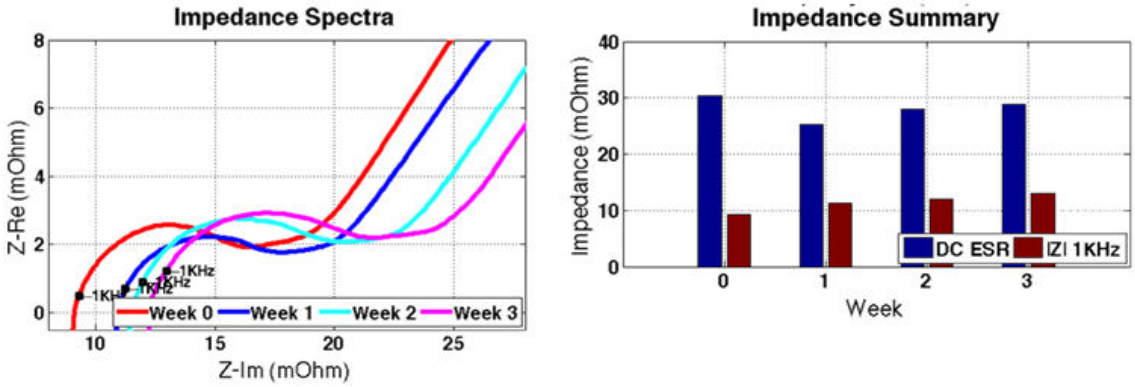

Figure 2-41 Impedance shifting during aging

The red bars of the 1 kHz ESR shows, Figure 2-41 (b), a steady linear increasing trend. The 1 kHz internal ESR grows by 40% relatively consistently after 3 weeks of storage. Thermal data collected over three weeks hint that axial thermal conductivity and specific heat, Figure 2-42, which radial thermal conductivity, Figure 2-43, decreases as time progresses. Ultimately it was determined that the results were inconclusive and follow previous research that state of charge and aging has negligible impact in these thermophysical properties.

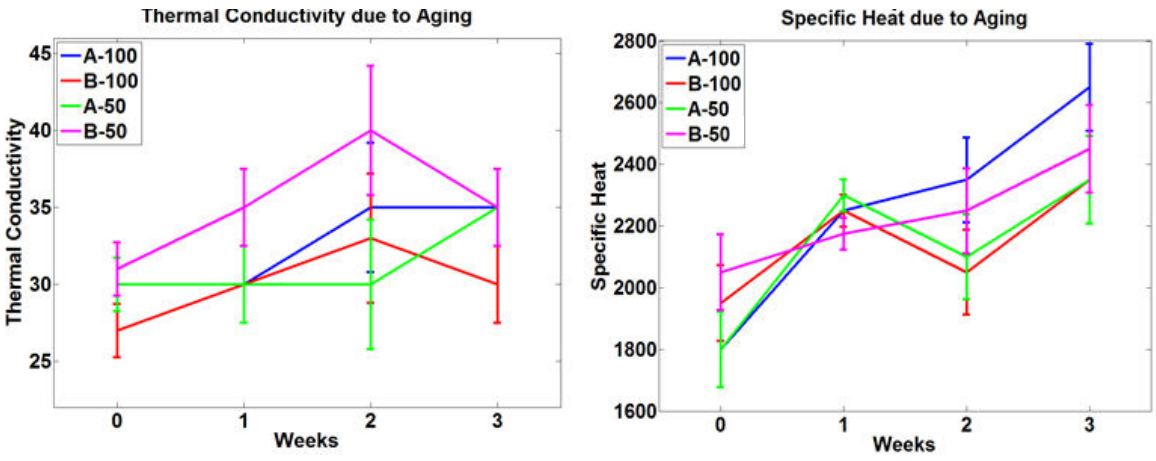

Figure 2-42 Thermophysical properties in axial direction over aging, the numbers indicated in the legend refer to the state of charge (SOC) at which each cell was stored during aging at 70˚F

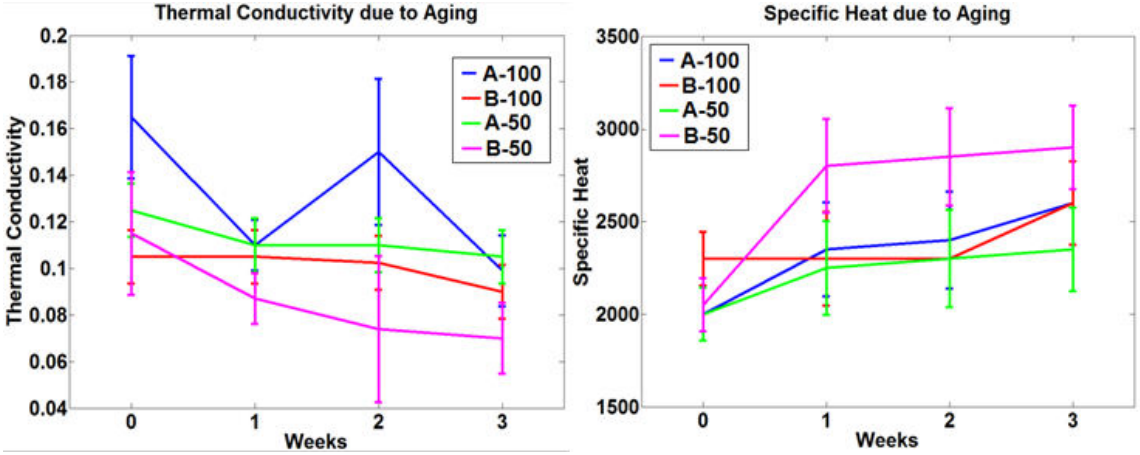

Figure 2-43 Thermophysical properties in radial direction over aging, the numbers indicated in the legend refer to the state of charge (SOC) at which each cell was stored during aging at 70˚F

Measurements indicate the potential for trends, however given the minimal amount of change, the results suggest there is little change to the thermal properties as the age of the cells increases and SOC decreases.

Chapter 3

Heat Generation Measurements in Thermal Test Cells

This section describes an alternative to calorimetry-based methods for measurement of heat generation rate in a heated cylinder, which represents a first step towards the measurement of heat generation rate in a Li-ion cell during operation. This method is based on measurement of heat flux at the outer surface of the cell and comparison with the expected transient thermal characteristics of the cylinder. A thermal test cell of the same dimensions as a 26650 Li-ion cell is used in these experiments. The test cell is capable of precisely controlled heat generation rate. It is shown that the method can measure heat generation rate with very low error, even in transient conditions when the heat generation does not last long, as is typical for high C-rate processes. The next section describes the theory underlying the heat flux measurement method. Experimental setup, comparison with of the model with experimental data, and other results are described in subsequent sections.

Analytical Model

The proposed method for measurement of heat generation rate is based on measurement of outgoing heat flux at the outer surface of the body of interest. Figure 3-1 shows a schematic of a heat-generating cylindrical cell with a heat flux sensor attached on the outer radial surface.

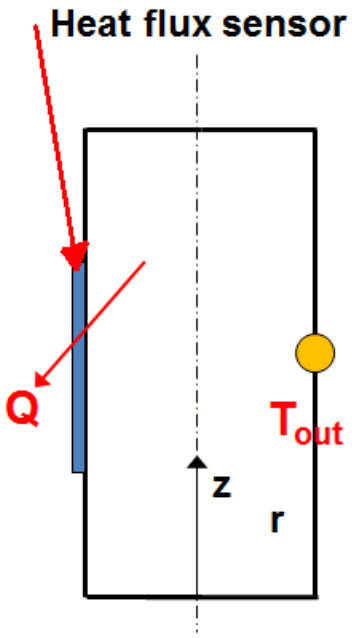

Figure 3-1 Heat flux sensor schematic

Starting at t=0, the cell generates a uniform volumetric heat generation Q''' which is to be measured. As a result of the volumetric heating, the heat flux sensor measures an outward heat flux $q''_{meas}(t)$ that increases with time and eventually reaches a steady state value, $q''_{meas,SS}$. At steady state, since the cylinder temperature does not increase with time, all heat generated inside the cell is dissipated through the outer surface. As a result, a measurement of the heat flux sensor at steady state can be used to determine the internal heat generation rate.

$$Q''' = q''_{meas,SS} \times \frac{A}{V} \quad (15)$$

where A and V are the cell outer surface area and volume respectively.

If the cell has been provided sufficient time to reach thermal steady state, the measured heat flux at steady state can be used in equation (15) to determine the heat generation rate. However, in many cases, the operation of a Li-ion cell may not reach thermal steady state. For example, a Li-ion cell discharging at a high C-rate, say 10C, will undergo complete discharge

within a few minutes. In such a case, it is important to be able to measure the heat generation rate using the heat flux data available for only a limited time, which may be much lower than the time needed to reach steady state. To enable such a measurement, a transient analytical model is developed to model the measured heat flux as a function of time. Assuming that the Biot number is small, the cell can be modeled as a lumped thermal mass, and the temperature of the cell can be written as [Incropera *et al*., 2002]

$$T_{cell}(t) = T_{cell,SS} \cdot \left(1 - \exp\left(-\frac{t}{\tau}\right)\right) \quad (16)$$

where τ is the thermal time constant.

As a result, the heat flux through the outer surface of the cell is given as a function of time by

$$q''(t) = q''_{SS} \cdot \exp\left(-\frac{t}{\tau}\right) \quad (17)$$

Equation (17) shows that q''_{SS} can be determined even if the cell does not actually reach thermal steady state. Equation (17) has two unknown parameters – q''_{SS} and τ. The thermal time constant τ is in general difficult to determine from theoretical calculations, since it involves the convective heat transfer coefficient to the ambient medium, which is not easy to measure precisely. However, data from low power experiments where q''_{SS} is known experimentally can be used to determine τ. This can be done by carrying out a least squares filling of the data with equation (17) and determining the value of τ that results in least error. Once τ is determined from a low power experiment, q''_{SS} for any experiment under the same conditions can be determined by least squares fit of the data with equation (17). This can be done even if thermal steady state is not actually reached, since τ is known, and equation (17) has only one unknown parameter q''_{SS} to

be determined from least squares fitting. Once q''_{SS} is determined, the heat generation rate can be obtained from equation (15).

A conceptually similar approach involves the time derivative of the measured heat flux variation with time. Differentiating equation (17) and evaluating at t=0 yields

$$\left.\frac{dq''}{dt}\right|_{t=0} = \frac{q''_{SS}}{\tau} \quad (18)$$

Combining equations (18) and (15) results in

$$Q''' = \tau \cdot \frac{A}{V} \cdot \left.\frac{dq''}{dt}\right|_{t=0} \quad (19)$$

Equation (19) shows that once the thermal time constant is known, the heat generation rate can be easily determined from the initial slope of the measured heat flux data, even if the cylinder does not actually reach thermal steady state. Equation (19) eliminates the need for least squares fitting by using the initial slope of the heat flux data. However, since it is often difficult to accurately determine the slope of experimental data at a specific time, least squares fitting may still be advantageous.

Equations (17) and (18) provide the theoretical basis for measuring heat generation rates in a body even if the heat generation occurs for a short time. The next section discusses experiments to validate this model.

Experiments

A thermal test cell capable of internal heat generation is fabricated. The test cell has the same dimensions as a 26650 Li-ion cell. Figure 3-2 shows and image of the actual test cell respectively. An empty metal casing of 26mm diameter and 65mm height is used as the outer shell. Inside the casing, a 0.001in thick stainless steel foil is helically wound to provide a means for heat generation through Joule heating. Stainless steel is used because of its relatively high resistivity of $\rho=6.9\text{x}10^{-7}$ Ω-m among commonly available materials.

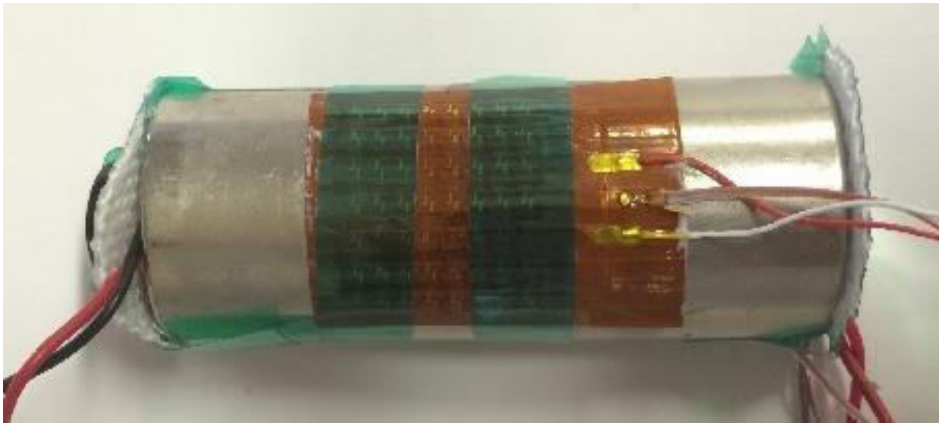

Figure 3-2 Thermal test cell with heat flux sensor attached

A plastic separator is used between the stainless steel turns to allow for multiple windings within the test cell thereby increasing the effective length, and hence electrical resistance of the heating coil. Following the insertion of the heating coil, the cell is filled up with non-conductive epoxy. The two ends of the heater coil are attached to the two electrodes at both axial ends of the test cell, after which the cell is hermetically sealed using a casing cap. The electrical resistance of the test cell is measured to be 0.80 Ω, which is found to be nearly constant in the temperature range of interest. As a result, the thermal test cell is capable of generating a well-known heat generation rate that can be precisely controlled by regulating the electric current passing through the test cell. Due to the square dependence of heat generation on electric current, a large range of heat generation rate can be dissipated in the cell within a narrow range of current.

The test cell is wired with two electrical connections at each axial end, one for supplying electrical current, and another for voltage measurement. Tests were carried out at 2 Hz. Since the heater resistance is very low and comparable to the small diameter of the lead wires, this configuration allows precise power measurement. The axial ends are covered with electrically insulating tape, followed by aluminized glass fiber woven self-adhesive thermal insulation tape. Heat lost through the outer radial surface is measured by an Omega HFS-4 heat flux sensor attached to the outer radial surface. The heat flux sensor is attached to the test cell using

Omegatherm 201 high temperature high thermal conductivity silicone thermal paste. Thin strips of thermal tape are also used to secure the heat flux sensor on the curved surface of the cell, and ensure uniform surface contact. The experiment is conducted underneath a large plastic dome to maintain consistent ambient conditions (within 0.1 C) over several experiments.

A schematic of the test and data acquisition setup is shown in Figure 3-3. A Keithley 2401 sourcemeter is used to supply heating current and a Keithley 2100 multimeter is used for voltage measurements.

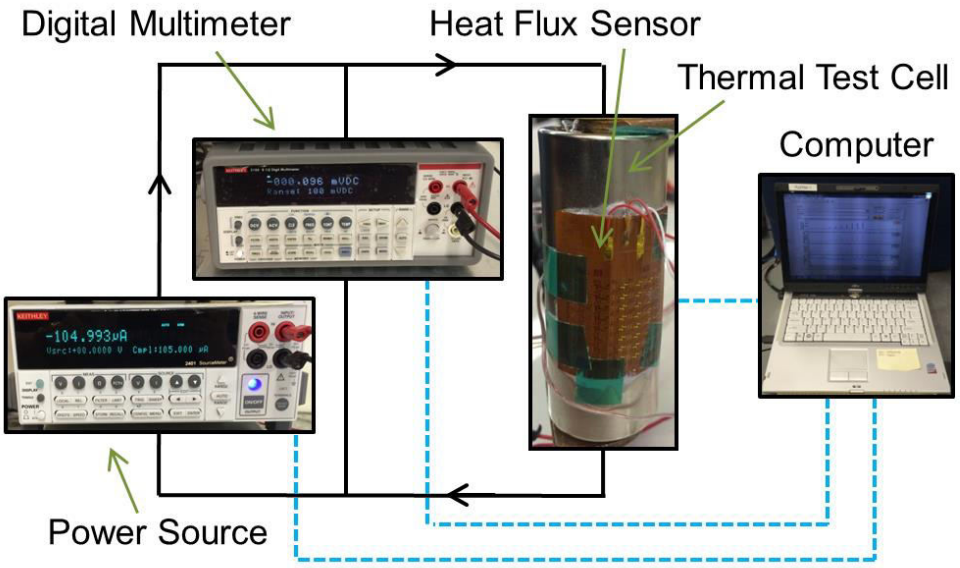

Figure 3-3 Thermal test cell experimental setup

The heat flux sensor outputs a voltage that is proportional to the heat flux passing through the sensor. As a result, heat flux exiting the test cell can be determined by multiplying the measured sensor voltage by a calibration constant. Heat flux sensor output is acquired through a National Instruments NI-9213 16-channel thermocouple input module inside a NI cDAQ 9171 single slot USB chassis. All hardware is controlled and monitored by a LabVIEW code. In each experiment, electric current is sourced to the test cell for a fixed time period. It is found that in

these experimental conditions, steady state is reached in a few hours. The test cell is allowed to cool down to ambient temperature over several hours between experiments.

Analytical Model Validation

Figure 3-4 compares measured heat flux as a function of time with finite element simulation results. Heating current is supplied to the test cell to produce 0.42W heat generation within the cell. Total heat rate exiting the test cell based on measurement from the heat flux sensor is plotted as a function of time. Results from a finite-element simulation are also plotted for comparison. These simulations are carried out in ANSYS CFX based on the geometry of the test cell. The desired volumetric heating is modeled within the cell volume. Grid refinement is carried out to ensure grid-independence of simulation results. The heat flux at the outer surface predicted by the simulations is integrated over the cell surface area to provide heat rate exiting the cell as a function of time. Figure 3-4 shows that there is excellent agreement between experimental measurements and simulation results.

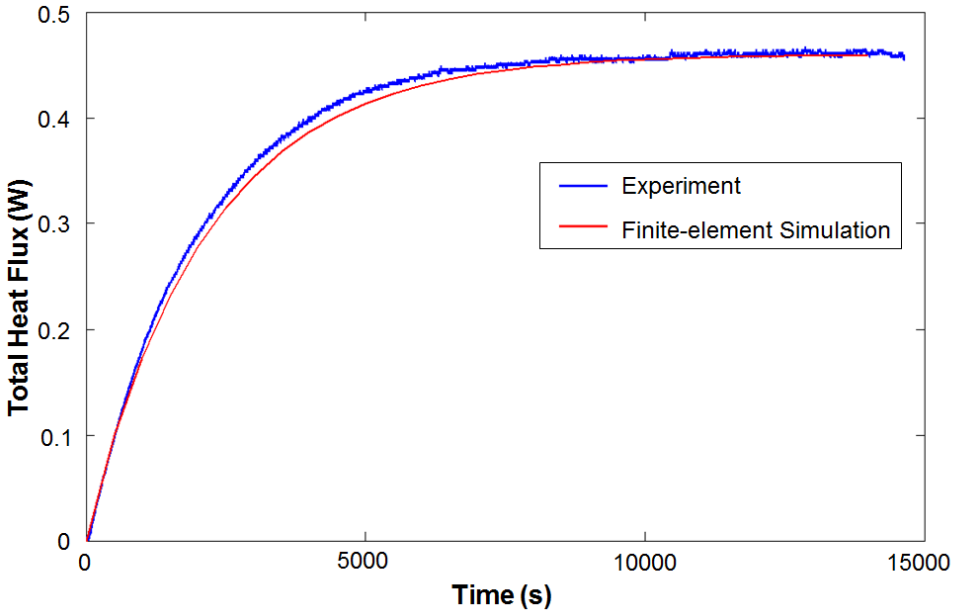

Figure 3-4 ANSYS simulation compared to experimental data

Results and Discussion

Figure 3-5 plots the measured heat flux as a function of time for five different heating powers. Experimental data is shown in solid line while the corresponding analytical model is dashed. Heat flux variation predicted by the analytical model (equation (17)) is also plotted for each power. Powers shown are 0.40 W, 0.46W, 0.59W, 0.67W, 0.76W. There is excellent agreement between experimental measurements and analytical model in each case. The initial rate of increase and the steady-state value are both in excellent agreement with the analytical model. Initially, the heat flux increases rapidly since the cell is far from steady state. Eventually, as steady state is reached, the heat flux measurement stabilizes to a steady-state value. Time required to reach thermal steady state is the same for each power. This is expected since ambient conditions are identical in these experiments.

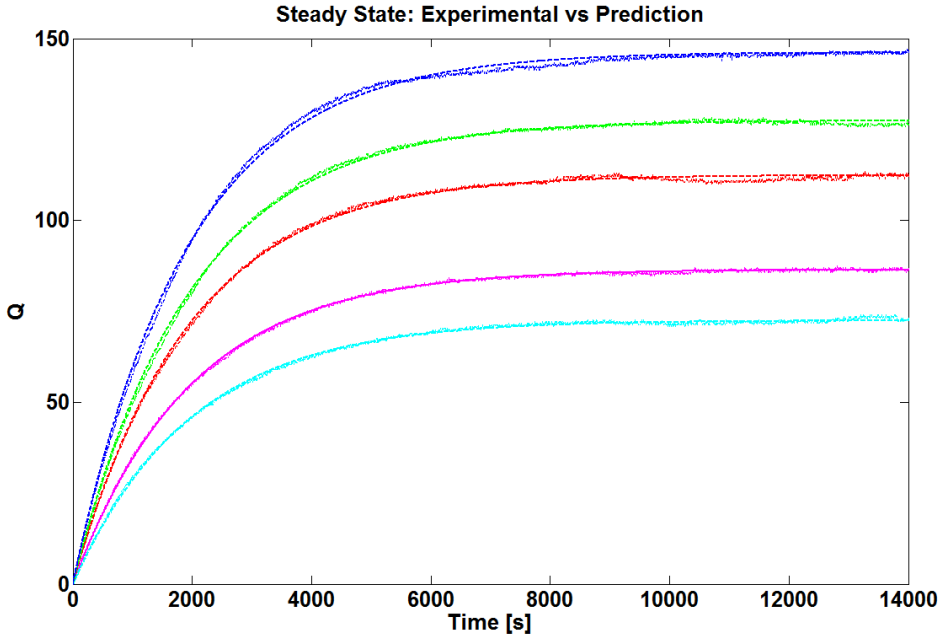

Figure 3-5 Measured heat flux compared to model prediction

Based on the measured steady-state heat flux q''_{SS}, the total heat generation rate in the cell is computed and compared against the known heat generation rate based on the measured

current and voltage across the cell. The measured and actual heat generation rates are plotted in Figure 3-6. All data lie close to the ideal 45° line, with a maximum error of 3.9%. This demonstrates that the measured steady-state heat flux from the heat flux sensor accurately predicts the heat generation rate. These measurements are independent of the thermal ambient conditions and do not require information about thermal properties of the cell or the convective heat transfer coefficient around the cell, unlike a finite-element simulation.

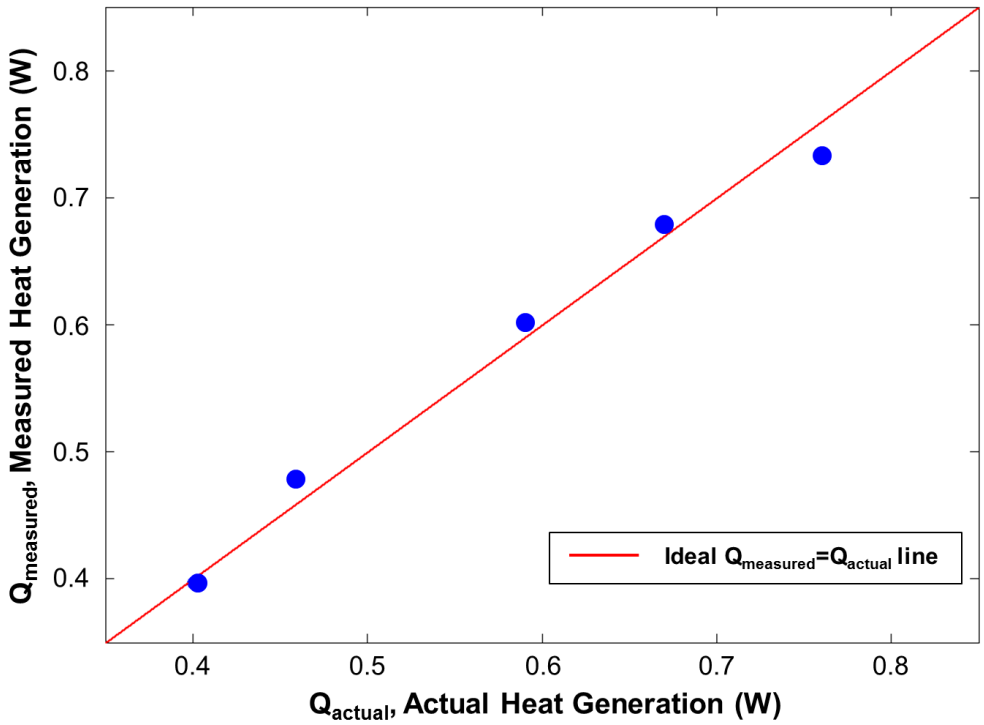

Figure 3-6 Ideal compared to measured heat generation at steady state

While the measurements discussed in Figure 3-5 and Figure 3-6 reached a steady-state, in several cases, there may not be sufficient time available for steady-state to be reached. High-rate charging and discharging of Li-ion cells is complete much before thermal steady state is reached. For example, a 10C discharge completes in only 6 minutes. It is important to be able to predict the heat generation rate even in the absence of steady-state heat flux data – particularly

the value of q''_{SS} – that was used in Figure 3-6**.** In order to do this, heat flux data measured at each power is truncated at different time lengths in order to have data for only a short time available, starting at t=0. This represents a set of experiments where heat generation occurs only for a short time. Heat flux data available only within this short time must be used to measure heat generation rate. These truncated data are compared with the analytical model (equation (17)), assuming that the thermal time constant τ remains the same as previous experiments where thermal steady state was reached. This is a reasonable assumption, since τ depends on surface area, volume and heat capacity of the cell, and the convective heat transfer coefficient, each of which remain the same between experiments. Thus, the only unknown in equation (17) is q''_{SS} . A least squares fit of available data with equation (17) is used to predict the steady-state heat flux. Figure 3-7 plots the predicted heat flux as a function of time based on experimental data for 0.46W power truncated at 250, 500, 750, 1000 and 1500 seconds.

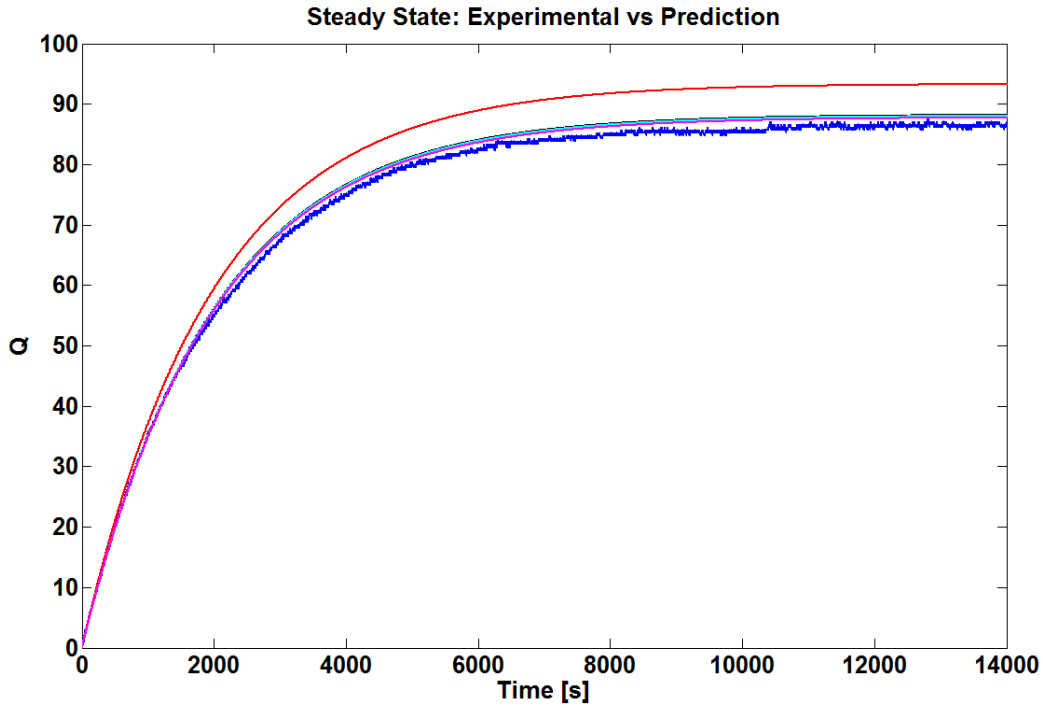

Figure 3-7 Experimental data for 0.46W compared to model analysis at five different duration lengths

The experimentally measured heat flux variation as a function time up to steady state is also plotted. In each case with limited experimental data, the model predicts the steady-state heat flux with reasonable accuracy. The accuracy improves as the duration of experiment increases. With as low as 250s of data, the error between actual and measured heat generation rate is below 7%. With 500s or more of data, the error reduces even more. This shows that the model presented can be used to accurately predict the heat generation rate even for short duration heat generation.

Figure 3-8 plots the measured heat generation rate in W with the actual heat generation rate for a 500s experiment. Similar to Figure 3-6, there is good agreement between the two, and the maximum error among the five power values investigated is 3.9%.

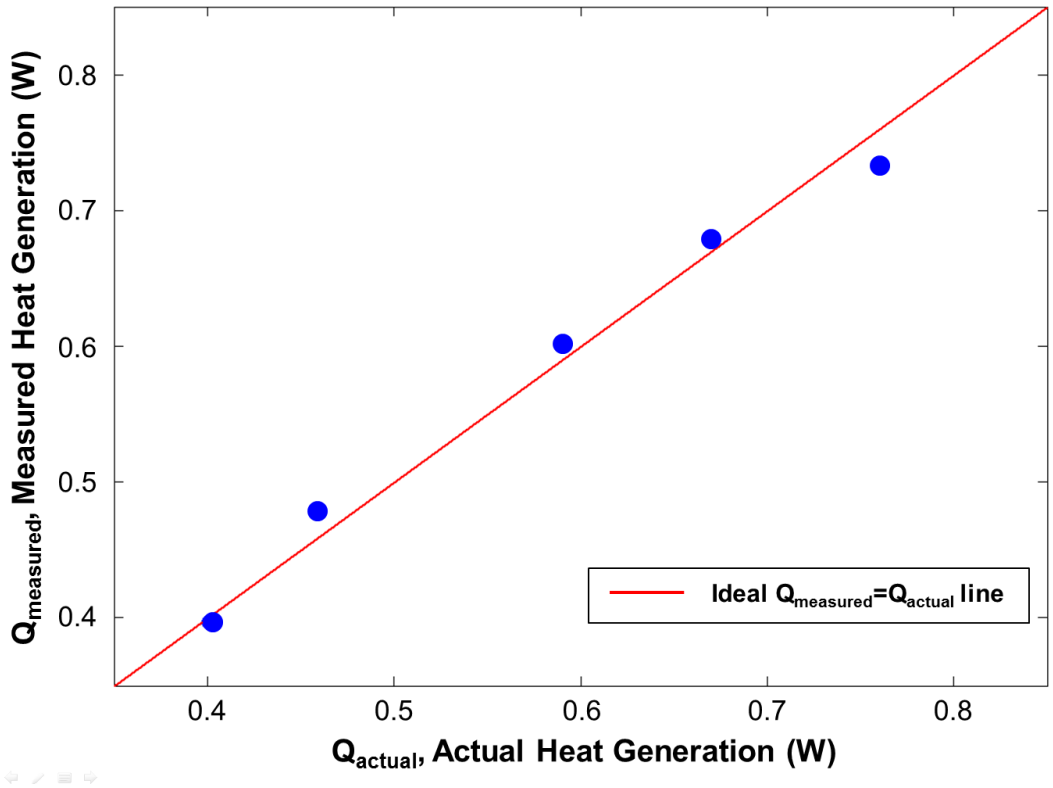

Figure 3-8 Ideal compared to measured heat generation with 500 seconds of data

Figure 3-9 plots the percent error in measurement of five different heat generation rates as a function of the time duration of the experiment. In general, the error reduces as the time duration increases. Even with only 500s of data, which roughly corresponds to 7C discharge rate for a Li-ion cell, the maximum error among all five heat generation rates investigated here is less than 4%. Thus, this method is capable of measurement of heat generation rate even for short time duration discharges typical of large C-rate processes.

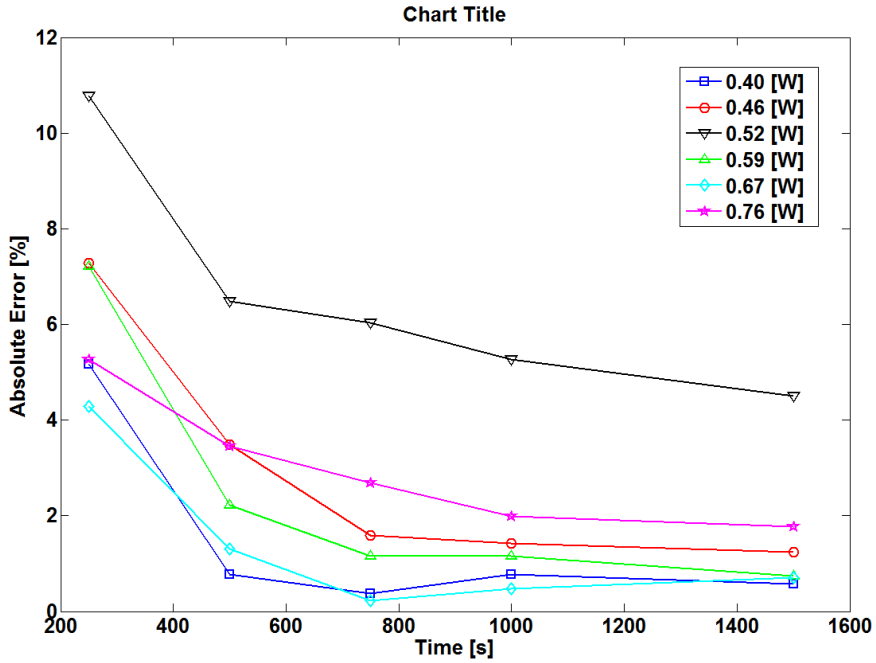

Figure 3-9 Percent error for six powers as a function of the time duration of the experiment

Conclusions

Presented a method for measuring heat generation rate in a heat generating body using heat flux measurement on the outside surface of the body. Even when the duration of heat generation is too short for the body to reach steady state, the method presented here predicts the heat generation rate with excellent accuracy. In general, the longer the time duration of heat generation, the more accurate is the method. Accurate measurement of heat generation rate is expected to aid in better thermal modeling and control of the cell and battery packs.

The methodology presented is relatively simple, requiring only a heat flux sensor. Information about material properties or ambient conditions is not needed, which further adds to the ease and versatility of the method. In the context of Li-ion cells, this method measures heat generation rate with good accuracy even at large C-rates. While the focus on measurement is this work is on heat-generating Li-ion cells, this capability can be easily extended to other engineering problems involving heat generating bodies.

Chapter 4

Heat Generation Measurements in Real Cells

Temperature rise in a Li-ion cell during operation is governed by three phenomena: the rate at which heat is generated within the cell, the rate at which heat conducts within the cell to the outer surface, and the rate at which heat is removed from the cell outer surface to the surroundings. Heat dissipation to the ambient depends on the cell geometry and the cooling system performance. Heat conduction within the cell depends on thermal transport properties of the Li-ion cell, namely thermal conductivity and heat capacity. Previous presented measurements of thermal properties of a Li-ion cell using an adiabatic heating method indicate strong anisotropy in thermal conduction between radial and axial directions, with particularly poor radial thermal conductivity.

In addition to heat conduction within the cell and heat removed at the cell surface, an understanding of internal heat generation rate is also very important for a complete thermal understanding of a cell.

This section reports real-time, *in situ* measurements of heat generation rate during high-rate discharge of a cylindrical Li-ion cell, up to 9.6C. These measurements are purely thermal in nature, utilizing heat flux and temperature sensor measurements in *in situ* settings. Heat stored in the cell and heat lost through the outside surfaces – two independent components of the total heat generated – are accounted for and measured simultaneously. Measurements provide data on heat generation as a function of time during the discharge process. Experiments are carried out with and without active cooling provided by a fan.

Analytical Model

A widely used theoretical model predicts the heat generation rate as follows [Thomas *et al.*, 2003]

$$Q_{theoretical} = I \cdot (U - V) - I \cdot T \frac{\partial U}{\partial T} \quad (20)$$

Where I, V and T are current, voltage and temperature respectively, and U is the open circuit voltage corresponding to the depth of discharge. The first term in equation (20) accounts for heat generation due to voltage overpotential/underpotential (under discharge/charge, respectively), whereas the second term accounts for entropic heat generation. Equation (20) assumes that heat generation due to heats of mixing and heat generation due to side reactions are neglected.

Consider a charge or discharge process for a Li-ion cell, starting at t=0, during which heat is generated. Let Q(t) be the total heat generated, in Joules, up to time t. Revisit the schematic, Figure 4-1 (a), Q(t) is either stored within the cell, $Q_A(t)$ or is lost to the ambient through the outer surface of the cell, $Q_B(t)$.

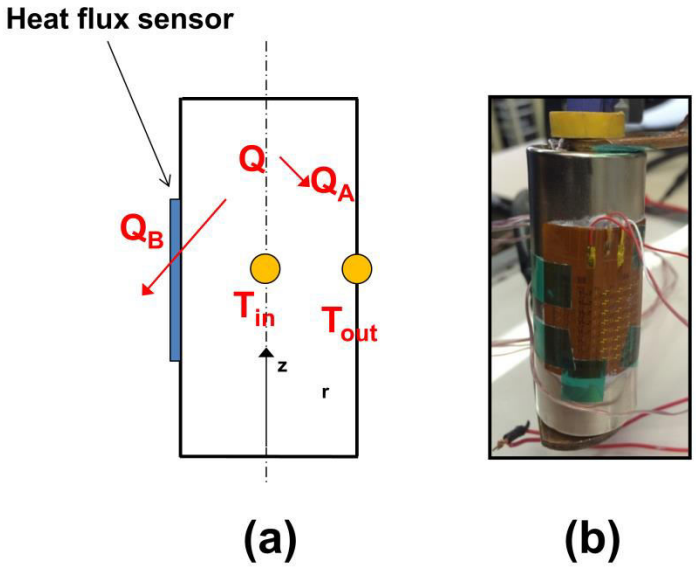

Figure 4-1 (a) Schematic of stored and lost components of total heat generated, (b) Picture showing Li-ion cell under test, including a heat flux sensor

The component $Q_A(t)$ results in temperature rise of the cell, whereas $Q_B(t)$ results in an increase in the heat flux leaving the cell at the outer surface. $Q_A(t)$ is related to the volume-averaged cell temperature rise as follows:

$$Q_A(t) = \rho \forall C_p \Delta T_{volavg}(t) \quad (21)$$

where ρ, C_p, and ∀ are the mass density, heat capacity and total volume of the cell respectively. $\Delta T_{volavg}(t)$ is the volume-averaged cell temperature rise at any time, t. Thus, a measurement of $\Delta T_{volavg}(t)$ can be combined with cell thermal properties to determine $Q_A(t)$.

On the other hand, $Q_B(t)$, the component corresponding to heat lost through the outer surface, can be measured using a heat flux sensor. A heat flux sensor outputs a DC voltage proportional to the heat flux passing normal to the sensor surface at any time. Thus, $Q_B(t)$ is given by

$$Q_B(t) = \int_0^t C \cdot V_{HFS}(\tau) \cdot Ad\tau \quad (22)$$

where $V_{HFS}(\tau)$ is the voltage output of the heat flux sensor at any time τ, C is the calibration constant of the heat flux sensor ($Wm^{-2}V^{-1}$), and A is the cell surface area.

The total heat generated at any time t is then simply given by

$$Q(t) = Q_A(t) + Q_B(t) \quad (23)$$

The instantaneous heat generation *rate*, in Watts, can be determined by differentiating the experimentally measured Q as a function of time.

Equations (21)-(23) represent a purely thermal method to measure heat generation rate in an operating Li-ion cell directly, as opposed to estimating the heat generation rate from cell voltage and current. Measurements of only temperature and heat flux are needed, and no information is needed about the underlying mechanisms responsible for heat generation in the cell.

In general, $\Delta T_{volavg}(t)$ is given by

$$\Delta T_{volavg}(t) = \frac{2}{R^2 H} \int_0^H \int_0^R r \Delta T(r, z, t) dr dz \quad (24)$$

Determination of $\Delta T_{volavg}(t)$ requires measurement of temperature rise throughout the internal volume of the cell, followed by integration according to equation (24). This is clearly not practical. However, it can be shown that within the parameter space encountered in these experiments, the volume-averaged temperature rise in a cylinder can be determined from only two temperature measurements as follows:

$$\Delta T_{volavg}(t) \approx \Delta T_{mean}(t) = \frac{\Delta T_{core}(t) + \Delta T_{out}(t)}{2} \quad (25)$$

where $\Delta T_{core}(t)$ and $\Delta T_{out}(t)$ are the temperature rise at the core of the cell (r=0), and at the outside surface of the cell (r=R) at mid-height respectively.

A further difficulty in the determination of $\Delta T_{volavg}(t)$ lies in the measurement of the core temperature $\Delta T_{core}(t)$. While it may be possible to drill a hole through the top cap of the cell to insert a thermocouple into the cell core [Forgez *et al.*, 2010], this is only practical for controlled laboratory experiments. The drilling process may alter the electrical impedance of the cell and, in many cases, may cause a short circuit and render the cell inoperable. An indirect method for determination of the cell core temperature, without the need for drilling, is utilized in this paper. This method is based on measuring the core and outside temperatures of a drilled cell having the same geometry and thermal properties , undergoing discharge in the same ambient condition as the *undrilled* cell of interest. Following the theory of thermal conduction it can be shown that the core temperature of an undrilled cell, $\Delta T_{core,undrilled}(t)$ is given by

$$\Delta T_{core,undrilled}(t) = \Delta T_{core,drilled}(t) \times \frac{\Delta T_{out,undrilled}(t)}{\Delta T_{out,drilled}(t)} \quad (26)$$

In short, equation (26) states that the ratio of the core and outside temperatures is the same for the drilled and undrilled cells, assuming same geometry, thermal properties, and ambient conditions. Heat generation rates in the two cells do not need to be the same. Equation (26) makes it possible to use a one-time measurement of the core temperature of a drilled cell to non-invasively determine the core temperature of a similar undrilled cell undergoing any discharge process. Once the core temperature is determined, equation (21) and (25) are used to determine the heat stored in the cell. Finally, equation (23) is used to determine heat generated in the cell. This measurement can be carried out at any time during the cell discharge process, and hence can provide heat generated, in Joules, as a function of time. The instantaneous and time-averaged heat generation rates, in Watts, can also be determined by numerical differentiation of the experimental data.

Experiments

A previously unused 2.6 A-hr $LiFePO_4$ 26650 cell is used in the measurements. Prior to heat generation measurements, Electrochemical Impedance Spectroscopy (EIS) of the cell is performed using a Princeton Applied Research PARSTAT 4000 potentiostat, Figure 4-2.

Figure 4-2 Princeton Applied Research PARSTAT 4000 potentiostat

The equivalent series resistance (ESR) of the cell is measured to be 12.0 m-Ω. An EIS measurement prior to heat generation measurements establishes the electrical health of the cell being used in the measurements.

The fully charged cell is connected to a Maccor Series 4000 testing system, Figure 4-3, that incorporates electrical loads and power supplies to charge and discharge the cell at a desired rate.

Figure 4-3 Maccor Series 4000 cycling system

The Maccor system also provides voltage and current measurements. Measurements from T-type thermocouples attached to the cell are monitored to ensure that the cell is uniformly at room temperature prior to any discharge. A maximum operating temperature of 55 °C is implemented during the discharge process for safety.

Figure 4-1 (b) shows the test cell, including a heat flux sensor attached on the outer surface. A HFS-4 heat flux sensor from Omega Engineering is placed in direct contact with the outer surface of the cell using Omegatherm-201 thermal paste, to ensure good thermal contact with the cell, and Kapton polyimide tape, to help secure the sensor to the cell. The heat flux sensor incorporates a dual-layered thermocouple array to output a voltage signal that is proportional to the heat flux passing through the sensor surface. Sensor output is measured using the same National Instruments NI-9213 16-channel thermocouple input module inside a NI cDAQ 9171 single slot USB chassis. A single input channel is configured to log data in the microvolt range. T-type thermocouples are also placed in contact with the outer surface to measure $T_{out}(t)$. Additional channels in the same NI cDAQ 9171 are configured for use with these thermocouples. It is used in conjunction with an NI LabVIEW VI for data acquisition from thermocouples. Temperature and heat flux measurements are recorded every second for the entire discharge duration.

A set of experiments are carried out to evaluate the effect of active cooling on the thermal performance of the cell. In these experiments, air is blown over the outer surface of the cell by a Holmes two-speed personal fan with air speed of 3.6 m/s.

$\Delta T_{core,drilled}(t)$, which is needed to determine $\Delta T_{core,undrilled}(t)$ using equation (25) is measured using a separate, identical 26650 Li-ion cell. A 7/32-in hole is drilled through the cap of this cell. Three T-type thermocouples are aligned vertically and encased in a thin-walled heat shrink tubing. This allows for better placement accuracy and minimizes unwanted shifting during assembly. The tubing carrying the thermocouples is inserted down the spindle gap of the cell. The hole in the cell cap is then back-filled with an OmegaBond two part thermal epoxy. The entire process is carried out within an inert gas glovebox environment. The cell is cured overnight in the glovebox.

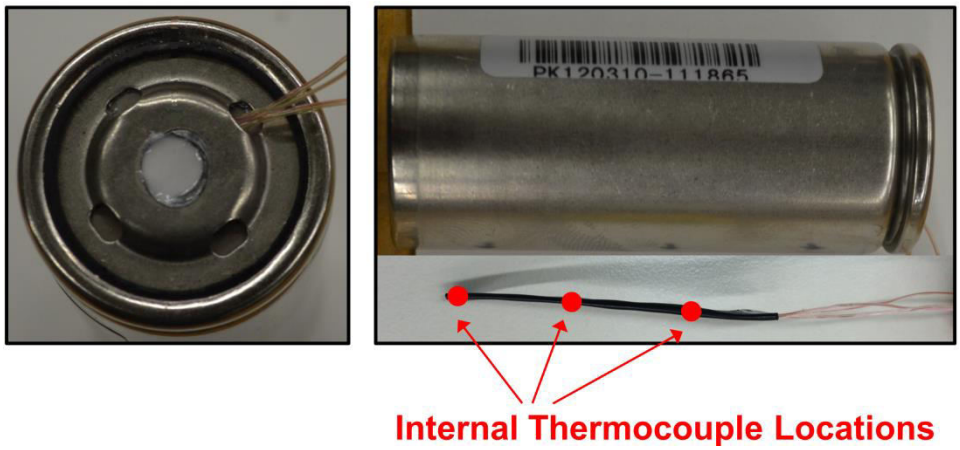

Figure 4-4 Pictures showing top and side views of the drilled Li-ion cell; approximate locations of thermocouples are shown in side view

Figure 4-4 shows images of the thermocouples mounted in the tubing, as well as the drilled hole in the cell. Prior to heat generation measurement, the cell is recharacterized through an EIS measurement. Cell ESR is found to undergo minimal change (12.0 m-Ω to 14.0 m-Ω). This indicates that the cell is still capable of storing charge with negligible change in its electrical characteristics.

The mass density of the test cell is determined separately by measuring its volume using Vernier calipers and its weight using a sensitive scale balance. The value of heat capacity of the cell, to be used in equation (21) is obtained from recently reported measurements [Murashko *et al.*, 2014].

Results and Discussion

Components of Heat Generation

Following EIS characterization, the 26650 Li-ion cell is discharged at six different discharge currents, ranging from 2.6A (1C) to 25A (9.6C). In each case, the heat lost, heat stored and total heat generated are measured as functions of time. Figure 4-5-Figure 4-10 shows a representative plot of these quantities as functions of time during all discharges.

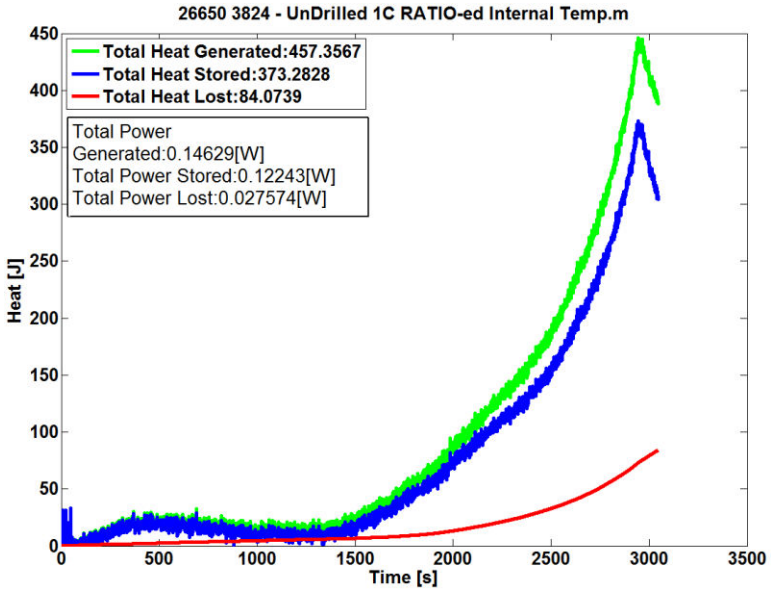

Figure 4-5 Measured heat stored, heat lost and heat generated as functions of time for an uncooled cell at 1C discharge

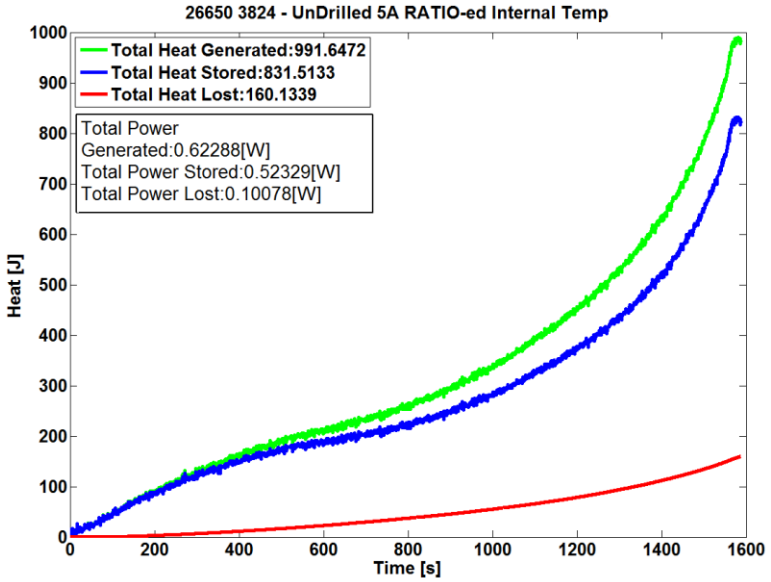

Figure 4-6 Measured heat stored, heat lost and heat generated as functions of time for an uncooled cell at 1.9C discharge

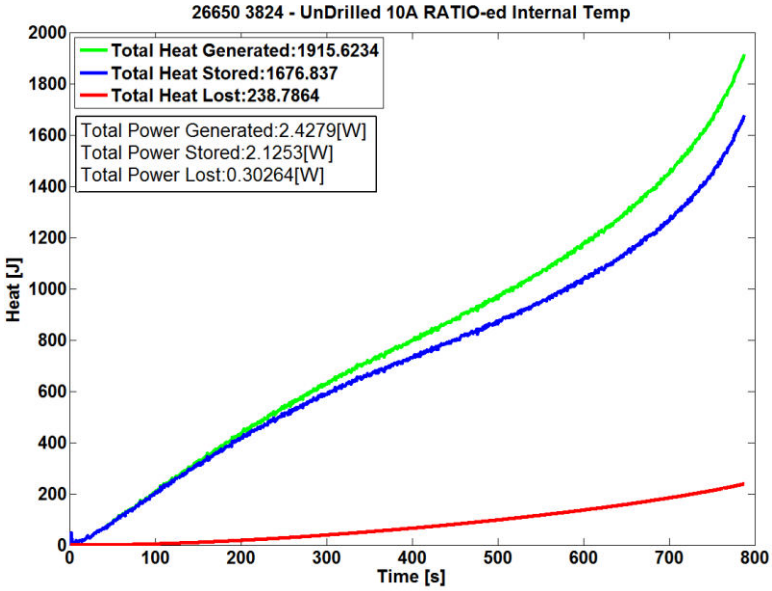

Figure 4-7 Measured heat stored, heat lost and heat generated as functions of time for an uncooled cell at 3.8C discharge

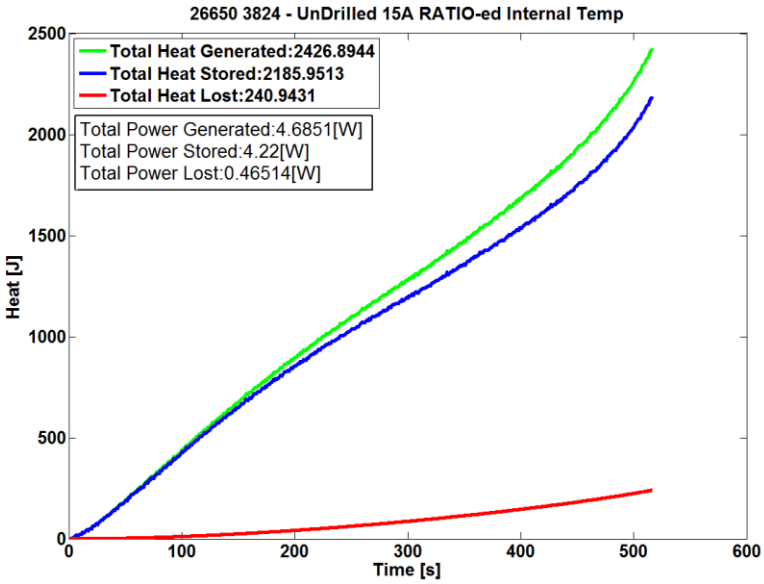

Figure 4-8 Measured heat stored, heat lost and heat generated as functions of time for an uncooled cell at 5.8C discharge

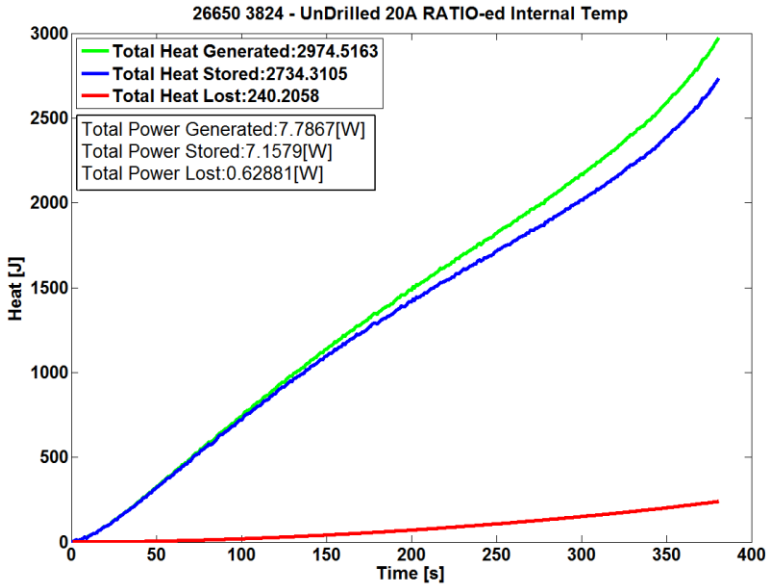

Figure 4-9 Measured heat stored, heat lost and heat generated as functions of time for an uncooled cell at 7.7C discharge

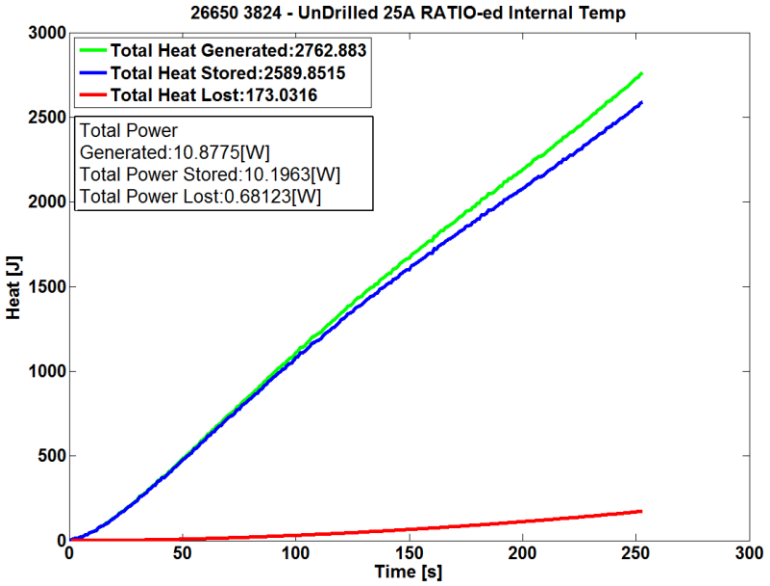

Figure 4-10 Measured heat stored, heat lost and heat generated as functions of time for an uncooled cell at 9.6C discharge

Most of the heat generated in the cell during the discharge process is stored within. This is consistent with the lack of any active cooling of the cell. In all, about 2100 J heat is generated,

which is about 8% of the 26200 J energy converted from chemical to electrical form during the discharge process. Plots similar to Figure 4-8 are obtained for other C-rates.

Heat Generation and Heat Generation Rate as functions of C-rate and SOC

Figure 4-11 plots total heat generated for the entire discharge process as a function of time for six different discharge currents.

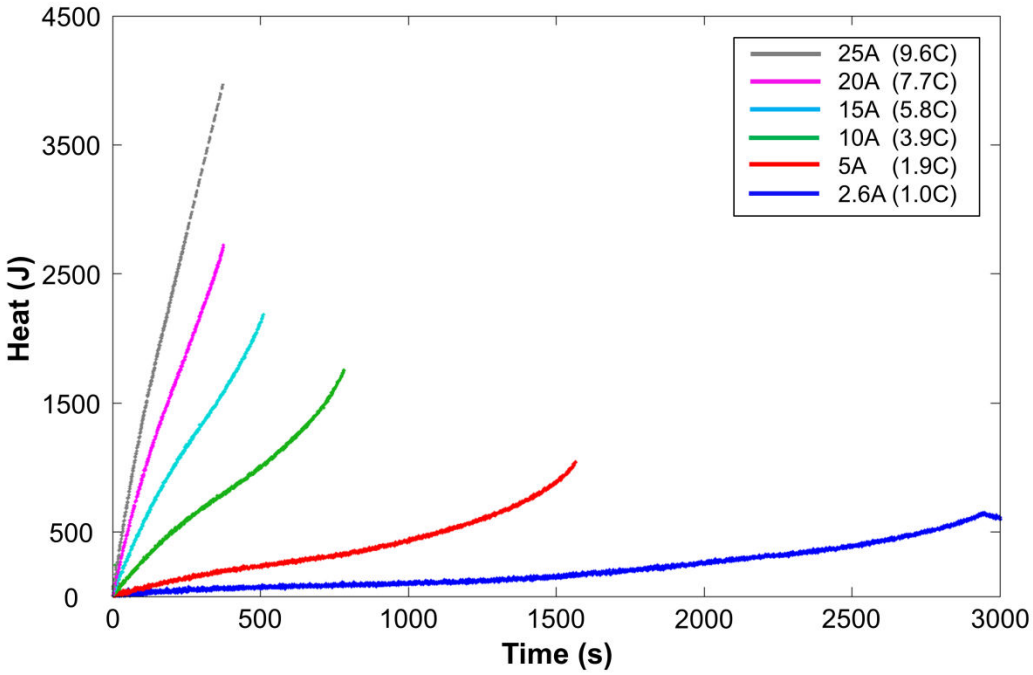

Figure 4-11 Heat generated as a function of time for different C-rates

Heat generation is nearly linear with time for high C-rate cases. In all cases, there appears to be more rapid heat generation towards the end of the discharge process. As expected, Figure 4-11 shows that low C-rate discharge results in significantly lower heat generated over a longer time period. Note that for the 25A discharge case, the cell temperature reached the 55 °C safety limit before completely discharging. As a result, a portion of the 25A curve, shown as a broken line on Figure 4-11 is extrapolated based on actual measurements. As

shown in Figure 4-12, the total heat generated in the entire discharge period increases linearly with C-rate.

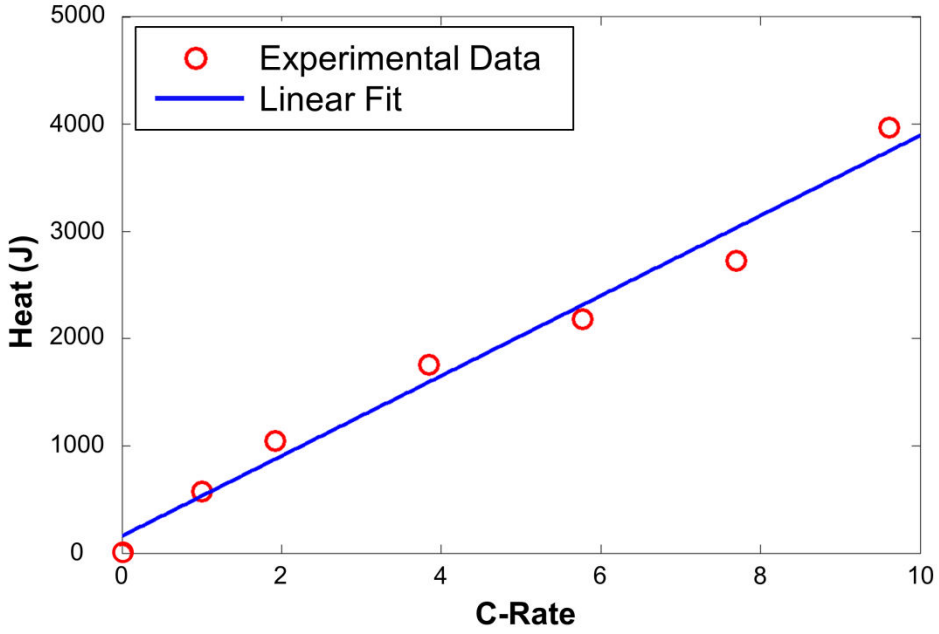

Figure 4-12 Total heat generated during entire discharge process as a function of discharge rate known as C-Rate

From the measurement of total heat generated shown in Figure 4-11, it is possible to determine the instantaneous heat generation rate as a function of time, or SOC. This is plotted in Figure 4-13 (a) for a number of C-rates. In each case, the heat generation rate goes up, then down and then up again during the discharge process. When divided by I^2, the heat generation rate curves collapse into a tight band, shown in Figure 4-13 (b). This shows that the measurement method described here captures the common underlying mechanism for time-varying, current-dependent heat generation rate during discharge at all C-rates. Figure 4-13 shows the capability of measuring the instantaneous heat generation rate as a function of SOC in *in situ* conditions, without the need of a calorimeter.

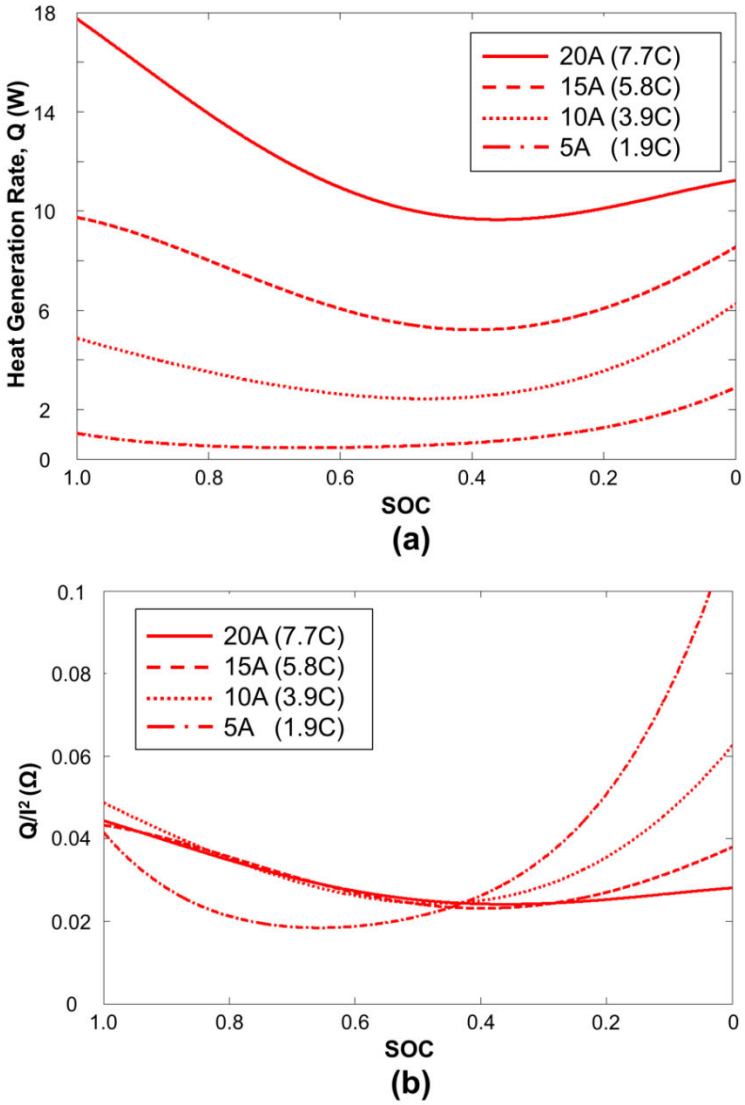

Figure 4-13 (a) Heat generation rate as a function of state of charge, SOC, for different C-rates, (b) Heat generation rate divided by square of the current as a function of SOC for different C-rates

The average heat generation rate over the entire discharge period is computed, and plotted as a function of C-rate in Figure 4-14, which shows strong dependence on C-rate.

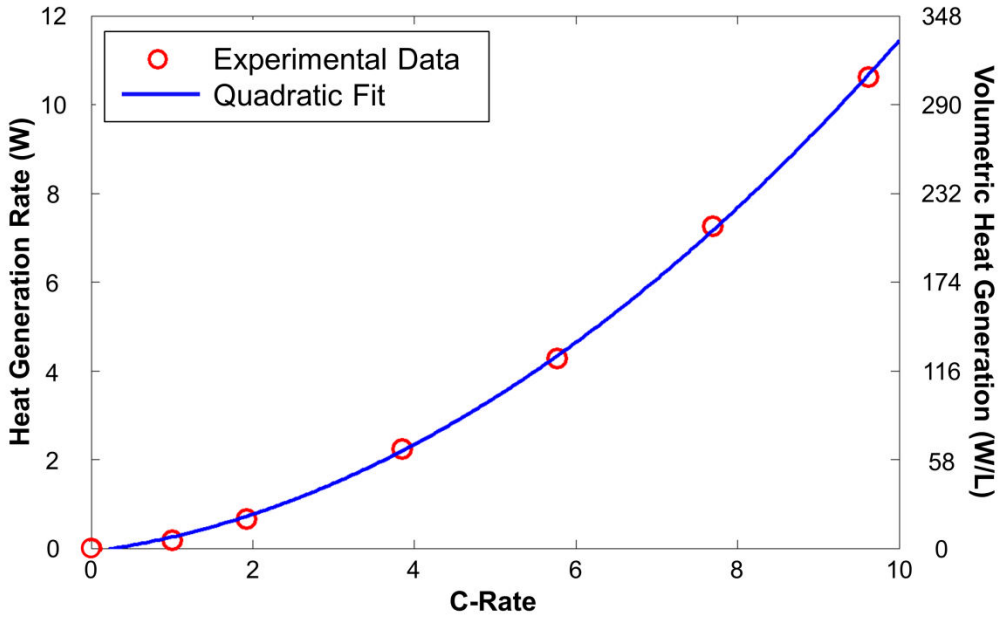

Figure 4-14 Average heat generation rate as a function of C-rate

This data fits well with a quadratic curve, which is expected, based on the I^2 dependence of heat generation mechanisms within the cell. The heat generation rate at 9.6C, the highest C-rate tested in this work is 10.6W for a single 26650 cell. Expressed as volumetric heat generation rate, this corresponds to 307 W/L.

Analytical Model Validation

The commonly used heat generation model for Li-ion cells, given by equation (20) is used to compute the heat generation rate and compare with experimental data. In this model, I and V, the current and voltage across the cell are based on measurements during tests. The open-circuit voltage, U, is determined by plotting the experimentally measured voltage as a function of discharge current at each SOC during the discharge process. This curve is found to be linear for all experiments, and extrapolation to zero current results in determination of U. The volume averaged cell temperature defined in equation (24) is determined using equation (25) for use in the entropic heating term in equation (20). Finally, the dU/dT term in equation (20) is obtained

from measuring open-circuit voltage response to step-changes in temperature at various SOC similar to the procedures described by Forgez, *et al.* [Bandhauer *et al.*, 2011].

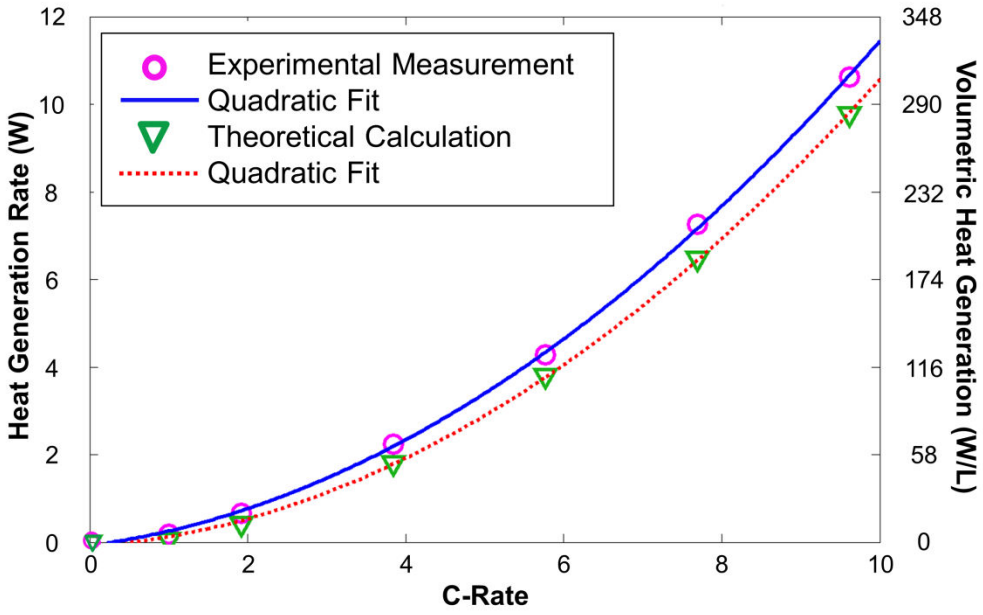

Figure 4-15 Comparison of experimental measurement of average heat generation rate with theoretical model

The entropic heating term in equation (20) is endothermic from fully charged state to an SOC of around 35%, and exothermic below an SOC of 35%. The entropic heating term contributes to the non-linear heat generation curves at lower discharge rates shown in Figure 4-11, while the entropic heating term becomes less significant at higher discharge rates.

The experimentally measured heat generation rate is compared with the theoretical calculation in Table 4-1, and plotted in Figure 4-15. The two are in close agreement, within around 10% at high C-rates. Both curves follow the expected quadratic dependence on C-rate. While the theoretical curve is based on an analytical model that relates heat generation rate to electrical and electrochemical parameters such as current and voltage, the experimental curve represents a purely thermal measurement of the heat generation rate. The deviation between the

two may be attributed to various sources of experimental error and uncertainty, including uncertainty in measurements of heat capacity, temperatures and heat flux. In addition, approximations in the theoretical model may also be a contributing factor.

Table 4-1 Comparison of measured heat generation rates with calculations from theoretical model

C-rate	Heat Generation Rate (W)			
	Experimental	Theoretical	Deviation	Deviation %
1.0	0.19	0.05	0.13	71.2
1.9	0.67	0.42	0.25	36.8
3.8	2.24	1.81	0.43	19.3
5.8	4.28	3.79	0.49	11.4
7.7	7.26	6.48	0.78	10.7
9.6	10.62	9.78	0.84	7.9

Effect of Active Cooling

Heat generation measurement experiments are repeated in the presence of active cooling using a fan. All other experimental conditions are maintained to be the same as the baseline case on an uncooled undrilled cell. Experiments are carried out at a number of C-rates. Figure 4-16 plots the heat stored, heat lost and total heat generated in the cell during 15A discharge as a function of time while being actively cooled.

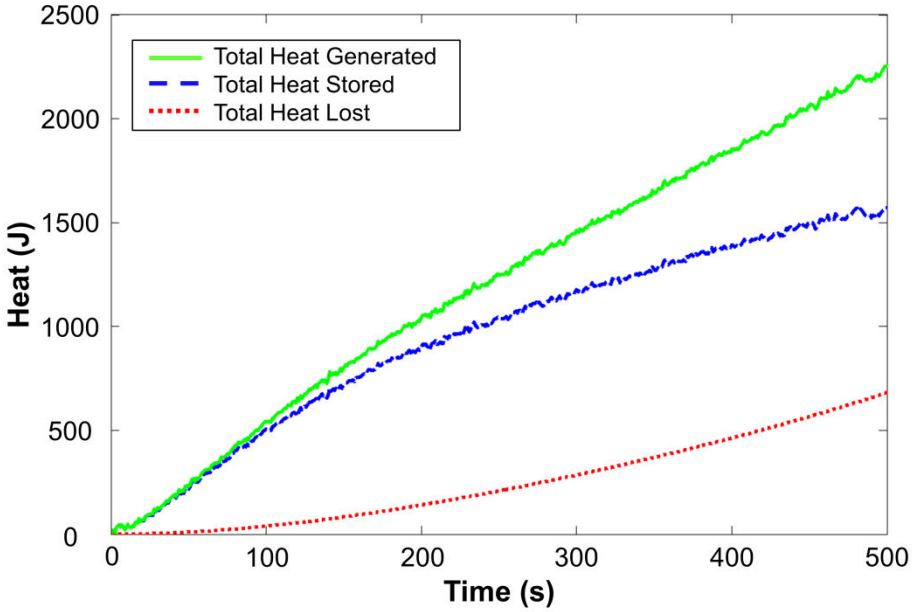

Figure 4-16 Measured heat stored, heat lost and heat generated as functions of time for a cooled cell at 5.8C discharge

In comparison with Figure 4-8, where these data are plotted for the baseline, uncooled cell, there is greater heat lost and lesser heat stored. The total heat generated remains nearly the same as the uncooled case. This is consistent with the presence of active cooling that facilitates greater heat removal, and hence reduced heat stored. Similar behavior in also observed at other C-rates.

Differentiation of the total heat generated curve for the cooled cell results in a plot of heat generation rate as a function of SOC for various C-rates, shown in Figure 4-17(a).

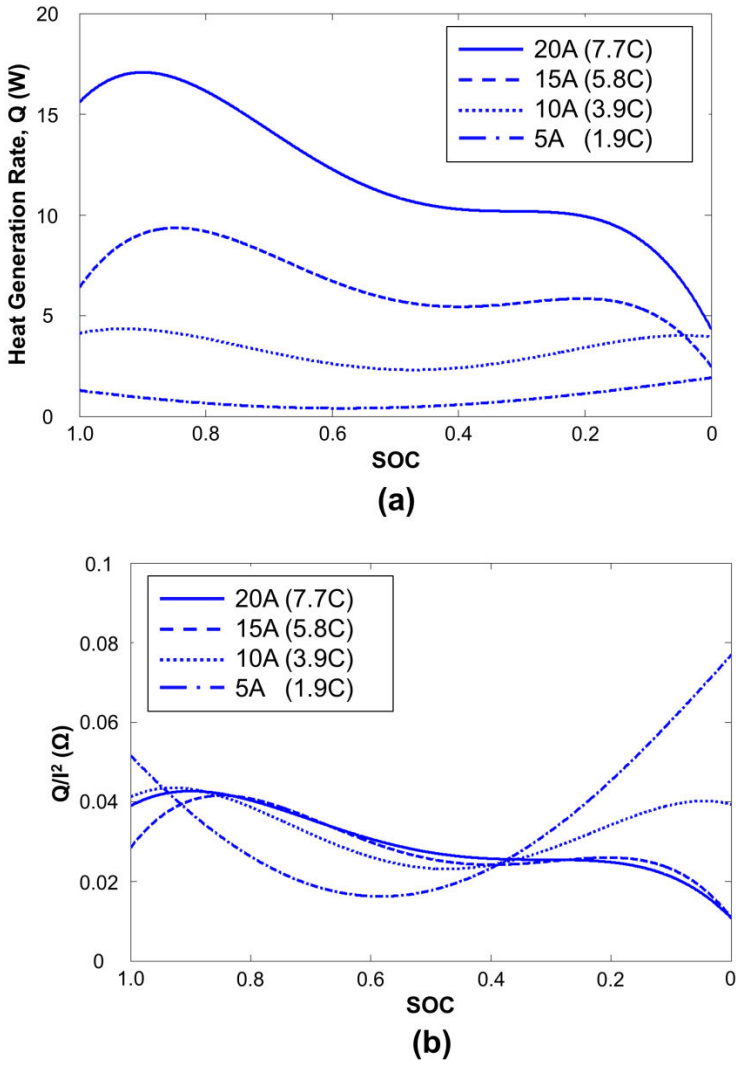

Figure 4-17 (a) Heat generation rate as a function of SOC for different C-rates for a cooled cell, (b) Heat generation rate divided by square of the current as a function of SOC for different C-rates for a cooled cell

Similar to Figure 4-13, the heat generation rates for various C-rates, when divided by I^2, all collapse into a tight band, shown in Figure 4-17(b). The heat generation rate curve for the cooled cell is lower than for the uncooled cell. However, the nature of the variation of heat generation rate as a function of SOC is the same for both cases.

Figure 4-18 compares the overall, average heat generation rate between uncooled and cooled cells at different C-rates.

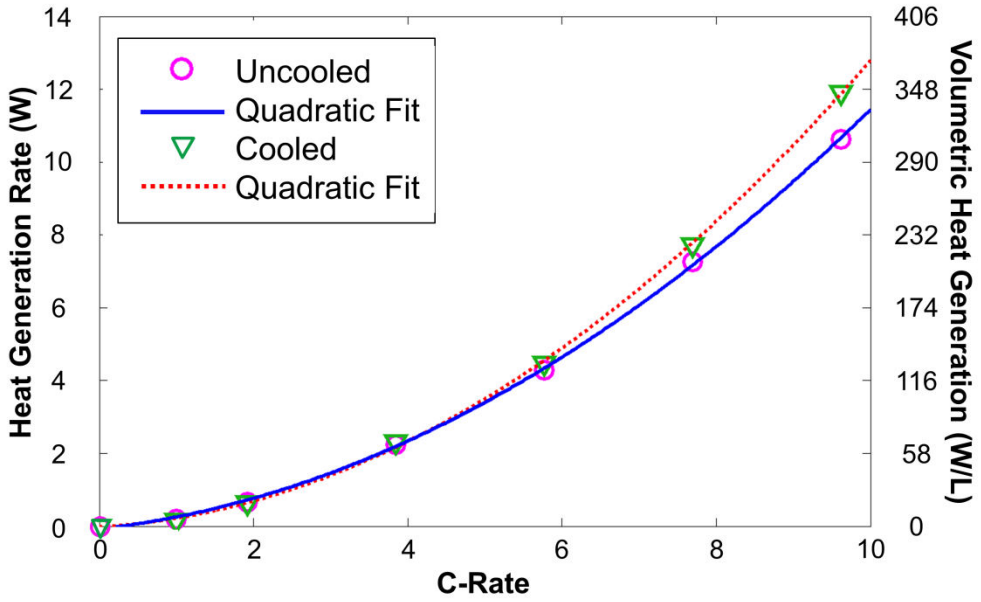

Figure 4-18 Comparison of measured heat generation rate as a function of C-rate for uncooled and cooled cells

Data from these two cases are very close to each other for each C-rate. Figure 4-18, the effective internal resistance is found to be 17.0 and 18.9 m-Ω for the uncooled and cooled cell respectively.

Energy Conversion Efficiency

Any heat generated during the discharge process results in reduction in the efficiency of energy conversion from chemical to electrical form. This energy conversion efficiency may be defined as

$$\eta = \frac{E_{elec}}{E_{elec} + Q} \quad (27)$$

where E_{elec} is the electrical work output.

η is plotted as a function of C-rate for the uncooled cell in Figure 4-19.

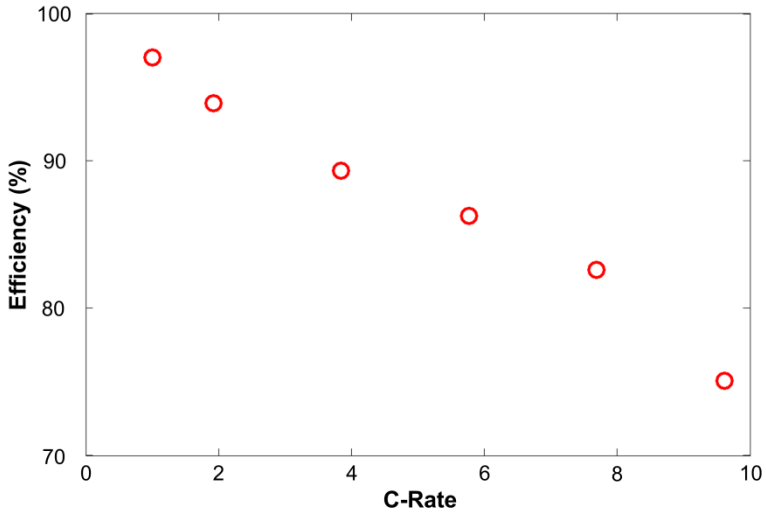

Figure 4-19 Efficiency of energy conversion as a function of C-rate for uncooled and cooled cells

The energy conversion efficiency reduces as C-rate increases, due to the increased heat generation rate at large C-rates. Energy conversion efficiency for the cooled cell is roughly the same, since cooling is found to affect the rate of heat removed, but not the total rate at which heat is generated.

Effect of Cell Drilling on Heat Generation Rate

Determination of core temperature of the baseline, undrilled cell requires one-time drilling, and insertion of a thermocouple into one separate cell. Experiments are also carried out to determine the effect of drilling the cell on heat generation rate. The heat generation rate in the drilled cell is measured at a number of C-rates using the same methodology as the undrilled cell. Figure 4-20 compares heat generation rate at different C-rates for the undrilled and drilled cells.

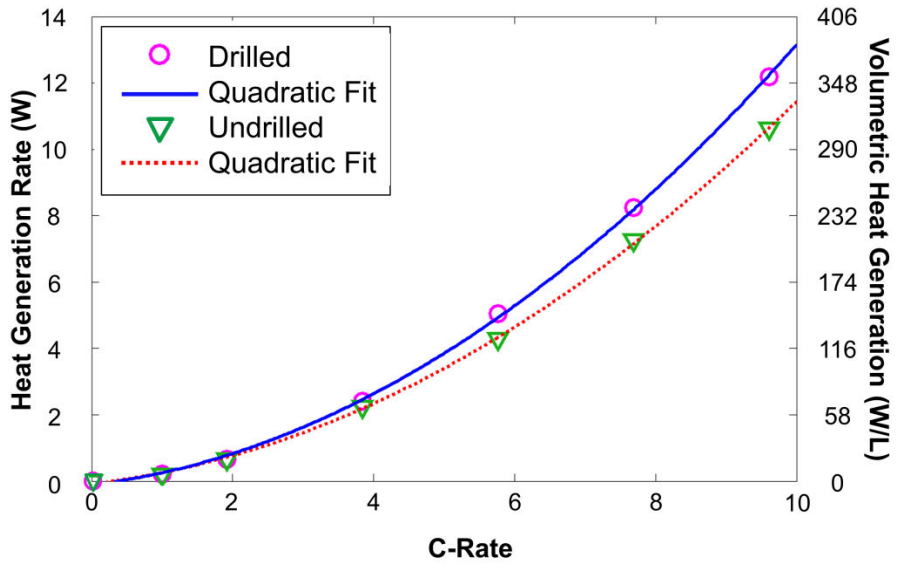

Figure 4-20 Comparison of heat generation rate as a function of C-rate for undrilled and drilled cells

There is a slight increase in heat generation rate as a result of drilling the cell, from 10.5W from the undrilled cell to 12.0W for the drilled cell at 25A, the highest discharge current tested. This is consistent with EIS measurements that indicate negligible change in cell ESR due to drilling.

Conclusion

This section describes a thermal-based *in situ* measurement of heat generation rate in a Li-ion cell under discharge at high C-rates. The method is based on measurement of heat stored in the cell, and heat lost to the ambient and does not rely on the mechanisms governing heat generation in the cell. The method utilizes a novel result from the theory of thermal conduction to determine the volume-averaged cell temperature from only two discrete, point measurements. Experimental data are in excellent agreement with well-known theoretical models for heat generation rate in cells. Results indicate a strong C-rate dependence of heat generation, as expected. The measurement method and data presented here contribute towards the

fundamental understanding of thermal phenomena in Li-ion cells, as well as effective thermal management strategies for reducing operating temperature for Li-ion cells, thereby improving safety, reliability and performance.

Chapter 5

Conclusion and Future Work

Summary

An iterative and progressive approach has been taken that characterizes the physical properties and thermal behavior of 26650 cylindrical li-ion batteries. This methodological process started from the conceptual information based on the fundamental way in which these cells are manufactured. An analytical model was developed that allowed for the several anisotropy within this system to be accounted. The models linear nature permitted experimental capture of these properties. Experimental data and theoretical models are in very good agreement and fall along expected values.

26650 inherent properties were studied on their reaction to simulated aging and states of charge. Cells effective age was determine by the increase in equivalent series resistance and capacity fade. Cells trended in specific directions, but ultimately it was determined that the effects of both aging and SOC were negligible.

Heat generation experiments were performed. These tests included systematically measuring the heat lost through the outer surface of the cell and heat stored within each cell. The combination of these two terms, lead to the total heat generation of the cell. Total heat generation characterization was performed at multiple high discharge C-Rates. Energy supplied to the cells was near to the amount of heat experimentally measured during testing.

Convection exploration over these cells again provided projected results. Total heat generation remained consistent, however heat lost and heat stored components shifted closer to one another as anticipated. Convection allowed for increase in heat loss to the surrounding environment while the internal heat stored decreased.

Thermophysical property characterization was extended to nine other cylindrical energy storage cells. These cells ranged in shapes, internal chemistries, power and energy densities.

Additionally, prismatic and pouch cells were experimentally tested and evaluated. In every case a similar anisotropy was measured with the highest discrepancy being over 700 times larger.

Future Research in Experiment

A significant amount of progress has been made towards a complete thermal understanding in Li-ion cells. The efforts described above should be continued on a wide range of cells. Heat generation measurement and techniques should be extended to the nine larger form factor cells, more specifically analyzing these cells at elevated discharge C-Rates. Heat flux measurements with in rectangular cells would also be of interest. Both cases would provide valuable information and insight to the way in which these cells behave in numerous conditions.

Expanding on 26650 cell tests should comprise of subjecting these cells to elevated discharge rates while introducing them to multiple convection conditions. This should range from zero air flow to subsequent and increasing wind speeds across the outer surface of the cell. Data from these tests can be used to understand the impact of varying air flow speeds, not just about cell's temperature, but internal heat stored and heat generation.

Experiments performed and proposed should be combined for simulated real performance testing. Understanding heat generation in cells should progress beyond a complete and single constant discharge rate. Cells should be subjected to pulsed discharge conditions. For instances a short burst of 10C discharge for 30 seconds, followed by and extended 1C discharge. This cycle would then repeat until the cell is completely discharged. Moving from basic understanding of a system and improving it to relate to real life situations is an important and necessary investigation.

Appendix A

LabVIEW Screen Shots

First LabVIEW Operating Program

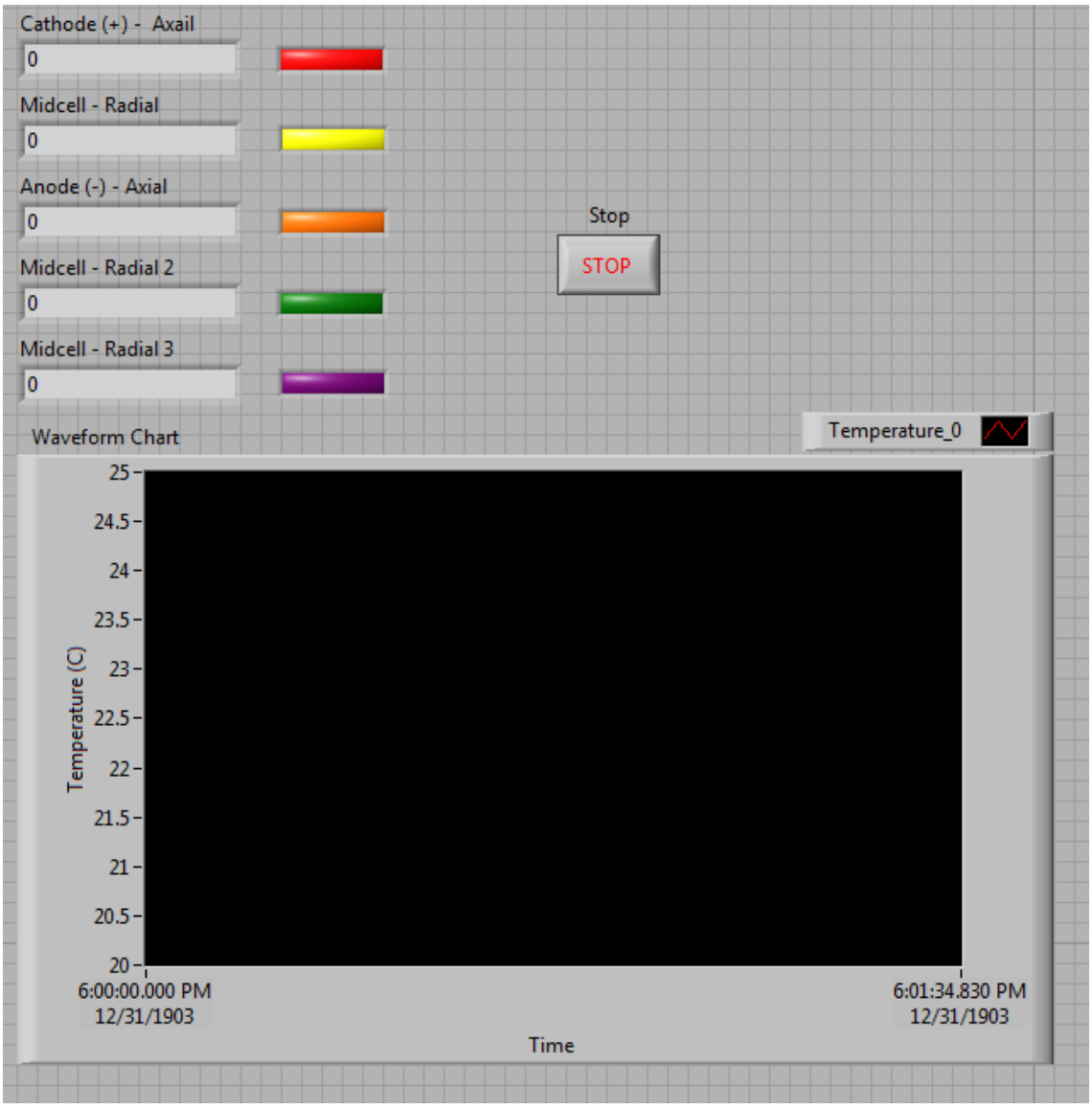

Figure A-1 First LabVIEW front panel

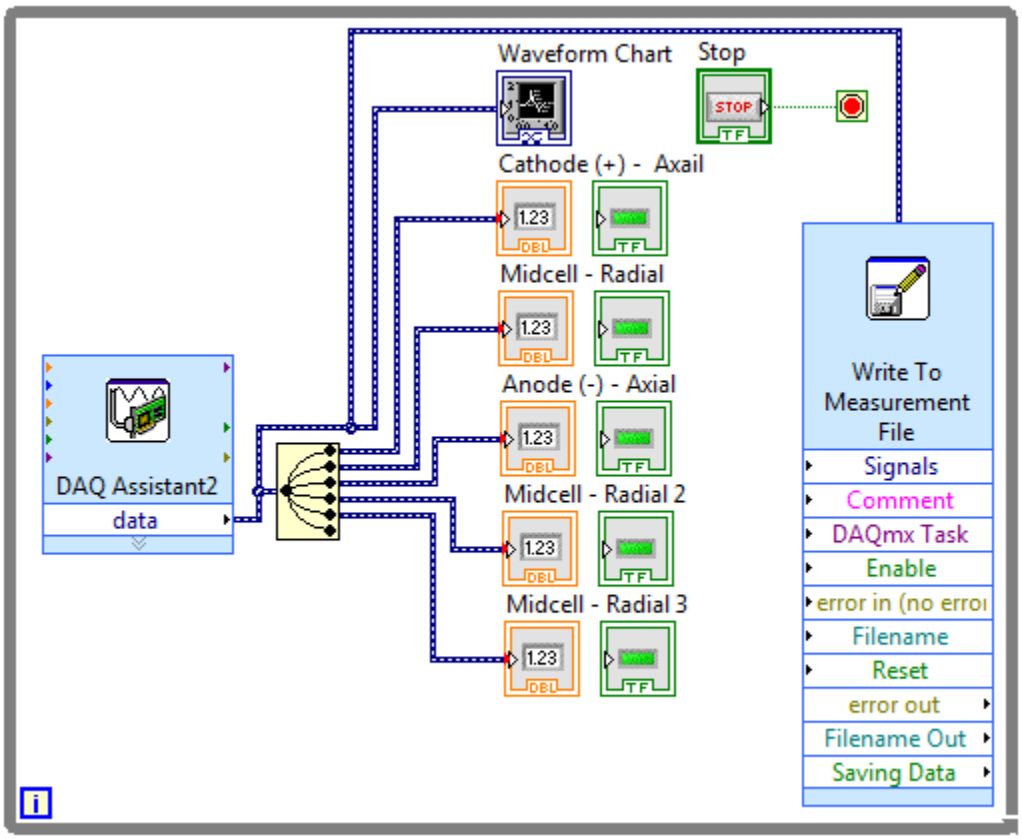

Figure A-2 First LabVIEW block diagram

Constant Power Program

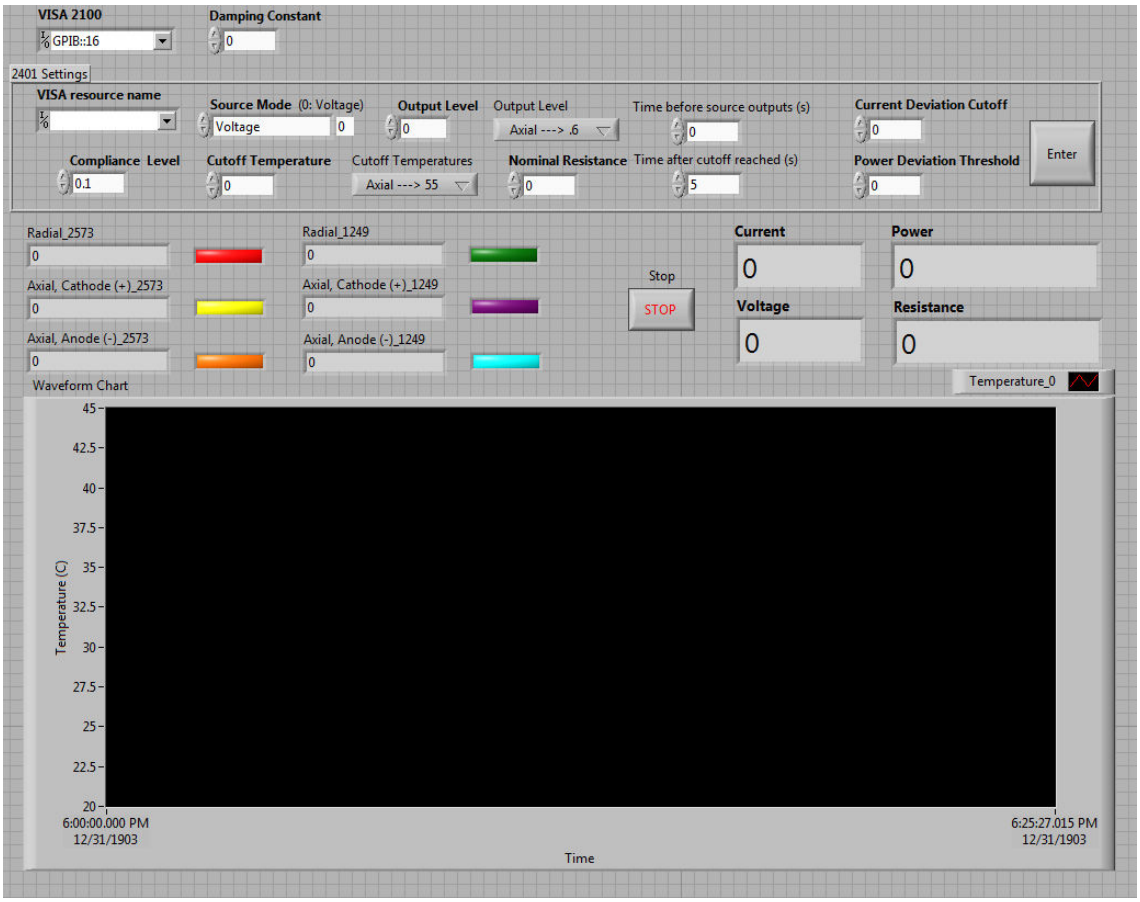

Figure A-3 LabVIEW constant power front panel .vi

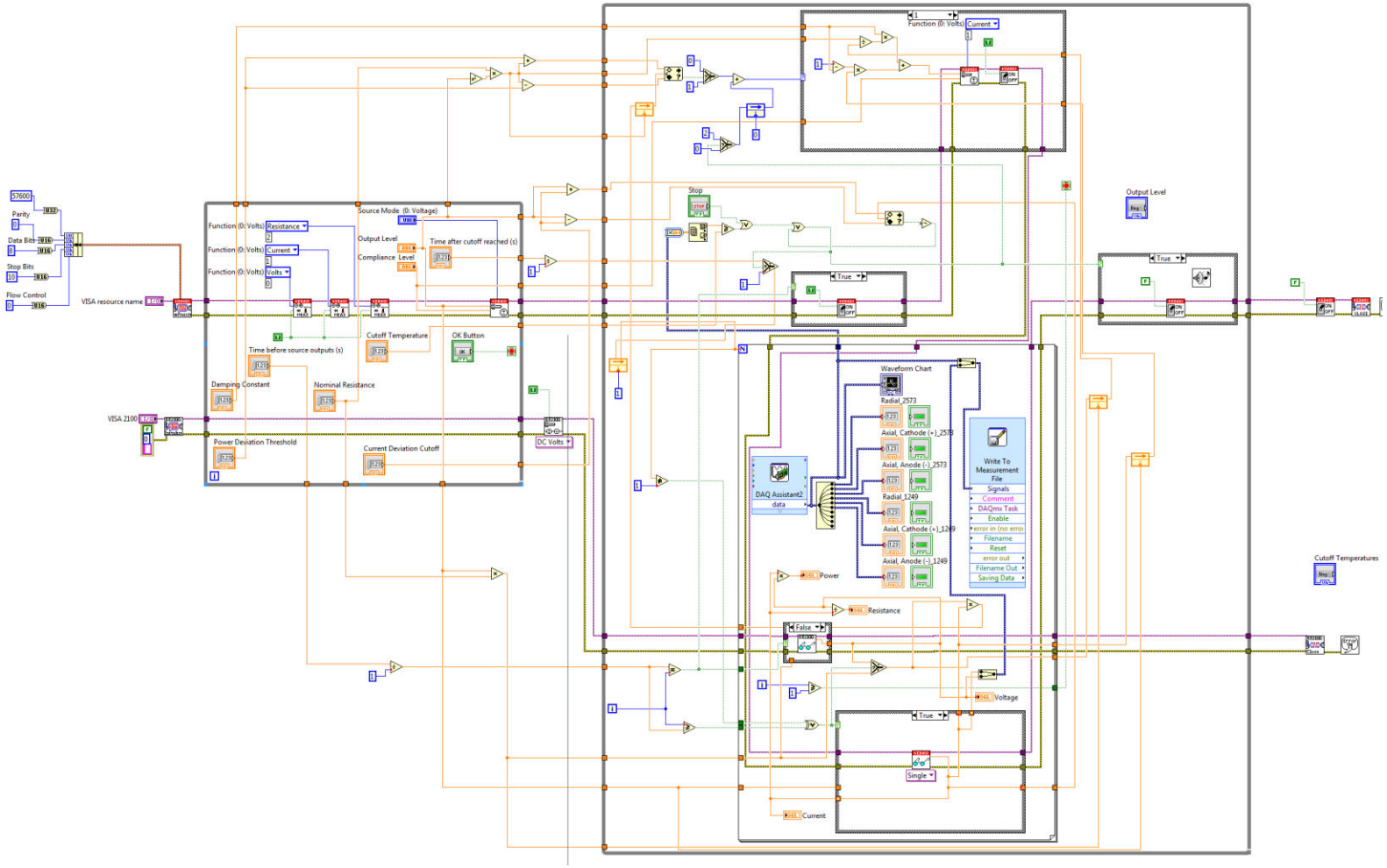

Figure A-4 LabVIEW constant power block diagram .vi

Heat Flux Program

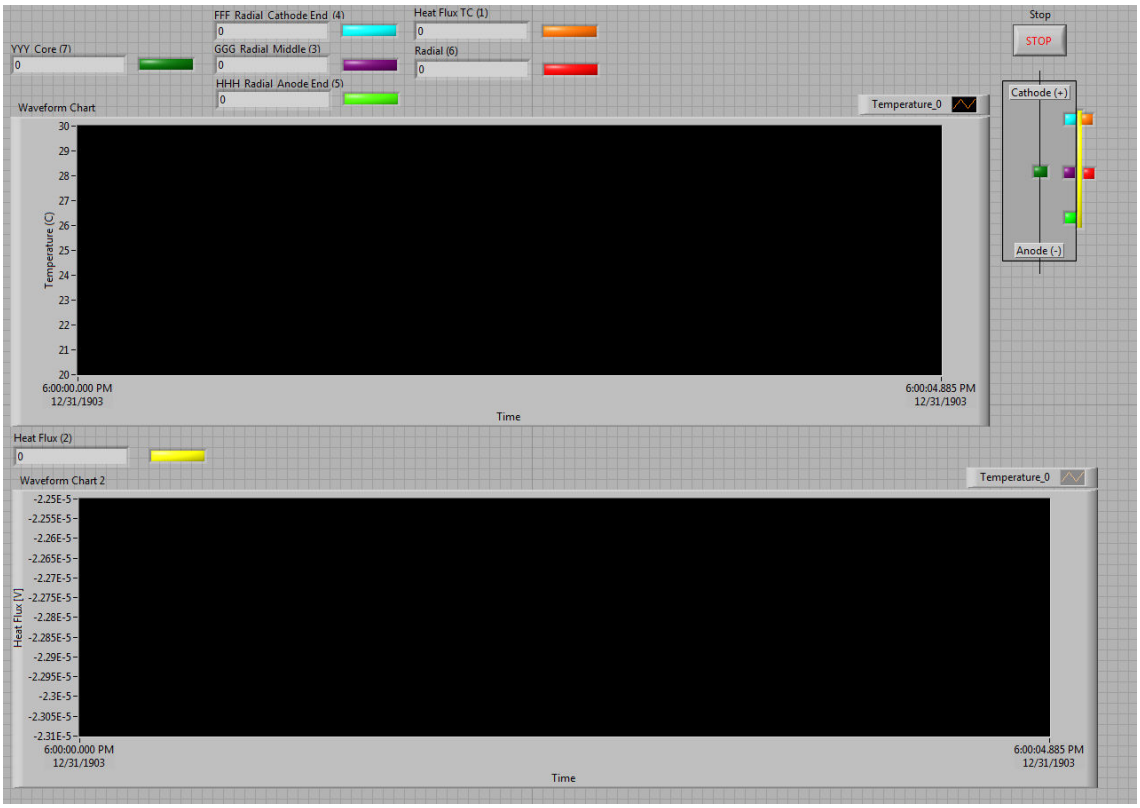

Figure A-5 LabVIEW heat flux measurement front panel .vi

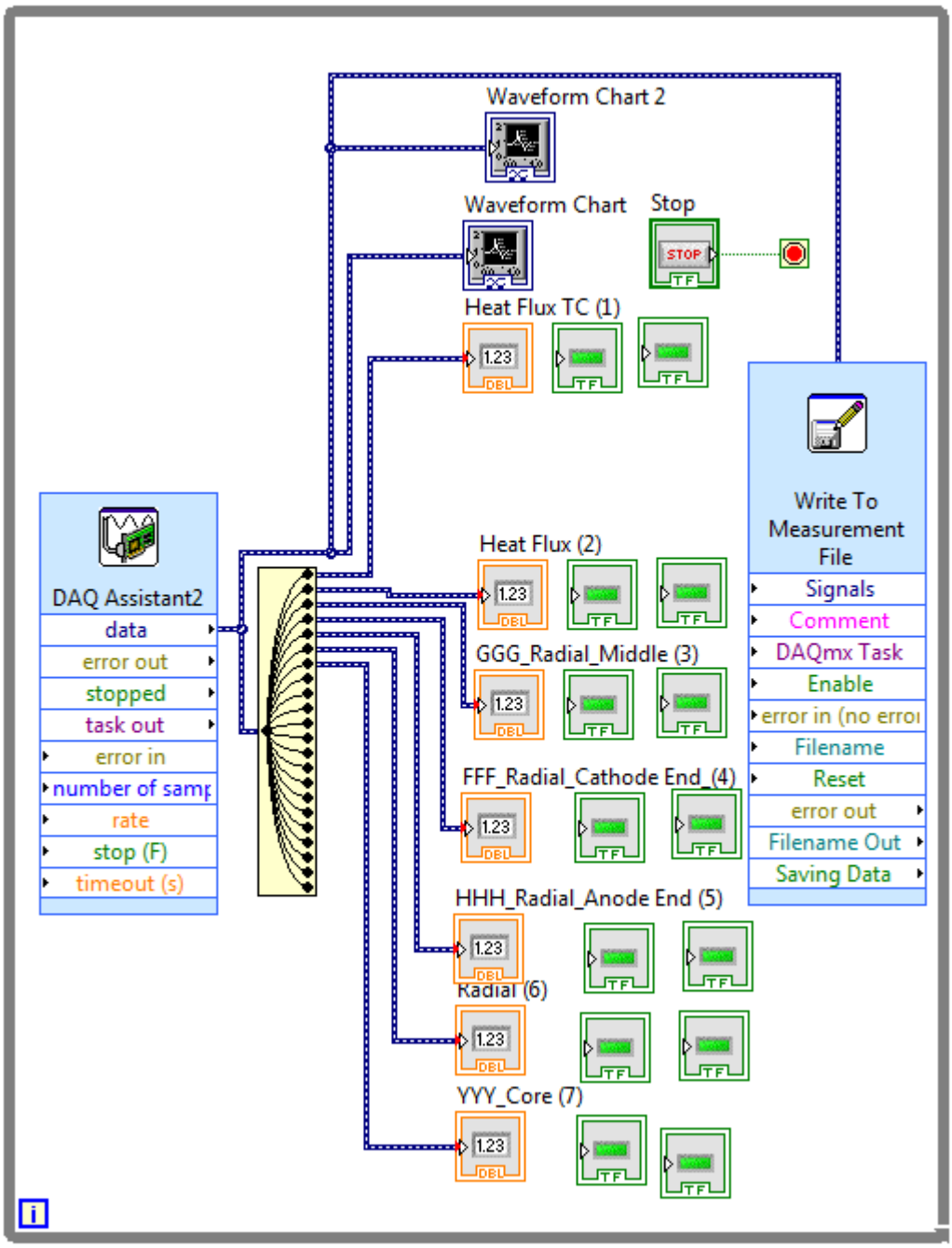

Figure A-6 LabVIEW heat flux measurement block diagram .vi

Pulsed Power Program

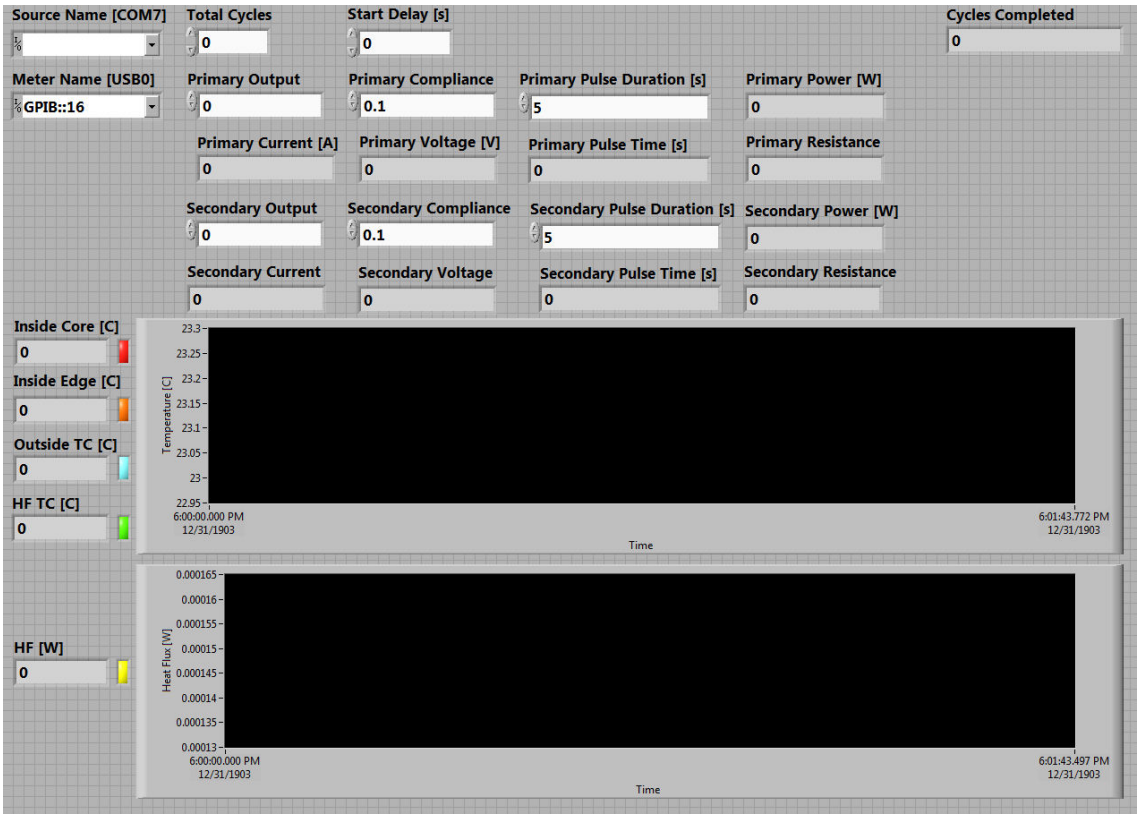

Figure A-7 LabVIEW pulsed power measurement front panel .vi

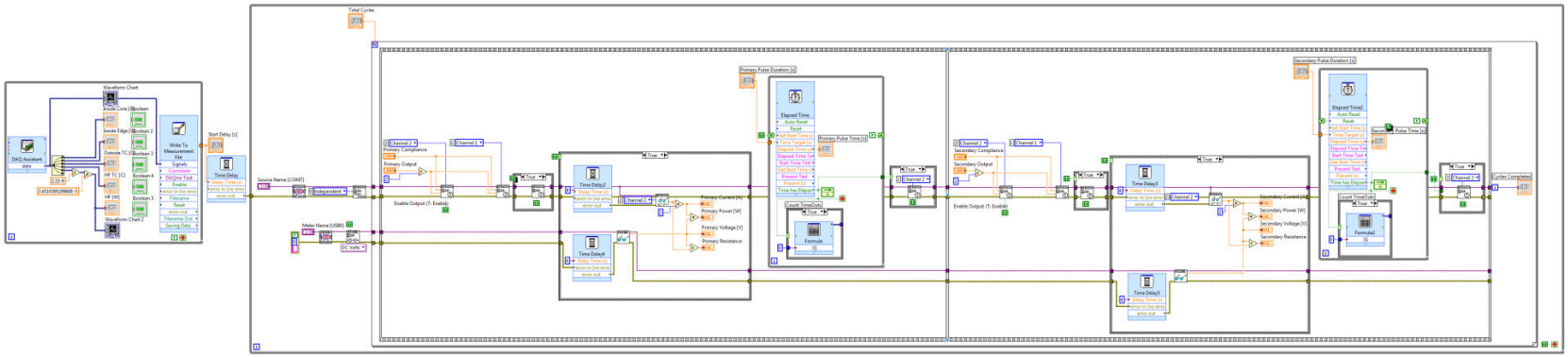

Figure A-8 LabVIEW pulsed power measurement block diagram .vi

Appendix B

MATLAB Code

Experimental Data Plot MATLAB Code

Standard experimental code for plotting experimental data:

```
a=dlmread('26650_3677 - Axial-A - 100_SOC - W3 - 2014 01 13.txt');

timea=a(:,1); %1 is Time

T1=a(:,6); %6 is Axial

%Limits for 26650_3677
lowerlima=120;
upperlima=1950;

timea=timea(lowerlima:upperlima)-timea(lowerlima);
T1=T1(lowerlima:upperlima)-T1(lowerlima);

%figure;
hold on
box on
% grid on

plot(timea,T1,'-b','LineWidth',2)
title('SOC Axial-Anode, 26650-3677 100% SOC W3');
xlabel('Time [s]');
ylabel('Temperature Shift [C]');
```

Radial Model Plot MATLAB Code

Standard radial code for plotting against experimental data:

```
R =.0127; %m
r=.0127; %m
H=.065; %m
SA=(H*2*pi*R); %m^2

V=20.8991;%V
I=0.0999939;%A
P=V*I;

Q=P/SA; %W.m2
rho=2577.7; %kg/m^3

k=.11; %W/m*K                    <-------
Cp=2300; %J/kg*K                 <-------
a=(k)/(Cp*rho); %m^2/s
t=0:2:2000; %s
tmax=length(t);

l=(1/R)*dlmread('besselzeroes.txt');
nmax=length(l);
get_cn;


for i=1:tmax
    A=2*Q/(rho*Cp*R)*t(i); %in Celsius
    B=Q/(k*R)*((r^2)/2-(R^2)/4); %in Celsius

    sum=0;
    for n=1:nmax
         term(n)=c(n)*besselj(0,l(n)*r)*exp(-a*(l(n))^2*t(i));
         sum=sum+term(n);
    end

    T(i)=A+B+sum;
    i
end

figure;
hold on;
box on;
plot(t,T,'-r','LineWidth',2)
title('Mock 2TC - Radial Outside Model');
xlabel('Time [s]');
ylabel('Temperature Shift [C]');
```

Axial Model Plot MATLAB Code

Standard axial code for plotting against experimental data:

```
R=.013; %m
H=.065; %m
z=0; %m

SA=(pi*R^2); %m^2
V=3.31621;%V
I=0.59995;%A
P=V*I; %W
Q=P/SA; %W.m2
rho=2577.7; %kg/m^3

k=30; %W/m*K
Cp=2700; %J/kg*

a=(k)/(Cp*rho); %m^2/s
t=0:1:1000; %s
tmax=length(t);

for i=1:tmax
    A=(Q*t(i))/(rho*Cp*H); %in Celsius
    B=(Q/(2*k*H))*(z^2-(H^2)/3); %in Celsius

    sum=0;
    for n=1:100
         term(n)=((-1)^n)*(2*Q*H/(k*(n*pi)^2))*(cos(n*z*pi/H))*exp(-
a*(n*pi/H)^2*t(i));
         sum=sum+term(n);
    end

    T(i)=A+B-sum;
    i
end

hold on;
box on;
plot(t,T,'-r','LineWidth',2)
```

Data Separation and Parsing MATLAB Code

Standard data processing code for separating and sorting multiple variables of experimental data:

```
%% Trim temp data to match time from cycle data
stop = max(Time_Cycle);
for i = 1:length(Time_Temp)
    if Time_Temp(i) <= stop
        temp1(i) = OuterTop(i);
        temp2(i) = OuterMid(i);
        temp3(i) = OuterBot(i);
        temp4(i) = InnerTop(i);
        temp5(i) = InnerMid(i);
        temp6(i) = InnerBot(i);
        temp7(i) = Ambient(i);
        temp8(i) = HeatFluxVoltage(i);
        temp9(i) = Time_Temp(i);
        pot(i) =Potential(i);
    end
end

raw.OuterTop        = temp1';
raw.OuterMid        = temp2';
raw.OuterBot        = temp3';
raw.InnerTop        = temp4';
raw.InnerMid        = temp5';
raw.InnerBot        = temp6';
raw.Ambient         = temp7';
raw.HeatFluxVoltage = temp8';
raw.Time_Temp       = temp9';
raw.Time_Cycle      = Time_Cycle;
raw.Potential       = Potential;
raw.Current         = Current;
raw.Capacity        = Capacity;

clear temp1 temp2 temp3 temp4 temp5 temp6 temp7 temp8 temp9 i stop;
clear OuterTop OuterMid OuterBot InnerTop InnerMid InnerBot Ambient
HeatFluxVoltage Time_Temp;
clear Time_Cycle Potential Current Capacity;
clc;

%% Plot entire dataset
figure(1)
clf(1)
plot(raw.Time_Cycle,raw.Current);           cute('green',1.2); hold
on;
plot(raw.Time_Temp,raw.OuterTop);           cute('red',1.2);
plot(raw.Time_Temp,raw.OuterMid);           cute('blue',1.2);
plot(raw.Time_Temp,raw.OuterBot);           cute('orange',1.2);
plot(raw.Time_Temp,raw.InnerTop);           cute('yellow',1.2);
```

```
plot(raw.Time_Temp,raw.InnerMid);           cute('magenta',1.2);
plot(raw.Time_Temp,raw.InnerBot);           cute('gray',1.2);
plot(raw.Time_Temp,raw.Ambient);            cute('cyan',1.2);
plot(raw.Time_Temp,raw.HeatFluxVoltage*15000+25);
cute('black',1.2);
plot(raw.Time_Cycle,raw.Potential);           cute('green',1.2); hold
on;

%% 1C ALIGNMENT
clear oneC;
% Use plot to get lower and upper times from the 1C Cycle
title('Select 1C Window!','fontsize',28,'fontweight','bold');
set(1,'units','normalized','outerposition',[0 0 1 1],'Color','w')
[Min,Y] = ginput(1);
[Max,Y] = ginput(1);

% Filter out 1C data into new variables
for i = 1:length(raw.Time_Temp)
    if raw.Time_Temp(i) <= Max && raw.Time_Temp(i) >= Min
        oneC.Temps(i,:) =
[raw.Time_Temp(i),raw.OuterTop(i),raw.OuterMid(i),raw.OuterBot(i),...

raw.InnerTop(i),raw.InnerMid(i),raw.InnerBot(i),raw.Ambient(i),raw.Hea
tFluxVoltage(i)];
    end
end
for i = 1:length(raw.Time_Cycle)
    if raw.Time_Cycle(i) <= Max && raw.Time_Cycle(i) >= Min
        oneC.Cycles(i,:) =
[raw.Time_Cycle(i),raw.Potential(i),raw.Current(i),raw.Capacity(i)];
    end
end

% Get rid of any cells with zeros
temp1 = find(oneC.Temps(:,1));
temp2 = find(oneC.Cycles(:,1));
oneC.Temps = oneC.Temps(temp1,:);
oneC.Cycles = oneC.Cycles(temp2,:);

% Reference to t = 0
oneC.Temps(:,1) = oneC.Temps(:,1) - min(oneC.Temps(:,1));
oneC.Cycles(:,1) = oneC.Cycles(:,1) - min(oneC.Cycles(:,1));
clear Max Min ans i Y temp1 temp2;

%% 5A ALIGNMENT
clear fiveA;
% Use plot to get lower and upper times from the 1C Cycle
title('Select 5A Window!','fontsize',28,'fontweight','bold');
set(1,'units','normalized','outerposition',[0 0 1 1],'Color','w')
[Min,Y] = ginput(1);
[Max,Y] = ginput(1);
```

```
% Filter out 1C data into new variables
for i = 1:length(raw.Time_Temp)
    if raw.Time_Temp(i) <= Max && raw.Time_Temp(i) >= Min
        fiveA.Temps(i,:) =
[raw.Time_Temp(i),raw.OuterTop(i),raw.OuterMid(i),raw.OuterBot(i),...

raw.InnerTop(i),raw.InnerMid(i),raw.InnerBot(i),raw.Ambient(i),raw.Hea
tFluxVoltage(i)];
    end
end
for i = 1:length(raw.Time_Cycle)
    if raw.Time_Cycle(i) <= Max && raw.Time_Cycle(i) >= Min
        fiveA.Cycles(i,:) =
[raw.Time_Cycle(i),raw.Potential(i),raw.Current(i),raw.Capacity(i)];
    end
end

% Get rid of any cells with zeros
temp1 = find(fiveA.Temps(:,1));
temp2 = find(fiveA.Cycles(:,1));
fiveA.Temps = fiveA.Temps(temp1,:);
fiveA.Cycles = fiveA.Cycles(temp2,:);

% Reference to t = 0
fiveA.Temps(:,1) = fiveA.Temps(:,1) - min(fiveA.Temps(:,1));
fiveA.Cycles(:,1) = fiveA.Cycles(:,1) - min(fiveA.Cycles(:,1));
clear Max Min ans i Y temp1 temp2;

%% 10A ALIGNMENT
clear tenA;
% Use plot to get lower and upper times from the 1C Cycle
title('Select 10A Window!','fontsize',28,'fontweight','bold');
set(1,'units','normalized','outerposition',[0 0 1 1],'Color','w')
[Min,Y] = ginput(1);
[Max,Y] = ginput(1);

% Filter out 1C data into new variables
for i = 1:length(raw.Time_Temp)
    if raw.Time_Temp(i) <= Max && raw.Time_Temp(i) >= Min
        tenA.Temps(i,:) =
[raw.Time_Temp(i),raw.OuterTop(i),raw.OuterMid(i),raw.OuterBot(i),...

raw.InnerTop(i),raw.InnerMid(i),raw.InnerBot(i),raw.Ambient(i),raw.Hea
tFluxVoltage(i)];
    end
end
for i = 1:length(raw.Time_Cycle)
    if raw.Time_Cycle(i) <= Max && raw.Time_Cycle(i) >= Min
        tenA.Cycles(i,:) =
[raw.Time_Cycle(i),raw.Potential(i),raw.Current(i),raw.Capacity(i)];
    end
end
```

```
% Get rid of any cells with zeros
temp1 = find(tenA.Temps(:,1));
temp2 = find(tenA.Cycles(:,1));
tenA.Temps = tenA.Temps(temp1,:);
tenA.Cycles = tenA.Cycles(temp2,:);

% Reference to t = 0
tenA.Temps(:,1) = tenA.Temps(:,1) - min(tenA.Temps(:,1));
tenA.Cycles(:,1) = tenA.Cycles(:,1) - min(tenA.Cycles(:,1));
clear Max Min ans i Y temp1 temp2;

%% 15A ALIGNMENT
clear fifteenA;
% Use plot to get lower and upper times from the 1C Cycle
title('Select 15A Window!','fontsize',28,'fontweight','bold');
set(1,'units','normalized','outerposition',[0 0 1 1],'Color','w')
[Min,Y] = ginput(1);
[Max,Y] = ginput(1);

% Filter out 1C data into new variables
for i = 1:length(raw.Time_Temp)
    if raw.Time_Temp(i) <= Max && raw.Time_Temp(i) >= Min
        fifteenA.Temps(i,:) =
[raw.Time_Temp(i),raw.OuterTop(i),raw.OuterMid(i),raw.OuterBot(i),...

raw.InnerTop(i),raw.InnerMid(i),raw.InnerBot(i),raw.Ambient(i),raw.Hea
tFluxVoltage(i)];
    end
end
for i = 1:length(raw.Time_Cycle)
    if raw.Time_Cycle(i) <= Max && raw.Time_Cycle(i) >= Min
        fifteenA.Cycles(i,:) =
[raw.Time_Cycle(i),raw.Potential(i),raw.Current(i),raw.Capacity(i)];
    end
end

% Get rid of any cells with zeros
temp1 = find(fifteenA.Temps(:,1));
temp2 = find(fifteenA.Cycles(:,1));
fifteenA.Temps = fifteenA.Temps(temp1,:);
fifteenA.Cycles = fifteenA.Cycles(temp2,:);

% Reference to t = 0
fifteenA.Temps(:,1) = fifteenA.Temps(:,1) - min(fifteenA.Temps(:,1));
fifteenA.Cycles(:,1) = fifteenA.Cycles(:,1) -
min(fifteenA.Cycles(:,1));
clear Max Min ans i Y temp1 temp2;

%% 20A ALIGNMENT
clear twentyA;
```

```
% Use plot to get lower and upper times from the 1C Cycle
title('Select 20A Window!','fontsize',28,'fontweight','bold');
set(1,'units','normalized','outerposition',[0 0 1 1],'Color','w')
[Min,Y] = ginput(1);
[Max,Y] = ginput(1);

% Filter out 1C data into new variables
for i = 1:length(raw.Time_Temp)
    if raw.Time_Temp(i) <= Max && raw.Time_Temp(i) >= Min
        twentyA.Temps(i,:) =
[raw.Time_Temp(i),raw.OuterTop(i),raw.OuterMid(i),raw.OuterBot(i),...

raw.InnerTop(i),raw.InnerMid(i),raw.InnerBot(i),raw.Ambient(i),raw.Hea
tFluxVoltage(i)];
    end
end
for i = 1:length(raw.Time_Cycle)
    if raw.Time_Cycle(i) <= Max && raw.Time_Cycle(i) >= Min
        twentyA.Cycles(i,:) =
[raw.Time_Cycle(i),raw.Potential(i),raw.Current(i),raw.Capacity(i)];
    end
end

% Get rid of any cells with zeros
temp1 = find(twentyA.Temps(:,1));
temp2 = find(twentyA.Cycles(:,1));
twentyA.Temps = twentyA.Temps(temp1,:);
twentyA.Cycles = twentyA.Cycles(temp2,:);

% Reference to t = 0
twentyA.Temps(:,1) = twentyA.Temps(:,1) - min(twentyA.Temps(:,1));
twentyA.Cycles(:,1) = twentyA.Cycles(:,1) - min(twentyA.Cycles(:,1));
clear Max Min ans i Y temp1 temp2;

%% 25A ALIGNMENT
clear twentyfiveA;
% Use plot to get lower and upper times from the 1C Cycle
title('Select 25A Window!','fontsize',28,'fontweight','bold');
set(1,'units','normalized','outerposition',[0 0 1 1],'Color','w')
[Min,Y] = ginput(1);
[Max,Y] = ginput(1);

% Filter out 1C data into new variables
for i = 1:length(raw.Time_Temp)
    if raw.Time_Temp(i) <= Max && raw.Time_Temp(i) >= Min
        twentyfiveA.Temps(i,:) =
[raw.Time_Temp(i),raw.OuterTop(i),raw.OuterMid(i),raw.OuterBot(i),...

raw.InnerTop(i),raw.InnerMid(i),raw.InnerBot(i),raw.Ambient(i),raw.Hea
tFluxVoltage(i)];
    end
end
```

```
for i = 1:length(raw.Time_Cycle)
    if raw.Time_Cycle(i) <= Max && raw.Time_Cycle(i) >= Min
        twentyfiveA.Cycles(i,:) =
[raw.Time_Cycle(i),raw.Potential(i),raw.Current(i),raw.Capacity(i)];
    end
end

% Get rid of any cells with zeros
temp1 = find(twentyfiveA.Temps(:,1));
temp2 = find(twentyfiveA.Cycles(:,1));
twentyfiveA.Temps = twentyfiveA.Temps(temp1,:);
twentyfiveA.Cycles = twentyfiveA.Cycles(temp2,:);

% Reference to t = 0
twentyfiveA.Temps(:,1) = twentyfiveA.Temps(:,1) -
min(twentyfiveA.Temps(:,1));
twentyfiveA.Cycles(:,1) = twentyfiveA.Cycles(:,1) -
min(twentyfiveA.Cycles(:,1));
clear Max Min ans i Y temp1 temp2;

%% Plot 1C Temps
figure(2)
plot(oneC.Temps(:,1)/60,oneC.Temps(:,2)); cute('green',1.2); hold on;
plot(oneC.Temps(:,1)/60,oneC.Temps(:,3)); cute('red',1.2);
plot(oneC.Temps(:,1)/60,oneC.Temps(:,4)); cute('blue',1.2);
plot(oneC.Temps(:,1)/60,oneC.Temps(:,5)); cute('orange',1.2);
plot(oneC.Temps(:,1)/60,oneC.Temps(:,6)); cute('yellow',1.2);
plot(oneC.Temps(:,1)/60,oneC.Temps(:,7)); cute('magenta',1.2);
plot(oneC.Temps(:,1)/60,oneC.Temps(:,8)); cute('gray',1.2);

alphc=oneC.Temps(:,6)-oneC.Temps(1,6)
alphac=oneC.Temps(:,3)-oneC.Temps(1,3)

plot_label('1C Discharge ','Time (Min)','Temperature (DegC)',...
           {'Outer Top','Outer Mid','Outer Bot','Inner Top','Inner
Mid',...
            'Inner Bot','Ambient','Heat Flux Voltage'});

axis([0 max(oneC.Temps(:,1))/60+1 23 max(oneC.Temps(:,6))+5]);
%% Plot 5A Temps
figure(3)
plot(fiveA.Temps(:,1)/60,fiveA.Temps(:,2)); cute('green',1.2); hold
on;
plot(fiveA.Temps(:,1)/60,fiveA.Temps(:,3)); cute('red',1.2);
plot(fiveA.Temps(:,1)/60,fiveA.Temps(:,4)); cute('blue',1.2);
plot(fiveA.Temps(:,1)/60,fiveA.Temps(:,5)); cute('orange',1.2);
plot(fiveA.Temps(:,1)/60,fiveA.Temps(:,6)); cute('yellow',1.2);
plot(fiveA.Temps(:,1)/60,fiveA.Temps(:,7)); cute('magenta',1.2);
plot(fiveA.Temps(:,1)/60,fiveA.Temps(:,8)); cute('gray',1.2);

alpha=fiveA.Temps(:,6)-fiveA.Temps(1,6);
```

```
alphab=fiveA.Temps(:,3)-fiveA.Temps(1,3);

plot_label('5A Discharge ','Time (Min)','Temperature (DegC)',...
           {'Outer Top','Outer Mid','Outer Bot','Inner Top','Inner
Mid',...
            'Inner Bot','Ambient','Heat Flux Voltage'});

axis([0 max(fiveA.Temps(:,1))/60+1 23 max(fiveA.Temps(:,6))+5]);
%% Plot 10A Temps
figure(4)
plot(tenA.Temps(:,1)/60,tenA.Temps(:,2)); cute('green',1.2); hold on;
plot(tenA.Temps(:,1)/60,tenA.Temps(:,3)); cute('red',1.2);
plot(tenA.Temps(:,1)/60,tenA.Temps(:,4)); cute('blue',1.2);
plot(tenA.Temps(:,1)/60,tenA.Temps(:,5)); cute('orange',1.2);
plot(tenA.Temps(:,1)/60,tenA.Temps(:,6)); cute('yellow',1.2);
plot(tenA.Temps(:,1)/60,tenA.Temps(:,7)); cute('magenta',1.2);
plot(tenA.Temps(:,1)/60,tenA.Temps(:,8)); cute('gray',1.2);

beta=tenA.Temps(:,6)-tenA.Temps(1,6)
betab=tenA.Temps(:,3)-tenA.Temps(1,3)

%plot(tenA.Temps(:,1),beta); cute('yellow',1.2);

plot_label('10A Discharge ','Time (Min)','Temperature (DegC)',...
           {'Outer Top','Outer Mid','Outer Bot','Inner Top','Inner
Mid',...
            'Inner Bot','Ambient','Heat Flux Voltage'});

axis([0 max(tenA.Temps(:,1))/60+1 23 max(tenA.Temps(:,6))+5]);
%% Plot 15A Temps
figure(5)
plot(fifteenA.Temps(:,1)/60,fifteenA.Temps(:,2)); cute('green',1.2);
hold on;
plot(fifteenA.Temps(:,1)/60,fifteenA.Temps(:,3)); cute('red',1.2);
plot(fifteenA.Temps(:,1)/60,fifteenA.Temps(:,4)); cute('blue',1.2);
plot(fifteenA.Temps(:,1)/60,fifteenA.Temps(:,5)); cute('orange',1.2);
plot(fifteenA.Temps(:,1)/60,fifteenA.Temps(:,6)); cute('yellow',1.2);
plot(fifteenA.Temps(:,1)/60,fifteenA.Temps(:,7)); cute('magenta',1.2);
plot(fifteenA.Temps(:,1)/60,fifteenA.Temps(:,8)); cute('gray',1.2);

gamma=fifteenA.Temps(:,6)-fifteenA.Temps(1,6);
gammab=fifteenA.Temps(:,3)-fifteenA.Temps(1,3);

%plot(fifteenA.Temps(:,1),gamma); cute('yellow',1.2);


plot_label('15A Discharge ','Time (Min)','Temperature (DegC)',...
           {'Outer Top','Outer Mid','Outer Bot','Inner Top','Inner
Mid',...
            'Inner Bot','Ambient','Heat Flux Voltage'});
```

```
axis([0 max(fifteenA.Temps(:,1))/60+1 23 max(fifteenA.Temps(:,6))+5]);
%% Plot 20A Temps
figure(6)
plot(twentyA.Temps(:,1)/60,twentyA.Temps(:,2)); cute('green',1.2);
hold on;
plot(twentyA.Temps(:,1)/60,twentyA.Temps(:,3)); cute('red',1.2);
plot(twentyA.Temps(:,1)/60,twentyA.Temps(:,4)); cute('blue',1.2);
plot(twentyA.Temps(:,1)/60,twentyA.Temps(:,5)); cute('orange',1.2);
plot(twentyA.Temps(:,1)/60,twentyA.Temps(:,6)); cute('yellow',1.2);
plot(twentyA.Temps(:,1)/60,twentyA.Temps(:,7)); cute('magenta',1.2);
plot(twentyA.Temps(:,1)/60,twentyA.Temps(:,8)); cute('gray',1.2);

gammd=twentyA.Temps(:,6)-twentyA.Temps(1,6);
gammad=twentyA.Temps(:,3)-twentyA.Temps(1,3);

plot_label('20A Discharge ','Time (Min)','Temperature (DegC)',...
           {'Outer Top','Outer Mid','Outer Bot','Inner Top','Inner
Mid',...
            'Inner Bot','Ambient','Heat Flux Voltage'});

axis([0 max(twentyA.Temps(:,1))/60+1 23 max(twentyA.Temps(:,6))+5]);
%% Plot 25A Temps
figure(7)
plot(twentyfiveA.Temps(:,1)/60,twentyfiveA.Temps(:,2));
cute('green',1.2); hold on;
plot(twentyfiveA.Temps(:,1)/60,twentyfiveA.Temps(:,3));
cute('red',1.2);
plot(twentyfiveA.Temps(:,1)/60,twentyfiveA.Temps(:,4));
cute('blue',1.2);
plot(twentyfiveA.Temps(:,1)/60,twentyfiveA.Temps(:,5));
cute('orange',1.2);
plot(twentyfiveA.Temps(:,1)/60,twentyfiveA.Temps(:,6));
cute('yellow',1.2);
plot(twentyfiveA.Temps(:,1)/60,twentyfiveA.Temps(:,7));
cute('magenta',1.2);
plot(twentyfiveA.Temps(:,1)/60,twentyfiveA.Temps(:,8));
cute('gray',1.2);

gammdw=twentyfiveA.Temps(:,6)-twentyfiveA.Temps(1,6)
gammaw=twentyfiveA.Temps(:,3)-twentyfiveA.Temps(1,3)

plot_label('25A Discharge ','Time (Min)','Temperature (DegC)',...
           {'Outer Top','Outer Mid','Outer Bot','Inner Top','Inner
Mid',...
            'Inner Bot','Ambient','Heat Flux Voltage'});

axis([0 max(twentyfiveA.Temps(:,1))/60+1 23
max(twentyfiveA.Temps(:,6))+5]);
```

Heat Generation Analysis Plot MATLAB Code

Standard heat flux sensor and thermocouple code for separating total energy into heat stored, heat lost, and the total heat generated:

```
%% Plot Setup
set(0,'DefaultAxesFontName', 'Arial')
set(0,'DefaultAxesFontSize', 20)
set(0,'DefaultTextFontname', 'Arial')
set(0,'DefaultTextFontSize', 20)
figure('Color',[1 1 1]); hold on; box on
title('26650 3824 - UnDrilled 15A RATIO-ed Internal Temp');
xlabel('Time [s]'); ylabel('Heat [J]'); % Set Plot Labels
set(gca,'FontSize',20,'fontWeight','bold')
set(findall(gcf,'type','text'),'FontSize',20,'fontWeight','bold')

%%
clear

data=dlmread('26650_3824_15A_Time_Out_In_HF_RATIO4UnDrilled.txt');

time=data(:,1); %1 is Time
hf=data(:,4); %4 is HF
intc=data(:,3); % 3 TC inside cell at H/2
otc=data(:,2); % 2 TC outside cell at H/2

tc=(intc+otc)/2;

hfv=hf*1e6;

hfsWm2=hfv/2.1; % in W/m2; 2.1 uV/(W/m2) is the correction factor

Tinitial=tc(1);
rho=2285; % kg/m3
Cp=1700; % J/kgK
R=13e-3; %m
H=65e-3; %m
Vol=pi*R^2*H;
SA=2*pi*R*H;

for i=1:length(time)
  totalheatout(i)=integ1d(hfsWm2(1:i),0,time(i))*SA; % in J
  totalheatstored(i)=rho*Vol*Cp*(tc(i)-Tinitial);
  totalheatgen(i)=totalheatout(i)+totalheatstored(i);
end
% avgheatout=max(totalheatout)/max(time); % in W

hold on
```

```
%Final heat numbers, convert to string for placement in plot
gennumber=strcat ('Total Heat
Generated:',num2str(max(totalheatstored)+max(totalheatout)))
storednumber=strcat ('Total Heat
Stored:',num2str(max(totalheatstored)))
lostnumber=strcat('Total Heat Lost:',num2str(max(totalheatout)))

%Plot heat curves
plot(time,(totalheatstored+totalheatout),'-g','LineWidth',4)
plot(time,totalheatstored,'-b','LineWidth',4)
plot(time,totalheatout,'-r','LineWidth',4)

%Write legend
legend(gennumber,storednumber,lostnumber,'Location','NorthWest')

%Calculate powers
powergen=max(totalheatgen)/(length(time))
powerstored=max(totalheatstored)/(length(time))
powerlost=max(totalheatout)/(length(time))

%Power numbers, convert to string for placement in plot
pgennumber=strcat ('Total Power
Generated:',num2str(max(totalheatgen)/(length(time))),'[W]');
pstorednumber=strcat ('Total Power
Stored:',num2str(max(totalheatstored)/(length(time))),'[W]');
plostnumber=strcat('Total Power
Lost:',num2str(max(totalheatout)/(length(time))),'[W]');

%Create and parameterize textbox
annotation('textbox',...
    [0.137 0.62 0.34 0.12],...
    'String',{[pgennumber],[pstorednumber],[plostnumber]},...
    'FontSize',20,...
    'FontName','Arial',...
    'LineStyle','-',...
    'EdgeColor',[0 0 0],...
    'LineWidth',2,...
    'BackgroundColor',[1 1 1],...
    'Color',[0 0 0]);
```

True Power Plot MATLAB Code

```
%Standard code for extrapolating true power from multiple test sets

potential and converting each time domain into 0-100% state of charge:

A26data=dlmread('26650_3824_Drilled_NoFan_1C_Potential.txt');
t26A=A26data(:,1);
V26A=A26data(:,5);

A5data=dlmread('26650_3824_Drilled_NoFan_5A_Potential.txt');
t5A=A5data(:,1);
V5A=A5data(:,5);

A10data=dlmread('26650_3824_Drilled_NoFan_10A_Potential.txt');
t10A=A10data(:,1);
V10A=A10data(:,5);

A15data=dlmread('26650_3824_Drilled_NoFan_15A_Potential.txt');
t15A=A15data(:,1);
V15A=A15data(:,5);

A20data=dlmread('26650_3824_Drilled_NoFan_20A_Potential.txt');
t20A=A20data(:,1);
V20A=A20data(:,5);

A25data=dlmread('26650_3824_Drilled_NoFan_25A_Potential.txt');
t25A=A25data(:,1);
V25A=A25data(:,5);


SOC26A=[1:-1/(length(t26A)-1):0];
SOC5A=[1:-1/(length(t5A)-1):0];
SOC10A=[1:-1/(length(t10A)-1):0];
SOC15A=[1:-1/(length(t15A)-1):0];
SOC20A=[1:-1/(length(t20A)-1):0];
SOC25A=[1:-1/(length(t25A)-1):0];

Curr=5; %CHANGE
imax=101;
for i=1:imax
    SOC(i)=1-(i-1)/(imax-1);
%    U(i)=interpolatereverse(SOC(i),SOC1C,V1C); % this assumes U=V@1C
which
%    may not be accurate. There is an alternate way - to calculate U
by
%    extrapolating the experimental V vs I curve at the given SOC

    Iplot=[2.6 5 10 15 20 25];
```

```
    Vplot=[interpolatereverse(SOC(i),SOC26A,V26A)
interpolatereverse(SOC(i),SOC5A,V5A)
interpolatereverse(SOC(i),SOC10A,V10A)
interpolatereverse(SOC(i),SOC15A,V15A)
interpolatereverse(SOC(i),SOC20A,V20A)
interpolatereverse(SOC(i),SOC25A,V25A)];
    %figure; hold on
    %plot(Iplot,Vplot,'ro');
    a=polyfit(Iplot,Vplot,1);
    U(i)=a(2);
    Uapprox(i)=interpolatereverse(SOC(i),SOC26A,V26A);
    V(i)=interpolatereverse(SOC(i),SOC5A,V5A); %CHANGE
    Q(i)=Curr*(U(i)-V(i));
    Qapprox(i)=Curr*(Uapprox(i)-V(i));
end

%figure; hold on
plot(SOC,Qapprox,'r-','LineWidth',2);
plot(SOC,Q,'r:','LineWidth',2);
Q5Amean=mean(Q)
Q5Ameanapprox=mean(Qapprox)
```

References

[Abraham *et al*., 2006] D. Abraham, E. Roth, R. Kostecki, K. McCarthy, S. MacLaren, D. Doughty, J. Power Sources 161(2006) 648.

[Armand *et al*., 2008] M. Armand, J-M. Tarascon, Nature 451(2008) 652-657.

[Aurbach *et al*., 2007] D. Aurbach, B. Markovsky, G. Salitra, E. Markevich, Y. Talyossef, M. Koltypin, L. Nazar, B. Ellis, and D. Kovacheva, J. Power Sources 165(2007) 491.

[Balakrishnan *et la*., 2006] Balakrishnan, P.g., R. Ramesh, and T. Prem Kumar. J. Power Sources 155 (2006)401-14.

[Bandhauer *et al*., 2011] T.M. Bandhauer, S. Garimella, T. Fuller, J. Electrochem. Soc. 158 (2011) R1-R25.

[Baoquan *et al*., 2012] L. Baoquan, et al. "Control method of the transient compensation process of a hybrid energy storage system based on battery and Ultra-capacitor in Micro-grid," *Industrial Electronics (ISIE), 2012 IEEE International Symposium on* , vol., no., pp.1325,1329, 28-31 May 2012.

[Belt *et al*., 2005] J.R. Belt, C.D. Ho, T.J. Miller, M.A. Habib, T.Q. Duong, J. Power Sources 142 (2005) 354-360.

[Bernardi *et al.*, 1985] D. Bernardi, E. Pawlikowski, J. Newman, J. Electrochem. Soc. 132 (1985) 5-12.

[Broussely *et al.*, 2002] M. Broussely, 'Aging mechanisms in Li-ion batteries and life prediction', In: 'Advances in Lithium-ion batteries', W.A.V. Schalkwijk, B. Scrosati (Eds.), Kluwer Academic/Plenum Publishers, New York, 2002.

[Cahill *et al.*, 2002] D.G. Cahill, K.E. Goodson, A. Majumdar, Trans. ASME J. Heat Transfer 124 (2002) 223-241.

[Cavas, 2008] Cavas, Christopher P. "Explosion May Endanger SEAL Mini-sub Program." www.navytimes.com. 9 Dec. 2008. Web.

[Chen *et al.*, 1993] Y. Chen, J.W. Evans, J. Electrochem. Soc. 140 (1993) 1833-1838.

[Chen *et al.*, 1996] Y. Chen, J.W. Evans, J. Electrochem. Soc. 143(1996) 2708.

[Chen *et al.*, 2005] S.C. Chen, C.C. Wan, Y.Y. Wang, J. Power Sources 140 (2005) 111-124.

[Drake *et al.*, 2014] S.J. Drake, D.A. Wetz, J.K. Ostanek, S.P. Miller, J.M. Heinzel, A. Jain, J. Power Sources 252 (2014) 298-304.

[Fang *et al.*, 2010] W. Fang, O.J. Kwon, C-Y. Wang, Int. J. Energy Res. 34 (2010) 107-115.

[Forgez *et al.*, 2010] C. Forgez, D.V. Do, G. Friedrich, M. Morcrette, C. Delacourt, J. Power Sources 195 (2010) 2961–2968.

[Goodenough *et al.*, 2013] J. Goodenough, K. Park, J. Am. Chem. Soc. 135(2013) 1167–1176.

[Hammami *et al.*, 2003] Hammami, Amer, Nathalie Raymond, and Michel Armand. "Lithium-ion Batteries: Runaway Risk of Forming Toxic Compounds." *Nature* 424.6949 (2003): 635-36.

[Incroperia *et al.*, 2002] Incropera, Frank P., and David P. DeWitt. Fundamentals of Heat and Mass Transfer. New York: Wiley, 2002. Print.

[Jain *et al.*, 2008] A. Jain, K.E. Goodson, ASME Trans. J. Heat Transfer 130 (2008) 1-7.

[Johnson *et al.*, 1998] B. Johnson, R. White, J. Power Sources 70(1998) 48.

[Kahn *et al.*, 2011] M. Kahn, K. White, R.T. Long, Lithium-ion batteries hazard and use assessment, Springer, 2011.

[Katzman, 2012] Joe Katzman. "US Destroyers Get a HED: More Power to Them!" Defense Industry Daily RSS News. N.p., 9 May 2012. Web.

[Khateeb *et al*., 2004] S.A. Khateeb, M.M. Farid, J.R. Selman, S. Al-Hallaj, J. Power Sources 128 (2004) 292–307.

[Kim *et al*., 2007] G-H. Kim, A. Pesaran, R. Spotnitz, J. Power Sources 170 (2007) 476–489.

[Kobayashi *et al*., 2002] Y. Kobayashi, H. Miyashiro, K. Kumai, K. Takei, T. Iwahori, I. Uchida, J. Electrochem. Soc. 149(2002) A978.

[Khaligh *et al*., 2010] A. Khaligh, Z. Li, IEEE Trans Vehic. Technol. 59(2010) 2806-2814.

[Liaw *et al*., 2003] B.Y. Liaw, E.P Roth, R.G. Jungst, G. Nagasubrmanian, H.L. Case, D.H. Doughty, J. Power Sources, 119 (2003) 874-886.

[Lide *et al*., 1994] D.R. Lide, et al. Handbook of Organic Solvents, CRC Press, Boca Raton, FL, 1994.

[Lin *et al*., 2013] X. Lin, H.E. Perez, J.B. Siegel, A.G. Stefanopoulou, Y. Li, R.D. Anderson, Y. Ding, M.P. Castanier, IEEE Trans. Control Syst. Technol. 21 (2013) 1745-1755.

[Linden *et al*., 2002] D. Linden, T.B. Reddy, 'Handbook of Batteries,' 3rd Ed., McGraw-Hill, New York, 2002.

[Lisbona *et al*., 2011] D. Lisbona, T. Snee, Process Safety & Env. Protection, 89 (2011) 434-442.

[Lundquist, 2012] Lundquist, Edward H. "DDG 1000's Integrated Power System Software, Hardware Come Together in Successful Test." *Defense Media Network*. Army Material Command, 20 Apr. 2012. Web.

[Maleki *et al*., 1999] H. Maleki, S.A. Hallaj, J.R. Selman, R.B. Dinwiddie, H. Wang, J. Electrochem. Soc. 146 (1999) 947-954.

[Marsh *et al*., 2001] R. Marsh, S. Vukson, S. Surampudi, B.V. Ratnakumar, M.C. Smart, M. Manzo, P.J. Dalton, J. Power Sources 97(2001) 25-27.

[Mayyas *et al*., 2011] A. Mayyas, M. Omar, P. Pisu, A. Alahmer, C. Montes, Int. J. Energy Res. 37 (2011) 331-346.

[Murashko *et al*., 2014] K.A. Murashko, A.V. Mityakov, J. Pyrhönen, V.Y. Mityakov, S.S. Sapozhnikov, J. Power Sources 271(2014) 48-54.

[Ogumi *et al*., 2004] Z. Ogumi, T. Abe, T. Fukutsuka, S. Yamate, Y. Iriyama, J. Power Source 127 (2004) 72–75.

[Pals *et al*., 1995] C. Pals, J. Newman, J. Electrochem. Soc. 142 (1995) 3274-3281.

[Pesaran *et al.*, 2001] A.A. Pesaran, M. Keyser, Thermal characteristics of selected EV and HEV batteries, In: Proc. Annual Battery Conf.: Advances & Applications, Long Beach, CA, USA, 2001.

[Pesaran, 2002] A.A. Pesaran, J. Power Sources 110 (2002) 377-382.

[Rao *et al.*, 2011] Z. Rao. S. Wang, Renewable and Sustainable Energy Reviews 15 (2011) 4554– 4571.

[Schweiger *et al.*, 2010] Schweiger, Hans-Georg, O. Obeidi, O. Komesker, A. Raschke, M. Schiemann, C. Zehner, M. Gehnen, M. Keller, P. Birke, Sensors 10.6 (2010) 5604-625.

[Scrosati *et al.*, 2010] B. Scrosati, J. Garche, J. Power Sources 9(2010) 2419-2430.

[Shah *et al.*, 2014] K. Shah, S.J. Drake, D.A. Wetz, J.K. Ostanek, S.P. Miller, J.M. Heinzel, A. Jain, J. Power Sources 258 (2014) 374-381.

[Shah2 *et al*,.2014] .K. Shah, S.J. Drake, D.A. Wetz, J.K. Ostanek, S.P. Miller, J.M. Heinzel, A. Jain, J. Power Sources 271 (2014) 262-268.

[Smith *et al.*, 2010] K. Smith, G-H. Kim, E. Darcy, A. Pesaran, Int. J. Energy Res., 34 (2010) 204-215.

[Spotnitz *et al.*, 2003] R. Spotnitz, J. Franklin, J. Power Sources 113(2003) 81.

[Srinivasan *et al.*, 2003] V. Srinivasan, C.Y. Wang, J. Electrochem. Soc. 150 (2003) A98-A106.

[Srinivasan *et al.*, 2011] R. Srinivasan, B. Carkhuff, M. Butler, A. Baisden, O. Uy, 'An external sensor for instantaneous measurement of the internal temperature in Lithium-ion rechargeable cells,' In: 'Energy Harvesting and Storage: Materials, Devices, and Applications,', N. Dhar, P. Wijewarnasuriya, A. Dutta (Eds.), SPIE, 2011.

[Taheri *et al.*, 2012] P. Taheri, M. Bahrami, SAE Int. J. Passenger Cars 5 (2012) 164−176.

[Taheri *et al.*, 2013] P. Taheri, M. Yazdanpour, M. Bahrami, J. Power Sources 243 (2013) 280-289.

[Thomas *et al.*, 2003] K. Thomas, J. Newman, J. Power Sources 119(2003) 844-849.

[Thongam *et al.*, 2013] J. Thongam, et al. "All-electric ships—A review of the present state of the art," *Ecological Vehicles and Renewable Energies (EVER), 2013 8th International Conference and Exhibition on*, vol., no., pp.1,8, 27-30 March 2013

[Touloukian *et al.*, 1970] Y.S. Touloukian, et al. Thermophysical properties of matter, 1st Ed., IFI/Plenum, 1970.

[Vaidyanathan *et al*., 2001] H. Vaidyanathan, W. Kelly, G. Rao, J. Power Sources 93(2001) 112.

[Wang *et al*., 2012] Q. Wang, P. Ping, X. Zhao, G. Chu, J. Sun, C. Chen, J. Power Sources 208(2012) 210–224.

[Winter *et al*., 2004] Winter, Martin, and Ralph J. Brodd. *Chemical Reviews* 104 (2004) 4245-270.

[Yi *et al*., 2012] Y. Yi, Y. Shi, N. Cai, J. Lee, X. He, J. Power Sources 199(2012) 227-238.

[Zhang *et al*., 2008] X.C. Zhang, A.M. Sastry, W. Shyy, J. Electrochemical Soc. 155 (2008) A542-A552.

[Zhang *et al*., 2014] J. Zhang, B. Wu, Z. Li, J. Huang, J. Power Sources 259 (2014) 106-116.

Biographical Information

Stephen James Drake was born in Hutchinson, Kansas in November 1981. After graduating high school he moved to Fort Worth, Texas to attend college at Texas Christian University. During his time at TCU he studied abroad in Eastern Europe, was a member of the Kappa Sigma fraternity, and worked part time as an engineering intern at a screw conveyor manufacturing company. In 2005 he graduated with a Bachelor of Science in Mechanical Engineering along with two minors in mathematics and business.

In August 2005, he enrolled as a graduate student at Texas A&M University in College Station, Texas. He obtained his Masters of Science in Mechanical Engineering in May of 2008, focusing in the field of aerosol mechanics and flame synthesis.

Following graduation he moved to Winston Salem, North Carolina to work for General Dynamics Advanced Information Systems. Working as a Principal Systems Engineering helped plan and coordinate missions for electronic warfare systems that persistently monitored the water column, sea floor, and deep-ocean networks. This experience allowed him to travel worldwide for both on and offshore installations.

Returning to Texas in 2011, he enrolled at the University of Texas at Arlington. He was advised by Dr. Ankur Jain and focused on modeling and experimental research involved in cylindrical lithium-ion cells.